ABSTRACT

Title of Document:	STUDYING LIQUID DYNAMICS WITH OPTICAL KERR EFFECT SPECTROSCOPY
	Xiaoxiao He, Doctoral of Philosophy, 2015
Directed By:	Professor, John T. Fourkas, Department of Chemistry and Biochemistry

Time-resolved optical Kerr effect (OKE) spectroscopy is an established technique for studying the orientational dynamics of liquids. The reduced spectral density (RSD) obtained from transforming the OKE spectrum into the frequency domain has shown its utility in probing the intermolecular dynamics of liquids.

The intermolecular dynamics of benzene and its isotopologues have been investigated using OKE spectroscopy. The observed linear dependence of the collective orientational correlation time on the square root of the moment of inertia leads to the conclusion that there is strong translation-rotation coupling in benzene liquid. By analyzing of the RSDs of benzene and its isotopologues, it is evident that the librational scattering dominates the high-frequency region and plays a major role throughout the RSD.

The dynamics of confined liquids have also been studied using OKE spectroscopy. A blue shift of the high-frequency portion of the RSD of confined benzene has been observed. This blue shift is similar to the shift in the RSD of bulk benzene as the

temperature is decreased. It is believed that this shift in the high-frequency portion of the RSD reflects the densification of the liquid in confinement. This phenomenon has also been observed in confined pyridine and acetonitrile liquids.

OKE spectroscopy has also been employed in studies of the dynamics of nano-confined propionitrile and trimethyl acetonitrile. The results of these studies indicate that propionitrile can form a lipid-bilayer-like structure at the confining surfaces, with the alkyl tails of the sublayers being entangled. However, due to the steric effects imposed by the *tert*-butyl group in trimethyl acetonitrile, bilayers are not formed at the confining surfaces for this liquid.

Keywords: OKE spectroscopy, liquid dynamics, nanoconfined liquid, benzene, librational scattering, reduced spectral density, interaction-induced scattering

STUDYING LIQUID DYNAMICS WITH OPTICAL KERR EFFECT SPECTROSCOPY

By

Xiaoxiao He

Dissertation submitted to the Faculty of the Graduate School of the
University of Maryland, College Park, in partial fulfillment
of the requirements for the degree of
Doctor of Philosophy
2015

Advisory Committee:
Professor John T. Fourkas, Chair
Professor Mikhai Anisimov, Dean's Representative
Professor Millard Alexander
Professor Amy Mullin
Professor John Weeks

Acknowledgements

I would like to express the deepest appreciation to my advisor, Professor John T. Fourkas, who gave me the opportunity to work in the Fourkas group and work on this challenging and exciting project. He is a patient and inspiring advisor, especially when I was struggling with the laser at the beginning of my Ph.D. studies. He never blamed me for breaking optics or messing up the alignment. On the contrary, he encouraged me to start an independent way of thinking and find solutions using scientific reasoning. He is also a real genius who has millions of great ideas. Without his guidance and persistent help this dissertation would not have possible.

I would like to thank Professor Mikhail Anisimov for agreeing to serve as the Dean's Representative on my dissertation committee and spend his valuable time in reviewing my thesis. I owe my thanks to Professor John Weeks for being my committee member of my proposal defense and dissertation defense. I also want to express my gratitude to Professor Millard Alexander for teaching me how to use MATLAB, which was of great help in my research. Special thanks goes to Professor Amy Mullin, for her kind assistance throughout my PhD studies, especially for letting me sit in on her lab-VIEW class.

My thanks are also sent to all my graduate friends, especially the Fourkas group members: Dr. Qin Zhong taught me hand by hand how to conduct the optical Kerr effect spectroscopy experiment. He provided me with numerous suggestions and discussions which help me a lot both in research and in life. Dr. Feng Ding coached me how to use vibrational sum frequency generation spectrometer. She helped me enrich

my knowledge and experience in spectroscopy field. Dr. Chris Rivera is a real pro in optics. He had answers to all my questions regarding optics and taught me how to survive as a Ph.D. student. I would also like to thank John Bender. The discussions between us were definitely a most valuable experience for me. The simulations he finished strongly support my experimental results and made our project advance faster. I would also to express my gratitude to Katherine Manfred who was an excellent colleague to work with; Dr. Linjie Li and Dr. George Kumi for their help and support in my Ph.D. studies; Amanda Jane Souna and Shirl Phelps for offering me a great help in my scientific writing. I am obliged to all the other present and past Fourkas group members who supported me during the past 5 years.

I wish to express my deepest love and gratitude to my beloved families for their encouragement and endless love. Last but not the least, I owe sincere and earnest thankfulness to my husband for his support and understanding.

Table of Contents

Acknowledgements ii
Table of Contents iv
List of Tables v
List of Figures vii
Chapter 1 : Introduction 1
1.1 Introduction 1
1.2 Theory of OKE Spectroscopy 4
1.3 The Dynamics of Nanoconfined Liquids 12
1.4 Outline of Thesis 18
Chapter 2 : Experimental Procedures 20
2.1 Introduction 20
2.2 OHD-OKE spectroscopy experimental setup 20
2.3 The sol-gel process and sample preparation 24
2.3.1 Synthesis of the sol-gel glass 28
2.3.2 Characterization and modification of sol-gel glasses 30
2.3.3 Preparation of samples of confined liquids 31
2.4 Data acquisition and analysis 32
Chapter 3 : Assessing the Role of Moment of Inertia in Optical Kerr Effect Spectroscopy 35
3.1 Introduction 35
3.2 Experiments 38
3.3 Results and Discussion 39
3.4 Conclusion 62
Chapter 4 : Density Effects on the Dynamics of Liquids in Nanoconfinement 63
4.1 Introduction 63
4.2 Experiments 65
4.3 Results and Discussion 66
4.3.1 Benzene 66
4.3.2 Pyridine 80
4.3.3 Acetonitrile 91
4.4 Conclusions 100
Chapter 5 : The Structure and Dynamics of Liquid Alkyl Cyanides at Interfaces 103
5.1 Introduction 103
5.2 Experiments 105
5.3 Results and Discussion 106
5.3.1 Propionitrile 106
5.3.2 Trimethyl acetonitrile (TMACN) 113
5.4 Conclusions 117
Chapter 6 : Conclusions and Future Prospects 118
6.1 Conclusions 118
6.2 Future Prospects 120
Bibliography 121

List of Tables

Table 3.1 Molecular properties and fitting parameters for the integrated OKE signal of benzene and its isotopologues..... 41

Table 3.2 Parameters from fits of RSDs of benzene and its isotopologues to a sum of a BL function and an AG function 55

Table 4.1 Decay times (τ_1 and τ_2) and amplitudes (A_1 and A_2) from biexponential fits of the collective orientational correlation function for nanoconfined benzene. 67

Table 4.2 Parameters from fits of RSDs of benzene in unmodified pores to a sum of a BL function and an AG function 75

Table 4.3 Parameters from fits of RSDs of benzene in modified pores to a sum of a BL function and an AG function 76

Table 4.4 Parameters from fits of RSDs of bulk benzene to a sum of a BL function and an AG function..... 78

Table 4.5 Decay times (τ) and amplitudes (A) from biexponential fits of the collective orientational correlation functions for confined pyridine. 82

Table 4.6 Parameters from fits of RSDs of bulk pyridine to a sum of a BL function and an AG function..... 89

Table 4.7 Parameters from fits of RSDs of pyridine in unmodified pores to a sum of a BL function and an AG function 90

Table 4.8 Decay times (τ) and amplitudes (A) from triexponential fits of the collective orientational correlation functions of confined acetonitrile..... 92

Table 4.9 Parameters from fits of RSDs of acetonitrile in unmodified pores to a sum of a BL function and an AG function..... 98

Table 4.10 Parameters from fits of RSDs of bulk acetonitrile to a sum of a BL function and an AG function..... 99

Table 5.1 Parameters from fits of integrated propionitrile OKE data. 110

Table 5.2 Parameters from fits of integrated TMACN OKE data. 115

List of Figures

Figure 1.1 Schematic depiction of the microscopic mechanism of OKE spectroscopy. 3

Figure 1.2 A simplified schematic experimental setup for OKE spectroscopy. 6

Figure 1.3 A time-domain OKE decay for mesitylene at 295 K. 9

Figure 1.4 The reduced spectral density of acetonitrile liquid at 295 K. 12

Figure 2.1 A schematic diagram of the experimental setup for OHD-OKE spectroscopy. 21

Figure 2.2 The time sequence of the four steps involved in the sol-gel synthesis..... 25

Figure 2.3 Sol-gel monoliths as they appear half way through the firing (left) and after the firing (right). 30

Figure 3.1 Natural logarithm of the OKE decays for benzene and its isotopologues. 40

Figure 3.2 Collective orientational correlation times (τ_0) as a function of molecular weight..... 41

Figure 3.3 Collective orientational correlation times (τ_0) as a function of the square root of the tumbling moment of inertia..... 44

Figure 3.4 Normalized (a) RSDs and (b) RSDs with frequencies scaled for maximum overlap for benzene and its isotopologues..... 46

Figure 3.5 Normalized RSDs with frequencies scaled by (a) the inverse square root of the moment of inertia relative to that of benzene and (b) the inverse square root of molecular weight relative to that of benzene for benzene and its isotopologues 47

Figure 3.6 Frequency scaling factors based on moment of inertia (circles) and molecular weight (triangles) as a function of experimental scaling factors. 48

Figure 3.7 Representative fit to the RSD of benzene with the sum of a BL function and an AG function. 55

Figure 3.8 First moments of AG fits to the isotopologue RSDs as a function of the inverse square root of the moment of inertia. 56

Figure 3.9 First moments of BL fits to the isotopologue RSDs as a function of the inverse square root of the moment of inertia. 58

Figure 3.10 First moments of AG fits to the isotopologue RSDs as a function of the inverse square root of the molecular weight. 58

Figure 4.1 Logarithmic plots of the collective orientational correlation function of confined benzene at room temperature. 67

Figure 4.2 Height-normalized RSDs for bulk benzene and benzene in nanopores 69

Figure 4.3 (a) Height-normalized RSDs for benzene at temperatures ranging from 269 K to 295 K in 1 K increments. (b) $\bar{\nu}_{HH}$ for the falling edge of the RSDs of bulk benzene liquid plotted as a function of the temperature. 71

Figure 4.4 The best matches between RSDs of bulk benzene (red, dashed) and confined benzene (black, line). 72

Figure 4.5 Height-normalized RSDs for benzene confined in surface-modified sol-gel glasses. 74

Figure 4.6 Representative fit to the RSD of confined benzene (in pores of 6.6 nm diameter) with the sum of a BL function and an AG function. 75

Figure 4.7 First moments of the AG portion of fits to RSDs of the bulk benzene are plotted as a function of the temperature. 79

Figure 4.8 First moments of the AG portion of fits to RSDs of benzene confined in unmodified pores (solid symbols) and modified pore (open symbols) are plotted as a function of the pore curvature. 79

Figure 4.9 First moments of the BL portion in the RSDs of confined benzene in unmodified pores (solid symbols) and modified pores (open symbols) are plotted as a function of the pore curvature. 80

Figure 4.10 First moments of the BL portion of fits to RSDs of the bulk benzene are plotted as a function of the temperature. 80

Figure 4.11 Logarithmic plots of the collective orientational correlation functions for nanoconfined pyridine. 82

Figure 4.12 Height-normalized RSDs for the bulk pyridine and pyridine confined in sol-gel glasses of pore diameters at 7.3, 5.9, and 2.4 nm. 84

Figure 4.13 (a) Height-normalized RSDs for pyridine at temperatures ranging from 263 K to 290 K. The data have been offset for clarity. (b) $\bar{\nu}_{HH}$ for the falling edge of RSDs is plotted as a function of temperature of bulk pyridine. 86

Figure 4.14 Comparisons of the best match between RSDs of bulk pyridine (red) and confined pyridine (black). 87

Figure 4.15 First moments of the AG portion of fits to RSDs of the bulk pyridine plotted as a function of the temperature. 90

Figure 4.16 First moments of the AG portion of fits to RSDs of pyridine confined in unmodified pores plotted as a function of the pore curvature. 91

Figure 4.17 Logarithmic plots of the collective orientational correlation functions of acetonitrile in sol-gel glasses at room temperature. 93

Figure 4.18 Height-normalized RSDs for bulk acetonitrile and acetonitrile confined in sol-gel glasses 95

Figure 4.19 (a) Height-normalized RSDs for acetonitrile at temperatures ranging from 225 to 295 K. (b) $\bar{\nu}_{HH}$ is plotted as a function of temperature for bulk acetonitrile liquid. 97

Figure 4.20 Comparison of the best matches between RSDs of bulk acetonitrile (red, dashed) and confined acetonitrile (black, solid). 98

Figure 4.21 First moments of the AG portion of fits to RSDs of bulk acetonitrile plotted as a function of the pore curvature..... 99

Figure 4.22 First moments of the AG portion of fits to RSDs of acetonitrile confined in unmodified pores are plotted as a function of the pore curvature. 100

Figure 4.23 Plots of fractional shift ($\bar{\nu}_{HH}/\bar{\nu}_{HH,bulk}$) on the falling edge of RSDs as a function of pore curvature of the confinement for benzene (triangle) and pyridine (diamond).. 102

Figure 5.1 Illustration of the beam polarizations in VSFG spectroscopy..... 107

Figure 5.2 VSFG data for propionitrile at the silica/liquid interface under *SSP* (black), *PPP* (red) and *SPS* (green) polarization conditions.. 108

Figure 5.3 Collective orientational correlation functions for liquid propionitrile in the bulk and confined in silica sol-gel glasses with different pore diameters. 109

Figure 5.4 Estimated thickness of the surface layer of propionitrile molecules with inhibited orientational dynamics as a function of pore diameter.. 111

Figure 5.5 VSFG spectra (solid lines) for TMACN at the silica/liquid interface..... 113

Figure 5.6 Collective orientational correlation functions for TMACN in the bulk and in silica pores of different diameters..... 114
Figure 5.7 Estimated thickness of the surface layer of TMACN with inhibited dynamics as a function of pore diameter..... 115

Chapter 1: Introduction

1.1 Introduction

Liquid dynamics have a pronounced effect on many chemical processes. To develop further insights into these phenomena, it is necessary to attain a deep understanding of the liquid dynamics, especially at the microscopic level. However, liquid dynamics is a challenging area of research. Liquids are disordered and dense, which means that many models that successfully describe the gas phase and solid phase cannot be applied to liquids.[1] Meanwhile, the structure of liquids can evolve on a broad range of time and distance scales, which further complicates their study.

A tremendous amount of effort has been put into the investigation of liquid dynamics in recent years. Progress made in theoretical, experimental and computational methods has brought new perspectives into this field. Experimentally, neutron scattering,[2] low-frequency Raman spectroscopy,[3] and far-infrared spectroscopy[4] have all proven to be powerful tools for exploring liquid dynamics on a microscopic scale. The development of pulsed laser technology has allowed time-domain techniques, such as optical Kerr effect (OKE) spectroscopy,[3,5–8] to be used in lieu of frequency-domain techniques. The ease of implementation of OKE spectroscopy,[9] its high signal-to-noise ratio, and its ability to provide time-resolved signals make OKE spectroscopy a powerful technique for studies on a wide range of problems in liquid dynamics.

In OKE spectroscopy, a linearly polarized optical pump pulse is focused into an isotropic sample, creating a transient birefringence. A second, linearly-polarized probe pulse, with a polarization that is different from that of the pump pulse, overlaps spatially with the pump pulse in the sample but arrives at a variable delay time. A polarizer that is crossed with the polarization of the probe pulse is placed after the sample. The transient birefringence of the sample can make the polarization of the probe pulse elliptical, as shown in Figure 1.1. Therefore, a fraction of the probe pulse can pass through the polarizer and be detected as the OKE signal. The time-domain OKE decay is measured by recording the OKE signal as a function of the delay time.

By Fourier-transforming the time-domain OKE decay, OKE signals can be converted into Bose-Einstein-corrected,[10] low-frequency Raman spectra. It is a common practice to subtract the contribution of collective orientation diffusion from the OKE signal. The remaining OKE signal can be transformed into the frequency domain, yielding the "reduced spectral density" (RSD). The RSD facilitates studies on the intermolecular vibrational dynamics of liquids.[11] The portion of the RSD in the frequency range from 0 to 300 cm^{-1} is particularly useful in studies of intermolecular vibrational dynamics.

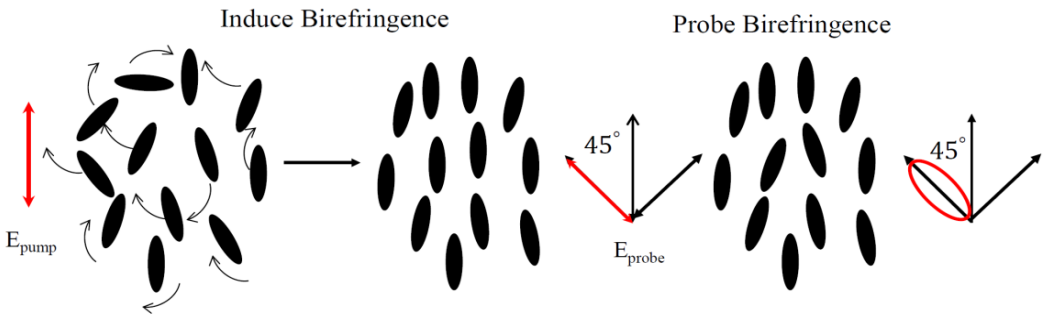

Figure 1.1 Schematic depiction of the microscopic mechanism of OKE spectroscopy. Before the pump pulse arrives, molecules are randomly oriented in the liquid. The pump electric field induces a small net alignment, making the sample birefringent. The birefingence induces ellipticity in the probe pulse polarization, and the depolarization is detected through a crossed polarizer. The signal decays as orientations randomize. Reproduced from reference 11.

Although the RSD carries information regarding intermolecular vibrational dynamics, determining its microscopic origin is made difficult by the fact that the RSD is generally broad and lacks distinct features.[12] Attempts have been made both theoretically and experimentally to understand the lineshape of the RSD. For instance, it is common to employ empirical functions to fit the RSD to unravel its molecular origins. For example, the RSD can be fit to a sum of a Bucaro–Litovitz function[13] and an antisymmetrized Gaussian function.[14] Alternatively, RSDs for liquids that are composed of molecules of different shapes, electrostatic properties, and moments of inertia can be compared to achieve a better understanding of the factors that affect the form of the RSD.

The application of OKE spectroscopy is not restricted to simple liquids. With the evolution of ultrafast lasers, the use of OKE spectroscopy has been extended to complex liquid systems, such as liquid crystals,[15,16] ionic liquids,[17,18] and confined liquids.[19–21] Among these systems, considerable effort has been put into studies on confined liquids, due to their broad appearance throughout nature.[22–26]

When a liquid is confined in a nanoscale space, substantial changes can occur in its dynamics and structure.[27,28] For example, the interaction between molecules and confining surfaces can hinder molecular translational motions, leading to a change of the glass-transition temperature for confined liquids when compared to their bulk counterparts.[29]

Many factors can influence the dynamics of a confined liquid, such as molecular shape,[30] molecular electrostatic properties,[30] and the interaction between liquid molecules and confining surfaces.[21] The interplay among these factors determines how much the dynamics of a confined liquid deviates from these of the corresponding bulk liquid. Therefore, by studying how these factors influence the OKE spectrum, it is possible to gain insight into the structure and dynamics of confined liquids on microscopic level. Results obtained from such studies have the potential to be used in many technical fields, such as in designing more efficient lubricants or enhancing the rate of oil recovery.

1.2 Theory of OKE Spectroscopy

When an intense, linearly polarized pump pulse propagates through an isotropic liquid, the electric field of the pump pulse induces dipoles in the liquid mol-

ecules. Driven by the impulsive torque created by the interaction between the electric field and the light-induced dipoles of the liquid molecules, the axes of maximum polarizability of these molecules tilt toward the plane of polarization of the light. The net orientation of molecules leads to a difference in refractive index of the liquid in directions parallel and perpendicular to the polarization of the pump pulse. In other words, the liquid becomes birefringent. This process of inducing a transient birefringence with a pump pulse is called the optical Kerr effect. Mayer and Gires[31] demonstrated for the first time that intense, nanosecond, optical pulses from a Q-switched ruby laser could be used to produce an electric field that is strong enough to generate birefringence within isotropic liquids. This observation marked the birth of OKE spectroscopy. Inspired by this innovation, Duguay and Hansen[5] used OKE spectroscopy to study the short-time orientational dynamics of simple molecules such as CS_2 and nitrobenzene. With powerful picosecond laser pulses, the ultra-short, non-instantaneous relaxation of liquid molecules was observed with OKE spectroscopy. It was also demonstrated for the first time that induced dipoles, rather than permanent dipoles, dominate the OKE signal.[5]

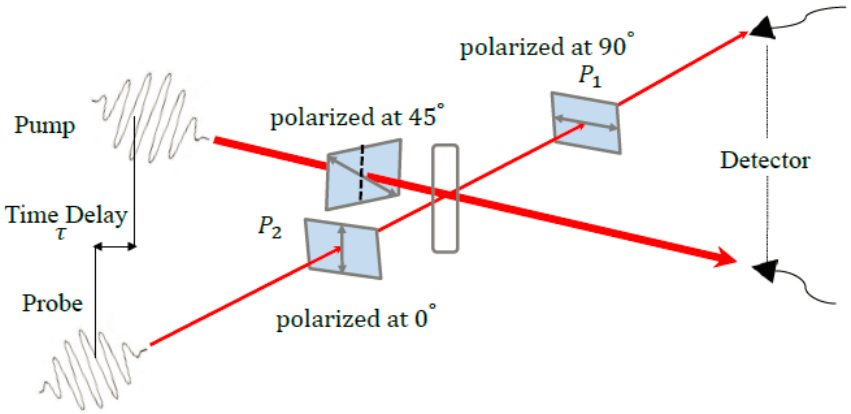

Figure 1.2 A simplified schematic experimental setup for OKE spectroscopy. The pump pulse (polarized at 45°) induces birefringence within the sample. The probe pulse comes at a variable delay time. The polarization of the probe is detected by the transmission through a polarizer pair (P_1, P_2). If there is no birefringence, the probe pulse cannot pass through the polarizer P_1.[5]

In OKE spectroscopy, a laser-induced anisotropy is created by a pump pulse and detected by a weak, polarized probe pulse that arrives at a variable delay time. By changing the delay time between the pump and probe pulses, the signal can be recorded as a function of delay time. The Kerr response as a function of delay time t is given by:

$$E_s(t) = E_S e^{-i\omega t}, \qquad \text{(Eq. 1.1)}$$

where ω is the carrier frequency of laser, and E_S is the electric field amplitude of the Kerr response. The detected signal is related quadratically to E_S:

$$I_s \propto |E_s(t)|^2. \qquad \text{(Eq. 1.2)}$$

I_s is usually referred to as the homodyne OKE signal. The analysis of the homodyne signal is complicated by the quadratic relationship between I_s and E_S.

To avoid the intricacy involved in data analysis, an optical-heterodyne detection (OHD) method[32] is often used in OKE spectroscopy. The essence of the OHD method is introducing a local oscillator to mix with the Kerr response. To introduce this local oscillator, a quarter-wave plate, with its "fast" axis parallel to the polarization of the probe, is placed before the sample and between P_1 and P_2. By rotating P_1 by an angle of $\theta \leq 1°$ away from the maximum extinction position (the position where the polarization of probe is orthogonal to the polarization of the pump), a local oscillator is created with electric field of:

$$E_{LO} = E_{probe} e^{-i\omega t} e^{i\pi/2}, \qquad \text{(Eq. 1.3)}$$

where E_{probe} is the electric field amplitude of the probe pulse. The local oscillator is in phase with the signal. Thus, the detected signal in the OHD method is:

$$\begin{aligned} I \ &\propto |E_s + E_{LO}|^2 = \left|E_s e^{-i\omega t} + E_{probe} e^{-i\omega t} e^{i\pi/2}\right|^2 \\ &= I_s + I_{LO} + 2E_s E_{probe}. \end{aligned} \qquad \text{(Eq. 1.4)}$$

Of the three components of the detected signal in (Eq. 1.4), the weakest and the strongest components are the local oscillator intensity (I_{LO}) and the homodyne signal (I_s), respectively. If we could get rid of these two terms, the rest of the signal intensity would scale linearly with the imaginary portion of the Kerr response. Suppression of I_s and I_{LO} can be achieved by collecting spectra with P_1 set at angles of $\pm\theta$. When the OKE signal is collected at the positive angle, it can be described by (Eq. 1.4). When the OKE signal is collected at the negative angle, the cross-term has the opposite sign:

$$I' \propto I_S + I_{LO} - 2E_S E_{probe}. \qquad \text{(Eq. 1.5)}$$

By subtracting (Eq. 1.5) from (Eq. 1.4), the homodyne signal and the intensity of the local oscillator can be rigorously eliminated.

The implementation of the OHD-OKE scheme can significantly enhance the signal-to-noise ratio, allowing us to observe several features[6] in the OKE spectrum, as shown in Figure 1.3. In this figure, the first feature is the spike that appears near time zero, which is the instantaneous electronic response originating from the molecular hyperpolarizability. This electronic response is denoted as $\sigma^{(3)}(t)$, and is approximated by a delta function centered at time zero:

$$\sigma^{(3)}(t) = b\delta^{(3)}(t). \qquad \text{(Eq. 1.6)}$$

The second feature is a strong oscillation arising after time zero and damping away at longer times. It has been shown that this feature arises from Raman-active, intramolecular vibrational motions whose frequencies lie within the bandwidth of the laser pulse.[33] A sub-picosecond, non-exponential decay is buried under this oscillatory feature and is ascribed to the intermolecular vibrational response.[33]

There is a lengthy and nearly single-exponential decay that dominates the spectrum after a few picoseconds. This decay arises from the molecular orientational diffusion and is proportional to the time derivative of the collective orientational correlation function $C_{coll}(t)$. $C_{coll}(t)$ can usually be described by a single or multi-exponential function.[34] The time constants associated with these exponential decays are called the collective orientational correlation times and can be used to estimate the molecular hydrodynamic volume through the Debye-Stokes-Einstein (DSE) equation:[35]

$$\tau = \frac{V\eta}{k_B T} = \frac{4\pi r^3 \eta}{3k_B T}, \qquad \text{(Eq. 1.7)}$$

where k_B is Boltzmann's constant, η is the shear viscosity, T is the temperature in units of Kelvin, and V and r are the hydrodynamic volume and the hydrodynamic radius required for reorientation, respectively.

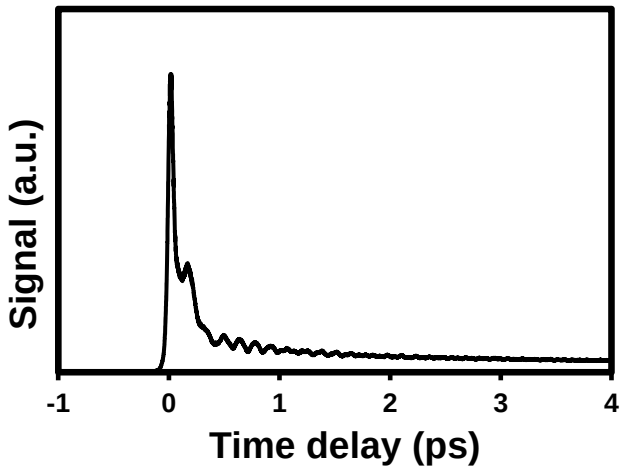

Figure 1.3 A time-domain OKE decay for mesitylene at 295 K. The sharp feature at zero delay time is the electronic response. The oscillations in the decay arise from Raman-active, intramolecular vibrational modes. Coherently excited intermolecular modes are the major contribution to the decay at times up to ~1 ps. At greater delay times, orientational diffusion dominates the OKE decay.

Although the orientational dynamics of liquids have been studied extensively with OKE spectroscopy, using OKE spectroscopy to study the intermolecular vibrational dynamics is still challenging. Because the orientational diffusion portion of the OKE signal often overwhelms all of the other components in the time-domain OKE signal, it is difficult to isolate the intermolecular component from the

others. However, intermolecular motions and orientational diffusion do not necessarily share the same frequencies, so they can be separated in the frequency domain. Considering the fact that OKE spectroscopy is the formal time-domain equivalent of low-frequency Raman scattering (also known as Rayleigh-wing scattering), transforming the spectrum into the frequency domain makes it possible to separate intermolecular dynamics from the diffusive orientational dynamics.

In the interest of converting the OKE spectrum into the frequency-domain, McMorrow and Lotshaw[11] developed the Fourier-transform four-wave mixing (FT4WM) method. A brief description of this technique is presented below.

The transmission of a Kerr cell is given by the convolution of the molecular nonlinear optical response function $R^{(3)}(t)$ with the second-harmonic-generation cross-correlation of the laser pulses—$G^{(2)}(t)$, where t is the delay time between the pump and the probe. The expression for the signal is:

$$S(t) = \int_{-\infty}^{+\infty} G^{(2)}(t - t')R^{(3)}(t)dt' = G^{(2)}(t) \otimes R^{(3)}(t), \quad \text{(Eq. 1.8)}$$

where $\otimes$ is the convolution operator. Based on the Born-Oppenheimer approximation,[36] $R^{(3)}(t)$ can be approximated by the sum of the nuclear response $r^{(3)}(t)$ and the electronic response $\sigma^{(3)}(t)$:

$$R^{(3)}(t) = \sigma^{(3)}(t) + r^{(3)}(t). \quad \text{(Eq. 1.9)}$$

$G^{(2)}(t)$, can be measured experimentally, and is given by:

$$G^{(2)}(t) = \int_{-\infty}^{+\infty} I_{pump}(t - t')I_{probe}(t)dt' = I_{pump} \otimes I_{probe}, \quad \text{(Eq. 1.10)}$$

where I_{pump} and I_{probe} are intensities of the pump beam and the probe beam, respectively.

Conversion into the frequency domain is achieved by taking the Fourier transform of (Eq. 1.10):

$$F[S(t)] = F\left[G^{(2)}(t)\right] \times F\left[R^{(3)}(t)\right]. \qquad \text{(Eq. 1.11)}$$

The Fourier transform of the electronic response is a real constant that can be removed easily, leaving only the nuclear response in the expression.

$$\begin{aligned} \frac{F[S(t)]}{F[G^{(2)}(t)]} &= F\left[r^{(3)}(t)\right] + F\left[\sigma^{(3)}(t)\right] \\ &= F\left[r^{(3)}(t)\right] + b \\ &= D^{(3)}(\Delta\omega), \end{aligned} \qquad \text{(Eq. 1.12)}$$

where $D^{(3)}(\Delta\omega)$ is the frequency-domain representation of the molecular response to the applied optical field. Because the nuclear response $r^{(3)}(t)$ is zero before time zero, it only contributes to $\mathrm{Im}D^{(3)}(\Delta\omega)$, which is commonly referred as the spectral density.

The spectral density contains contributions arising from coherent vibrations and from the diffusive relaxation of the laser-induced orientational anisotropy. Assuming that the nuclear response is the sum of these two, a spectrum that only contains the vibrational response can be obtained by subtracting the diffusive portion from the response function. Based on previous studies of diffusive relaxation, the functional form of orientational diffusion that is subtracted from the spectral density is:

$$\exp\left(\frac{-t}{\tau_{or,coll}}\right)\left(1-\exp\left(\frac{-t}{\tau_{rise}}\right)\right), \qquad \text{(Eq. 1.13)}$$

where $\tau_{or,coll}$ is the time constant for the liquid to relax back to its isotropic state and τ_{rise} is the rise time of the diffusive response, which is typically assumed to be $\cong$ 200 fs. By removing this portion and performing a Fourier transform of the response function, the spectral density is free of the orientational component. The resultant spectrum is called the "reduced spectral density" (RSD). A representative of the RSD is shown in Figure 1.4.

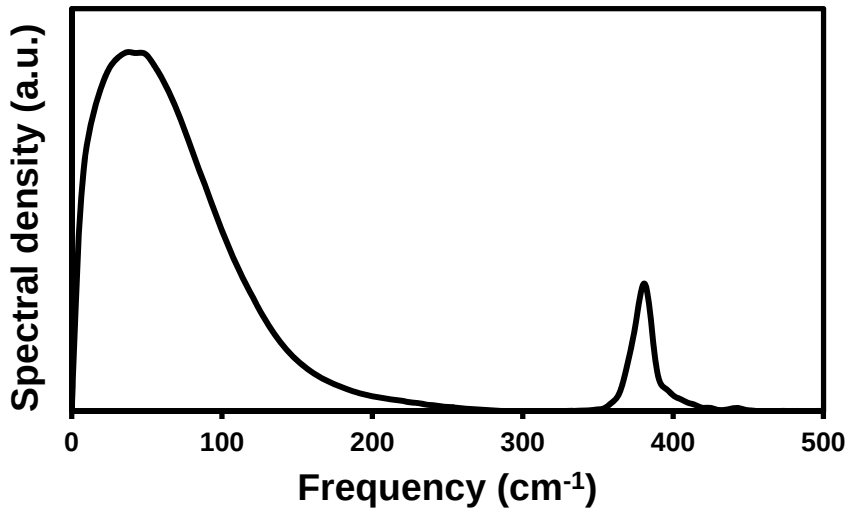

Figure 1.4 The reduced spectral density of acetonitrile liquid at 295 K.

1.3 The Dynamics of Nanoconfined Liquids

Monitoring the dynamics of nanoconfined liquids is challenging. One challenge comes from the selection of the confining material. To ensure that confinement-induced changes in dynamics can be probed, a large fraction of the liquid molecules must be in contact with the confining surfaces. Because the interactions between liquids and confining surfaces are of great relevance in the dynamics of

the confined liquid, using a confining material that can be chemically modified is additionally important.

Silica-based sol-gel glasses are suitable materials for the study of confined liquids.[37,38] Sol-gel glasses have a high surface-to-volume ratio and hence can increase the fraction of interfacial molecules, making the detection of these molecules possible. The high optical quality of sol-gel glasses helps to minimize the background absorption and scattering. The pore diameters of these glasses can be varied from twenty Ångstroms to several hundreds of Ångstroms by changing the synthetic conditions, facilitating the study of pore-size-dependent phenomena in confined liquids. The silanol groups at the pore surfaces can be chemically modified to tune the strength of the interaction between liquid molecules and the confining surfaces.

Inspired by Warnock, Awschalom, and Schafer's[39] OKE study on CS_2 confined in sol-gel glasses, a wide variety of liquids confined in this material have been studied using this technique.[20,21,40–43] Some important conclusions from these studies are highlighted here.

Liquids can be roughly sorted into weakly-wetting and strongly-wetting[40] based on the strength of the interactions between the liquid and the confining surfaces relative to the strength of the intermolecular interactions. Weakly-wetting liquids have modest attractive interactions with pore surfaces. In the bulk phase, simple weakly-wetting liquids have well-characterized, single-exponential diffusive orientational relaxation. When such liquids are confined in sol-gel glasses, their

relaxation dynamics is described by a multi-exponential function. The smallest observed exponential relaxation time is typically close to the diffusive orientational relaxation time in the bulk liquid, and is independent of the pore curvature. This time constant presumably arises from the relaxation of molecules that are far away from the surfaces, and hence are relatively unaffected by a change of the pore curvature. The greater time constants are several times larger than the bulk time constant. These greater times arise from the constrained orientational relaxation of molecules at surfaces. Each exponential component in this multi-exponential function has an amplitude that can be used to determine the relative population of molecules in the pore center or at the surfaces. The time constants can be used to estimate the hydrodynamic volume of molecules through the DSE[35] equation. By comparing the hydrodynamic volume of molecules in the pore center and at the surfaces, we can explore the differences in their molecular relaxations.

Because weakly-wetting liquids have weaker interactions with the confining surfaces, they facilitate studies on the inhibited molecular reorientation of molecules with different molecular shape. For example, for rod-like molecules such as 2-butyne, the smallest orientational relaxation time is independent of the pore curvature. However, for disk-like weakly-wetting molecules such as benzene, the smallest orientational relaxation time has a dependence on the pore curvature. Zhu *et al*.[44] concluded that this difference between 2-butyne and benzene is caused by the fact that benzene adopts a highly ordered structure within the pores of the sol-gel glasses, and hence that the relaxation of benzene located in the pore centers can be affected by the geometric factors through this ordered structure.

Liquids that have substantial interactions with the confining surfaces are classified as strongly-wetting. An example of such a liquid is acetonitrile. Acetonitrile molecules can accept hydrogen bonds from silanol groups at the surfaces of the sol-gel glasses, and so this liquid serves as a prototype for studying the dynamics of strongly-wetting liquids.[45] Tri-exponential orientational relaxation dynamics can be observed for acetonitrile confined in sol-gel glasses, and three orientational relaxation time constants can be obtained. Similar to weakly-wetting liquids, for acetonitrile, the smallest time constants among the three orientational relaxation time constants originates from the orientational relaxation of the molecules in the pore centers. Because acetonitrile molecules can form hydrogen bonds with surface silanol groups, the relaxation of the surface acetonitrile molecules is hindered by the molecular-surface interaction. This population accounts for the largest orientational relaxation time constant, which is an order of magnitude greater than the smallest one. The intermediate orientational relaxation time constant arises from molecules "exchanging" between molecules in the pore center and at the confining surfaces. Due to the large dipole moment of acetonitrile molecules, they have some tendency to form antiparallel dipole-pairs in the liquid. A second layer of acetonitrile molecules, with the CN group pointing into the bulk, can fit in the space between the hydrogen-bonded surface acetonitrile molecules and can exchange with molecules far away from the surface. The intermediate orientational relaxation is 3 to 4 times slower than the orientational relaxation of the molecules in the pore centers.

To determine whether hydrogen bonding plays a key role in the inhibited relaxation of the surface molecules, it is necessary to compare the dynamics of acetonitrile confined in hydrophilic pores and hydrophobic pores. It has been observed that when acetonitrile is confined in hydrophobic pores its slowest exponential relaxation disappears entirely, and it behaves like a weakly-wetting liquid. This observation demonstrates that the hydrogen bonds between molecules and the surface silanol groups can give rise to the retardation of surface dynamics.

To study the intermolecular dynamics of the nanoconfined liquids, we need to know the microscopic origin of their RSDs. It has been proposed that the intermolecular motion can contribute to the OKE signal through two mechanisms: librational scattering and interaction-induced (II) scattering.[46] When molecules reorient within the cages made by their nearest neighbor molecules, their dynamics are hindered. These molecules therefore oscillate back and forth. This oscillatory motion is called libration and contributes to the RSD. As in the case of molecules with isotropic polarizability, besides the libration, the interaction between induced dipole moments can also contribute to the OKE signal. Such interaction-induced relaxation can occur through both translational motion and orientational motion. However, using these mechanisms to interpret the RSD is challenging, due to the featureless lineshape of the RSD and the presence of a frequency-dependent cross-term between different contributions.

To understand the RSD lineshape, efforts have been put into fitting of the RSD with phenomenological functions, each of which is assumed to represent a

physically meaningful aspect of the liquid dynamics. In such fits, librational scattering is often described in the form of an antisymmetrized Gaussian[46] (AG) function that dominates at higher frequencies:

$$g_{AG} = A_{AG}\left[\exp\left(-\frac{(\omega-\omega_1)^2}{2\sigma^2}\right) - \exp\left(-\frac{(\omega+\omega_1)^2}{2\sigma^2}\right)\right], \qquad \text{(Eq. 1.14)}$$

where A_{AG} is the relative amplitude, ω_1 is the center frequency, and σ is the bandwidth of the asymmetric Gaussian lineshape. This AG function was proposed to describe the contribution of librations.[14]

The rest of the RSD is often described by a Bucaro-Litovitz[13] (BL) type function:

$$g_{BL} = A_{BL}\omega^{\delta}\exp\left(-\frac{\omega}{\omega_0}\right), \qquad \text{(Eq. 1.15)}$$

where A_{BL} is the relative amplitude and ω_0 is the characteristic frequency. The exponent δ is given by the expression $\delta = 2\frac{m-7}{7}$, where the factor *m* is the exponent of the distance dependence responsible for the polarizability modification due to a collision. Bucaro and Litovitz determined that for atomic fluids a value of $m = 9$ corresponds to a polarizability distortion caused by an electronic cloud overlap.[13] This value increases to $m = 13$ for a structural frame distortion in molecules. The BL function was originally developed to describe depolarized light scattering of atomic fluids in an isolated binary collision model. In this model, all depolarized scattering arises from collision-induced interactions, and hence it is often postulated that the BL component of the fit arises from II scattering in molecular liquids. The usefulness of such fits as mathematical descriptions of the RSD is undeniable, but the physical information imparted by the fits remains controversial.

1.4 Outline of Thesis

This thesis presents studies of the structure and dynamics of simple and confined liquids using both time-domain OKE decays and their corresponding RSDs. It is organized as follows:

Chapter 2: In this chapter, the synthesis, modification and characterization of the sol-gel glass that are used as the nanoscale confinement for liquids are discussed. Then, detailed descriptions of the sample preparation, the experimental setup, and the data collection procedure are provided. The transformation from the OKE spectrum to the RSD is discussed.

Chapter 3: In this chapter, an OKE study of benzene and four of its isotopologues (C_6D_6, $C_6H_3D_3$, $^{13}C_6H_6$, and $^{13}C_6D_6$) is presented. In all cases, the higher-frequency portion of the RSDs can be superimposed through scaling the frequency by the ratio of the moments of inertia of benzene and its isotopologues. The collective orientational correlation times of these liquids can be scaled with the inverse square root of the tumbling moment of inertia of these molecules, indicating that there is a strong translation−rotation coupling in benzene. Empirical fits to the RSDs suggest that librational motions dominate the depolarized scattering over the entire intermolecular spectrum.

Chapter 4: In this chapter, the role that density plays in the dynamics of nanoconfined benzene is studied using the RSD. The densification of nanoconfined benzene can cause a blue shift of the high-frequency (50 to 150 cm^{-1}) edge of its RSD. This conclusion is supported by the observation of a similar blue shift of the high-frequency edge of the RSD as bulk benzene liquid is densified by decreasing the

temperature. To test this idea further, pyridine and acetonitrile are studied using the same experimental method. The blue shift of the high-frequency edge of the RSD can also be observed in these liquids as they are confined in sol-gel glasses, which suggests that the density effect is present regardless of molecular shape and intermolecular structure.

Chapter 5: The dynamics of confined propionitrile and confined trimethyl acetonitrile (TMACN) are compared to those of acetonitrile using OKE spectroscopy. Experimental results demonstrate that the surface propionitrile molecules have a lipid-bilayer structure and are entangled, whereas TMACN molecules can form a surface monolayer due to the tertiary alkyl group. These results can be combined with the results obtained from studies on propionitrile and TMACN using vibrational sum-frequency-generation (VSFG) spectroscopy, giving us a detailed picture of the structure and dynamics of these liquids in confinement.

Chapter 2: Experimental Procedures

2.1 Introduction

OKE spectroscopy is pump-probe technique. In this method, two optical pulses (the pump pulse and the probe pulse) are used to investigate the dynamics of liquids. In Section 2.2, our experimental setup for the OHD-OKE spectroscopy is introduced.

Sol-gel glasses are useful materials with which to study confined liquids. In Section 2.3, the synthesis, the characterization, and the modification of the sol-gel glass are introduced with details, followed by a description of the preparation of the confined liquid samples.

In Section 2.4, our data acquisition and analysis procedures are discussed. Details of the data analysis in a specific experiment may vary, so full descriptions are reserved for later chapters.

2.2 OHD-OKE spectroscopy experimental setup

A schematic diagram of experimental setup of the OHD-OKE spectroscopy is shown in Figure 2.1. In this setup, a Ti:Sapphire laser is pumped by a 4.5-W green laser to produce a train of mode-locked pulses centered at 800 nm with a repetition rate of 76 MHz. The average output power of the Ti:Sapphire laser is ~350 mW.

To compensate for group velocity dispersion (GVD), the laser output is reflected multiple times from a pair of negatively-chirped mirrors and then passes

through a compressor with two LaFN28 prisms. A pinhole and a pair of lenses are used for spatial filtering of the beam. After being spatially filtered, the beam has a round mode and a clear edge. A beam splitter is then used to split the beam into the pump beam (95%) and the probe beam (5%). Then, the pump beam and the probe beam pass through optics that are as similar as possible to ensure that the pulse widths are identical when they arrive at the sample. The pump beam and the probe beam are modulated at 7:5 frequency ratio by passing through the outer slots and the inner slots of a chopper wheel, respectively.

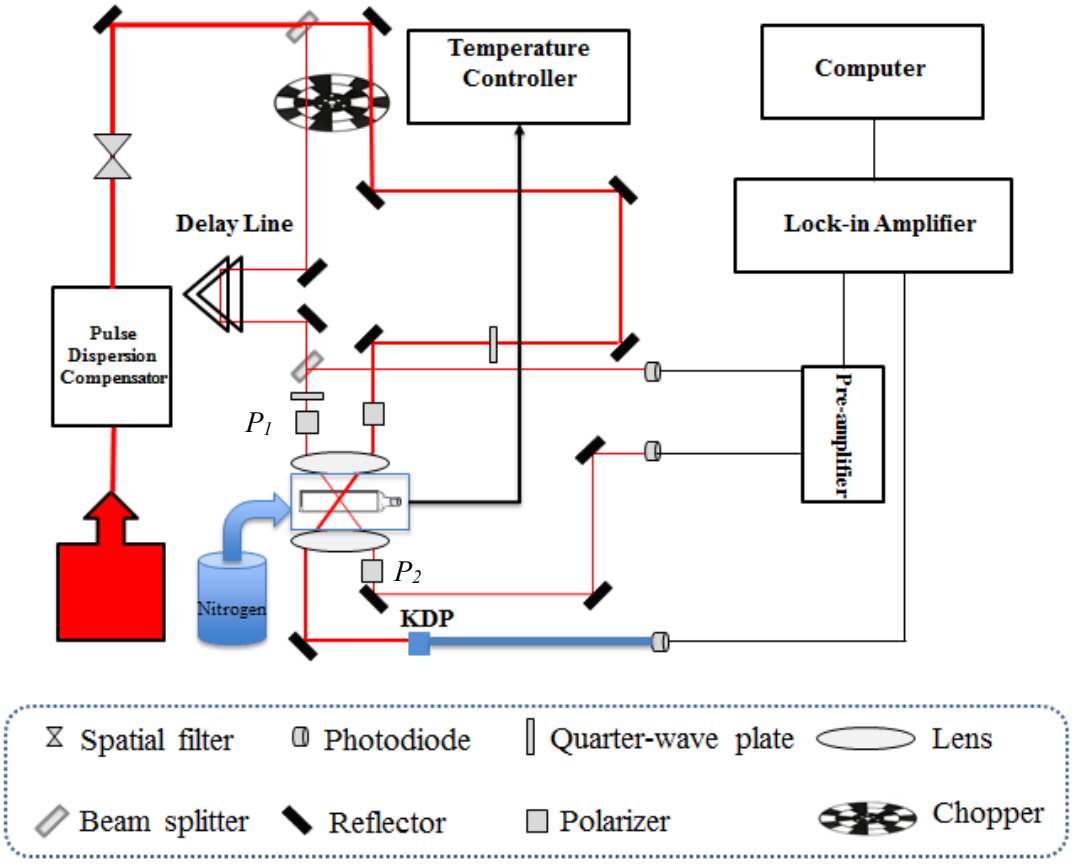

Figure 2.1 A schematic diagram of the experimental setup for OHD-OKE spectroscopy.

The probe beam is then reflected by a retroreflector that is mounted on a computer-controlled delay line (Newport MTL250CC with Newport controller MM1000DC). The resolution of the delay line is 0.667 fs/step. A small amount of the probe beam is picked off by a beam splitter and is directed into a photodiode. This small portion of the probe beam is used as the reference signal for the pre-amplifier. The rest of the probe beam passes first through a calcite Glan-Taylor polarizer (P_1) that is mounted on a high-resolution rotation stage and then through a quarter-wave plate with its fast axis set to vertical. The polarizer is used to set the polarization of the probe to vertical. To achieve the maximum extinction of the probe beam at the analyzer polarizer (P_2), the pump beam is blocked and the quarter-wave plate is removed from the experimental setup. P_1 is then rotated until the minimum amount of the probe beam passes through. To implement the heterodyne detection method, the quarter-wave plate is replaced in the path of the probe beam and polarizer P_1 is rotated from its maximum extinction position by an angle of $\theta \leq 1^{\circ}$ to introduce a local oscillator. The pump is then unblocked.

The polarization of the pump beam is set to 45° with respect to that of the probe beam using a half–wave plate/polarizer combination. The pump beam and the probe beam are spatially overlapped in the sample using an achromatic lens. After the sample, the probe beam is recollimated by another lens. Then, the probe beam passes through the analyzer polarizer, which is set to horizontal. If the sample makes the probe beam elliptically polarized, the horizontal projection of the probe beam will pass the analyzer polarizer. This transmitted light is the OKE signal. The

OKE signal is collimated by an achromatic doublet, sent into an amplified photodiode, and further amplified by a lock-in amplifier (Stanford Research Model 810 DSP). After the sample, the pump beam is recollimated by a pair of lenses and then passes through a frequency doubling (KDP) crystal. The frequency-doubled beam is then detected by an amplified photodiode and another lock-in amplifier (Stanford Research Model 810 DSP). Because the intensity of this frequency-doubled light and the OHD-OKE signal are both proportional to the square of the laser intensity, any long-term intensity variations in the signal can be accounted for by dividing the OHD-OKE signal by the frequency-doubled signal.

To obtain the RSD, the cross-correlation of the pump beam and the probe beam is required:

$$A(t_d) = \int_{-\infty}^{+\infty} I_{pump}(t) I_{probe}(t - t_d)\, \mathrm{d}t, \qquad \text{(Eq. 2.1)}$$

where the I_{pump} and I_{probe} are the intensities of the pump beam and the probe beam, respectively. The FWHM (Δx) of the cross-correlation function can be used to deduce the pulse duration, t_p:

$$t_p = (k\Delta x \sin\phi)/c, \qquad \text{(Eq. 2.2)}$$

where k is the deconvolution factor, which is $\sqrt{2}$ for Gaussian pulses or 1.54 for sech^2 pulses, ϕ is the half angle between the two incident beams, and c is the speed of light.

Because the durations of laser pulses are much shorter than the response times of most detectors, a simple and cost-effective cross-correlation measurement is achieved by using second-harmonic generation (SHG). In this cross-correlation

technique, the pump pulse and the probe pulse are focused in a nonlinear crystal to produce SHG radiation. Experimentally, we use a KDP crystal to serve this purpose. When the pump pulse and the probe pulse are overlapped well temporally and spatially, bright blue light is generated by the KDP crystal. This blue light then passes through an achromatic doublet and is detected by an amplified photodiode. By changing the delay time between the pump pulse and the probe pulse, the cross-correlation signal can be recorded by the photodiode. This cross-correlation signal is further amplified by a lock-in amplifier.

2.3 The sol-gel process and sample preparation

In studies on confined liquids, the confining material must have a large surface area. Therefore, porous material, such as zeolites,[47] membranes,[48] Vycor® glass,[49] and sol-gel glass[50] are widely used in such studies. Among all these materials, sol-gel glasses have many favorable properties, including low density, low conductivity, relatively large surface area, and high optical transmission. These properties enable the broad application of sol-gel glasses in optical experiments. In particular, the low birefringence of sol-gel glasses can keep the background signal to a minimum, making them ideal confining media for OKE spectroscopy experiments.[51]

The sol-gel process used in making inorganic ceramics and glasses was first employed around 150 years ago.[52,53] Back then, people found that adding an acid to a mixture of tetraethoxysilane (TEOS) and water could turn the solution into a

"glass-like" form. After patiently drying this solution for a long period, a transparent solid was produced. This solid is a sol-gel glass that is built from individual SiO_2 particles. The pores in the sol-gel glass have diameters on the nanometer scale.

There are three approaches used to make sol-gel glasses[50]: (1) gelation of a solution of colloidal powders; (2) hydrolysis and polycondensation of alkoxide or nitrate precursors followed by supercritical drying of gels; (3) hydrolysis and polycondensation of alkoxide or nitrate precursors followed by aging and drying gels under ambient conditions. We use the third method to synthesis sol-gel glasses, because sol-gel glasses made with this method have relatively larger (>400 m^2/g) surface areas, smaller average pore diameters (<10 nm), higher optical transmission, lower coefficients of thermal expansion, and better homogeneity than sol-gel glasses made by the other two methods.

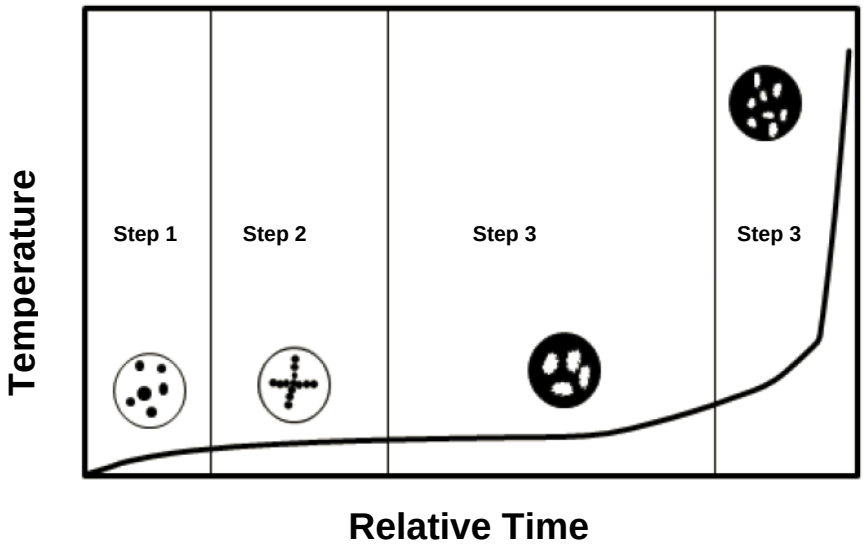

Figure 2.2 The time sequence of the four steps involved in the sol-gel synthesis process. Step 1: hydrolysis and pre-condensation; Step 2: gelation; Step 3: aging and drying; Step 4: firing.

Four steps are involved in synthesis process: hydrolysis and condensation, gelation, aging and drying, and firing. The time sequence of these steps is illustrated in Figure 2.2.

(1) Hydrolysis and condensation

Most sol-gel glasses are formed from alkoxysilanes, such as tetramethoxysilane (TMOS) or tetraethoxysilane (TEOS), because these species can be readily hydrolyzed and can condense under mild conditions. Alkoxysilane molecules are hydrolyzed into hydroxyl derivatives when they are mixed with water. Due to the poor solubility of alkoxysilanes in water, alcohol is needed during the hydrolysis. To speed up the reaction, acid is usually added. When the hydrolysis is proceeding in the mixture, collisions between hydroxyl derivatives or between hydroxyl derivatives and alkoxysilane molecules can lead to condensation into larger particles. Because the rate of the hydrolysis is faster than that of condensation, entangled or randomly branched chains of silicic acid are formed. These chains are the 'sols'. The size of the sols and the strength of the interactions between the sols depend upon the pH and the ratio $R = [H_2O]/[Si(OR)_4]$. Sols can undergo polycondensation reactions, which are catalyzed by base, immediately after their formation.

The whole process described above is called the two-step, acid-base, sol-gel process. Taking the TEOS example, the reactions involved in its hydrolysis and polycondensation process are:

(1) TEOS molecules are hydrolyzed in the presence of acid and form silicic acid ($Si(OH)_4$):

$$Si(OC_2H_5)_4+4H_2O \xrightarrow{H^+} Si(OH)_4+4C_2H_5OH. \qquad \text{(Eq. 2.3)}$$

(2) Silicic acid molecules condense into sols with a base catalyst:

$$Si(OH)_4+(OH)_4Si \xrightarrow{OH^-} (OH)_3Si\text{-}O\text{-}Si(OH)_3+H_2O, \quad \text{(Eq. 2.4)}$$

$$Si(OH)_4+(OC_2H_5)_4Si \xrightarrow{OH^-} (OH)_3Si\text{-}O\text{-}Si(OC_2H_5)_3+C_2H_5OH. \quad \text{(Eq. 2.5)}$$

An important aspect of our research is the study of size-dependent phenomena of confined liquids. To produce sol-gel glasses with various pore sizes, a series of systematic variations, such as changing amounts of catalysts and varying the molar ratio of reactants, have been performed. Our results demonstrate that to synthesize sol-gel glasses with small pore size (>2 nm and < 4 nm), the molar ratio of TEOS : water : ethanol : acid : base should be kept at 1 : 24 : 2 : 0.002: 0.002.

(2) Gelation

As sols are colliding, the water is consumed and the alcohol evaporates, making the density of the solution reach the point at which a semi-solid 3D structure is formed. This 3D structure is the gel.

The physical characteristics of the gel depend greatly on the size of sols and the extent of cross-linking prior to gelation. The pores of the sol-gel glass are formed during the gelation step. These pores are filled with water and alcohol and can change their shape and size upon the removal of the solvent. Because the negative surface charge can create a repulsive barrier that stabilizes the entire gel structure, the final gel structure prefers to have many deprotonated silanol groups at the surfaces.

(3) Aging and drying

Further condensation of sols after the formation of the gel is called aging. Aging is achieved when sols re-precipitate into more favorable positions in the gel network. The porosity of the gel decreases and the strength of the gel increases during aging. To ensure that a stable gel structure holds together in the subsequent processes, the gel must be aged for a sufficient amount of time.

Drying is a process during which the remaining water and alcohol are removed from the wet gel. When the solvent is removed from the gel, the gel shrinks, leaving small voids inside of its solid glassy structure. Because larger pores are vacated prior to smaller ones, an internal pressure gradient is formed within the gel, potentially creating cracks and fractures in the final structure. This phenomenon can cause a structural collapse of the final glass. This phenomenon can be avoided by evaporating the solvent slowly. Dry gels obtained by this method are called xerogels. The pore diameters of xerogels are smaller than those of wet gels.

(4) Firing

Firing refers to the high-temperature treatment of sol-gel glasses. This process is often performed in a furnace at temperatures in the range between 500 °C to 1200 °C. After firing, the density of the solid portion of the sol-gel glass becomes close to that of fused silica or fused quartz. The choice of firing temperature can determine the pore diameter, the connectivity, and the surface area of the sol-gel glass.

2.3.1 Synthesis of the sol-gel glass

The preparation of the sol-gel glass begins with the two-step, acid-base catalyzed hydrolysis of TEOS (98% TEOS, Acros Organics). A mixture of deionized

water (28.9 ml), ethanol (7.5 ml), and 98% TEOS (28.9 ml) is stirred in a 250-ml, round-bottom flask. An oil bath is used to maintain the reaction temperature at 40 °C. After being stirred for 15 minutes, the solution is acidified with 0.002 moles of HCl. The transparent solution is then cooled to room temperature. Another 28.9 ml of deionized water, 7.5 ml of ethanol, and an amount of base are added to the solution to initiate the condensation of sols. For the smallest pore size, the amount of base added is 0.002 mol. For larger pore sizes, this amount can increase in 0.001 mol increments; however, an amount of base above 0.008 mol can cause the condensation to occur too quickly. Before the density of the solution gets to the gel point, the solution is carefully distributed into 1.5-cm-diameter polystyrene vials. These vials are then capped. Gelation generally occurs within 40 minutes after the solution is transferred into these vials.

The vials are incubated at different temperatures for at least one week to complete the aging process. To obtain sol-gel glasses with pore diameters of 2 to 4 nm, aging takes place at room temperature. To obtain sol-gel glasses with medium pore diameters of 4 to 6 nm, the sample vials are kept in a 60 ^{o}C oven for one month. To produce sol-gel glasses with pore diameters larger than 6 nm, gels should be placed in a 60 ^{o}C oven for one month and further immersed in 0.1 M NH_4OH for 24 hours after aging.

In the drying stage, the solvent is evaporated gradually by covering the vials with perforated Parafilm®. To avoid internal pressure caused by fast evaporation, drying must be performed at room temperature for a period of at least 30 days. The entire gel structure shrinks during the drying process.

The final step is to fire the dry monolith in a muffle furnace at 800 ºC for 6 hours. To avoid fractures and cracks caused by fast temperature ramping, the ramping rate of the temperature is restricted to 0.5 ºC/minute. Gels first become brown and then turn transparent. A picture of a partially fired sol-gel glass and the final product is shown in Figure 2.3.

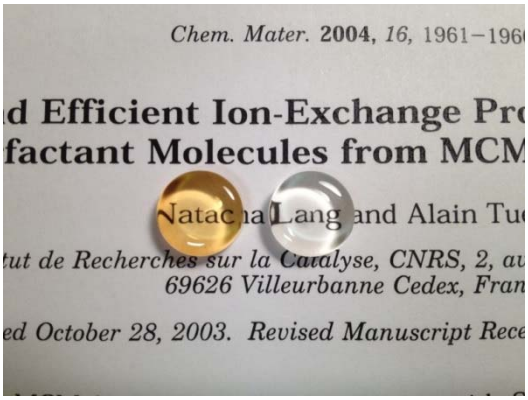

Figure 2.3 Sol-gel monoliths as they appear half way through the firing (left) and after the firing (right).

2.3.2 Characterization and modification of sol-gel glasses

The porosity and the surface area of the sol-gel glass are determined by a Brunauer-Emmett-Teller (BET)[54] sorptometer. (All of the porous glasses used in my experiments were characterized by a commercial BET sorptometer: Micrometrics TriStar 3020.) The sorptometer measures pore sizes based on the BET theory of multi-molecular adsorption.[54] This theory explains qualitatively many of the common features of gas adsorption isotherms and gives a quantitative measure of the surface area of the adsorbent. In BET measurements, nitrogen is usually used as the adsorbate due to its high purity, low cost, and relatively strong interaction with most solids as compared to other gases.

The surfaces of the sol-gel glasses have between 2 to 6 silanol groups per nm^2. This hydrophilic surface can be turned into a hydrophobic one through a silanization reaction. Trimethylchlorosilane (TMCS) (Gelest Inc.) is the reagent we use in the modification of the sol-gel glasses.

Before the modification reaction, sol-gel glasses are placed in a 100-ml, three-neck, round-bottom flask and dried with the flask in an oven for 4 hours. After the drying, the flask and sol-gel glasses are cooled to room temperature in a desiccator. The flask then has two of its necks sealed with rubber septa, leaving the third one connected to a refluxing column. A 50% solution of TMCS in dry toluene is then injected into the flask through one of the rubber septa. The mixture of TMCS and toluene is then refluxed at 110 °C for 4 days. During the reaction, the nitrogen gas is purged into the flask continuously to prevent water from contacting the reagents. After the reaction, TMCS molecules are anchored covalently to the surface silanol groups with their methyl groups pointing away from the surface. The surface is therefore hydrophobic. The sol-gel glass is then washed sequentially with toluene, benzene, and methanol. To remove any remaining volatile impurities, the sol-gel glasses are kept in a vacuum oven at 100 °C for at least 24 hours. The success of the surface treatment can be verified using IR spectroscopy.

2.3.3 Preparation of samples of confined liquids

Monoliths obtained through the sol-gel process are typically cylinders that are 10 mm in length. The sample cuvettes are transparent quartz cells with a 1- or 2-mm path length. To make the sol-gel monolith fit into the sample cuvette, first we use a diamond saw to cut the monolith into 5-mm-thick pieces. The 5-mm-thick

monolith is then ground into a disk of approximately 2 mm thickness using sand papers with different grits. Diamond pastes with grades of 15 μm, 6 μm, and 1 μm are then used to polish the disk gently until the disk has the high optical quality. Because some organic impurities (most likely the colored dyes in the diamond paste) can be absorbed into the pores of the sol-gel glass during the polishing, the disk is washed with organic solvent immediately after polishing. The polished and washed disk is then placed in a programmable furnace and fired at 500 °C for at least 48 hours to remove contaminants. To avoid cracks caused by fast heating, the temperature of the furnace increases at a rate of 0.5 °C/min. After heating, the disk is sealed in the 2-mm-pathlength cell along with the pre-distilled and pre-filtered sample liquid. The disk is then allowed to soak in the sample liquid for at least 24 hours before performing optical experiments.

For experiments on bulk liquids, the liquid in use is distilled and filtered multiple times through a 0.1-μm MilliPore filter before being transferred into the 1-mm-path-length cuvette. The sample cuvette is then capped, sealed, and used in our OKE experiments.

2.4 Data acquisition and analysis

LabView programs that are interfaced with instruments through a GPIB controller are used in all instrument control, data acquisition, and data analysis processes.

The OKE data are collected at two scan lengths, each with its own fixed-point spacing. To capture the slower molecular diffusive orientation, long-time scans are taken with a point-spacing of 66.7 fs. These long-time scans start from negative

delay time and stop when the signal has effectively decayed to zero. To acquire the OKE signal with high resolution, scans with a shorter time step (0.667 fs) are collected. These short-time scans start before zero delay time and are stopped after a few picoseconds of delay. For each sample, at least twenty long-step scans and four short-step scans are obtained and averaged into two separate data files. Between consecutive scans, the computer rotates the first polarizer on the path of the probe beam to switch the heterodyne angle.

Because the OKE signal is the negative time derivative of the collective orientational correlation function,[6] to find the orientational correlation times, the first step in data analysis is to integrate the long data. During the integration, the constant of integration is determined by ensuring that the correlation function decays exponentially at long times. The integrated data are fit by a nonlinear least-squares method to obtain the collective orientational correlation times and their corresponding amplitudes. An extrapolated tail calculated from these collective orientational correlation times is added to the short data to make up a set of data with a point spacing of 0.667 fs. Through this procedure, the nuclear response can be determined with high resolution and the time needed for collecting one set of data with high resolution is greatly shortened.

The SHG cross-correlation data are collected with 0.667-fs point spacing from delay times of -0.3335 ps to 0.3335 ps. To perform the Fourier-transform deconvolution, the cross-correlation data are padded with zeros to make their length the same as that of the concatenated data. The deconvolution process can help to

eliminate the effects of finite pulse length from the OKE data. The deconvolved OKE data are then Fourier transformed back to the time domain.

The component of the orientational diffusion in the OKE signal can be approximated by

$$r(t) = A\left[e^{\left(-\frac{t}{\tau_{or1}}\right)} + e^{\left(-\frac{t}{\tau_{or2}}\right)}\right]\left[1 - e^{\left(-\frac{t}{\tau_r}\right)}\right], \qquad \text{(Eq. 2.6)}$$

where τ_{or1} and τ_{or2} are the collective orientational correlation time constants that are obtained from the fitting of the long data. τ_r is the rise time for reorientation (usually assumed to be 200 fs in our experiments).

To obtain the RSD, Eq. 2.6 is subtracted from the time-domain OKE data. The resultant data are again Fourier transformed. Because the nuclear response is zero before time zero, it contributes only to the imaginary part of the spectrum. This imaginary part of the frequency-domain spectrum is the RSD. An example of a RSD is shown in Figure 1.4. Because the intermolecular modes are located at low frequency and any high-frequency features are ascribed to the intramolecular modes, we often study the RSD in the frequency range from 0 cm^{-1} to 300 cm^{-1}.

Chapter 3: Assessing the Role of Moment of Inertia in Optical Kerr Effect Spectroscopy

3.1 Introduction

OKE spectroscopy is a time-domain analogue of the low-frequency Raman spectroscopy.[55,56] OKE decays can be transformed into Bose-Einstein-corrected, low-frequency Raman spectra,[11] which can be further used in calculating the reduced spectral density (RSD). The RSD carries information regarding Raman-active intermolecular dynamics in the frequency region from 0 cm^{-1} to ~300 cm^{-1}.

Although it is well established that librations and interaction-induced (II) scattering from hindered rotations and translations can contribute to the RSD, the interpretation of the RSD is challenging due to its relatively featureless line-shape. As I mentioned in Chapter 1, to understand the line-shape of the RSD, a sum of two functions is often used to fit the RSD. One of the fitting functions is called the antisymmetrized Gaussian (AG) function:

$$g_{AG}(\omega) = \exp\left(-\frac{(\omega-\omega_1)^2}{2\sigma^2}\right) - \exp\left(-\frac{(\omega+\omega_1)^2}{2\sigma^2}\right). \qquad \text{(Eq. 3.1)}$$

The AG function[46] is postulated to arise from librational scattering in liquids.

The other function is the Bucaro-Litovitz[13] (BL) function:

$$g_{BL}(\omega) = \omega^{\delta}\exp\left(-\frac{\omega}{\omega_0}\right). \qquad \text{(Eq. 3.2)}$$

In molecular liquids, it is often assumed that the BL component arises from II scattering and reflects both the hindered translational and rotational motions.

Various simulation studies have also attempted to determine the microscopic origin of RSDs. Although some simulations have appeared to be consistent with the empirical fits, the results of different simulations have not been consistent. For example, one simulation of benzene concluded that the RSD arises mostly from single-molecule librational motions,[57] whereas another one suggested that hindered translations contribute significantly.[58] The relative importance of different scattering mechanisms in simulations appears to depend significantly on the polarizability model employed, as well as on the manner in which different contributions are calculated.[59]

Previous experimental work from our group has suggested that depolarized OKE RSDs are considerably more sensitive to molecular shape and polarizability than to intermolecular structure.[30] For instance, we have found that liquids with similar shapes but significantly different intermolecular interactions, such as benzene and pyridine, have RSDs with nearly the same shape.[30] In addition, liquids that are known to contain sizable voids[60] (such as tetrahydrofuran) have RSDs that are similar to those for liquids with molecules of approximately the same shape (such as cyclopentane), even when the latter liquids are known not to contain sizable voids.[60] On the other hand, molecules with similar shapes but different polarizability magnitudes and distributions, such as tetrahydrofuran and furan, have significantly different RSDs. Recent work by Meech and Heisler[61] describes a similar picture for isotropic OKE RSDs. The fact that molecular shape and polarizability

play such a prominent role in the shapes of RSDs underscores the difficulties inherent in trying to extract information regarding intermolecular structure and dynamics from RSDs.

Even though molecules with similar shapes but different polarizabilities can have significantly different RSDs, there may still be useful information to be gained by comparing the RSDs of molecules with similar shapes and similar polarizabilities. For instance, we have shown previously that the depolarized RSDs of benzene and benzene-d_6 are virtually identical when scaled by the ratio of the square roots of their moments of inertia.[62] We have observed the same behavior to hold for the depolarized RSDs of pyridine and pyridine-d_5, as well as for other pairs of related liquids.[30] These observations suggest that librations dominate the higher-frequency portion of the RSDs of these liquids. Heisler and Meech found a linear relationship between the inverse of the square root of the molecular weight and the first moment of the isotropic RSDs for a range of aromatic liquids.[61] This observation highlights the potential importance of hindered translations in the lower-frequency range of the isotropic RSDs for these liquids.[61]

Here, we present the results of an OKE study of benzene and four of its isotopologues: C_6D_6, $C_6H_3D_3$, $^{13}C_6H_6$, and $^{13}C_6D_6$. In all cases, the higher-frequency portion of the RSDs can be superimposed by scaling the frequency by the ratio of the moments of inertia. Empirical fits to the sum of a BL function and an AG function suggest that even at the lowest frequencies the RSDs are dominated by scattering from hindered rotations. For isotopologues with six ^{13}C atoms, we

observe a surprising enhancement of the RSD at low frequencies. In addition, analysis of the collective orientational correlation times for the different isotopologues reveals a clear signature of strong translation−rotation coupling in liquid benzene.

3.2 Experiments

Benzene (EMD Chemicals, 99%), benzene-1,3,5-d_3 (Cambridge Isotope Laboratories, 98%), benzene-d_6 (Cambridge Isotope Laboratories, 99.5%), $^{13}C_6H_6$ (Cambridge Isotope Laboratories, 99%), and $^{13}C_6D_6$ (Isotec, 99%) were used as purchased without further purification. The liquids were sealed in cuvettes with a 1-mm path length. All data were collected at a temperature of 295 K.

Detailed descriptions of the OKE experimental setup and procedure for data acquisition were given in Chapter 2. Data sets were collected in pairs at positive and negative heterodyne angles of equal magnitude. Time-domain spectra were collected by scanning the delay line out to a delay time of 40 ps with a step size of 66.7 fs. Additionally, short-time scans, with a step size of 0.667 fs, were collected out to a delay time of 4.7 ps, to provide more details in this region of the OKE decay. For each sample, 20 long-step scans and 4 short-step scans were recorded.

RSDs were derived from the time-domain data using the Fourier-transform deconvolution method of McMorrow and Lotshaw[11] that has been discussed previously. A MATLAB program was used to find the best parameters for fitting RSDs to the sum of a BL function and an AG function. The RSDs were fit from 0 to 300 cm^{-1}. MATLAB was also used to determine the frequency scaling factors between the experimental RSDs for different isotopologues and that of benzene. The pro-

gram performed a point by point match between the benzene RSD and the frequency-scaled RSD for another isotopologue until the difference between these two sets of data had converged. This procedure was used for benzene RSD frequencies from 50 to 300 cm^{-1}. Error bars in the scaling factors were determined by performing scaling with a ±2% deviation in the normalization constant of the isotopologue RSDs.

3.3 Results and Discussion

The time-domain OKE data are shown over a period of 15 ps in Figure 3.1. The natural logarithm of the long-time OKE decay of benzene and its isotopologues is linear, as shown in Figure 3.1. This linearity shows that the long-time OKE decay can be described by a single exponential decay function. This behavior indicates that the long-time tails of these OKE decays all arise solely from the collective reorientation of molecules. The time constant of this exponential is the collective orientational correlation time, which we denote as τ_o.

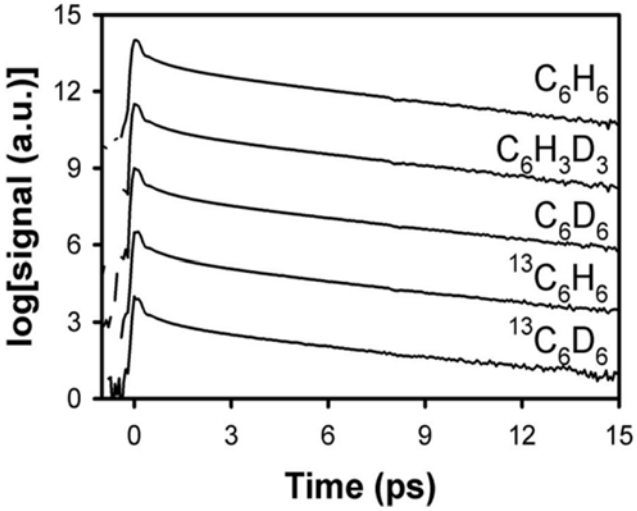

Figure 3.1 Natural logarithm of the OKE decays for benzene and its isotopologues over the first 15 ps of the decay. The data have been offset for clarity.

For liquids studied in this chapter, there is generally an exponential component in the OKE decay with a time scale that is shorter than that for orientational diffusion. The time constant related to this exponential is called the "intermediate" response time, which we denote as τ_i.

In Table 3.1, we give the molecular weight, the tumbling moment of inertia, and τ_o for each isotopologue studied in this chapter. We also list the values of τ_i in Table 3.1, as well as the relative amplitudes and ratio of time constants for these two exponentials. It was found previously that there is a strong linear correlation between τ_o and τ_i,[30,45,63,64] which led to the suggestion that the intermediate response is related to motional narrowing.[64] The constant of proportionality between τ_o and τ_i is generally found to be on the order of 2.5 to 5, which holds for the liquids studied here as well.

Table 3.1 Molecular properties and fitting parameters for the integrated OKE signal of benzene and its isotopologues. This table contains molecular weight (MW), tumbling moment of inertia (I_{tumb}), collective orientational correlation time (τ_o), intermediate response time (τ_i), ratio of relaxation times, and ratio of relaxation amplitudes (numbers in parentheses are uncertainties in the last digits).

Liquid	MW (amu)	I_{tumb} (amu•Å^2)	τ_o (ps)	τ_i (ps)	τ_o/τ_i	A_o/A_i
C_6H_6	78.11	86.1	2.80(7)	0.79(9)	3.5(3)	0.71(5)
C_6D_6	84.15	104.4	3.02(8)	0.85(8)	3.6(3)	0.77(5)
1,3,5-$C_6H_3D_3$	81.13	95.3	2.95(8)	0.88(9)	3.4(3)	0.71(5)
$^{13}C_6H_6$	84.07	91.8	2.98(8)	0.84(8)	3.5(3)	0.73(5)
$^{13}C_6D_6$	90.1	110.1	3.27(8)	0.97(9)	3.4(3)	0.75(5)

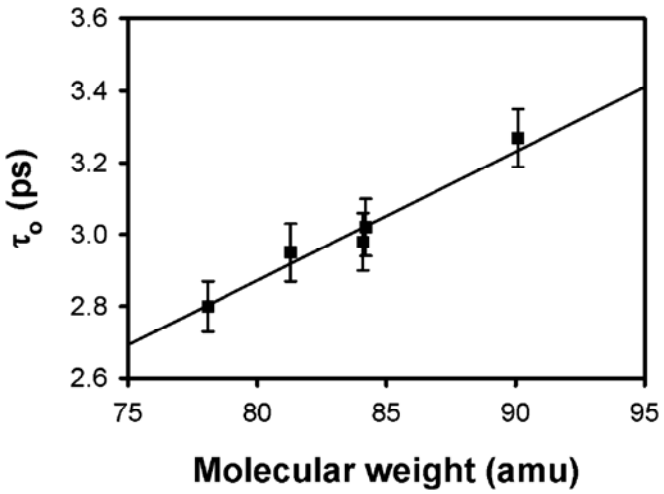

Figure 3.2 Collective orientational correlation times (τ_0) as a function of molecular weight. The line is a linear least-squares fit that passes through the origin.

In Figure 3.2, we plot the collective orientational correlation time as a function of molecular weight. A linear least-squares fit of these data has an intercept

that is close to the origin, and so in the fit shown in Figure 3.2 we have constrained the line to pass through the origin. It is surprising that the collective orientational correlation times scale directly with molecular weight, as molecular weight is not generally a factor that comes into models of orientational diffusion.

One common model for the orientational correlation time in a liquid is the Debye−Stokes−Einstein[35] (DSE) equation:

$$\tau_0 = \frac{V_H \eta}{k_B T} + c, \qquad \text{(Eq. 3.3)}$$

where V_H is the hydrodynamic volume of the molecule, η is the viscosity, k_B is Boltzmann's constant, T is the temperature, and c is a constant that describes the diffusive orientational correlation time at zero viscosity. Molecular weight does not appear explicitly in this expression, and the only parameter in which it might reasonably play a role is the viscosity. In gases, the viscosity generally scales with the square root of molecular weight, and in polymer solutions, it scales with the molecular weight to a fractional power.[65] In small-molecule liquids, the viscosity of isotopologues is also predicted to scale with the square root of molecular weight.[65] The range of molecular weights of the isotopologues studied here is not large enough to distinguish unequivocally between proportionality to molecular weight and the square root of molecular weight. However, a logarithmic plot of the orientational correlation time as a function of molecular weight has a slope of 1.03, which strongly supports a linear proportionality.

It has also been suggested that, for small-molecule liquids that feature significant translation−rotation coupling, the viscosity should scale with the square root of the moment of inertia.[66] To test this idea, in Figure 3.3, we plot the collective

orientational correlation time as a function of the square root of the moment of inertia. As can be seen from this plot, there is indeed a strong linear correlation between τ_o and the square root of moment of inertia. The line is a linear least-squares fit to the data, which was again constrained to pass through the origin. A logarithmic plot of τ_o versus the moment of inertia has a slope of 0.52, supporting the square-root relationship.

Previous measurements of the translational diffusion constant of benzene and benzene-d_6 found a ratio that was somewhat greater than the square root of the ratios of molecular weights but considerably less than the ratio of the square roots of the moments of inertia.[66] It was therefore suggested that translation−rotation coupling is not strong in benzene. However, our results for the collective orientational correlation times of a larger number of isotopologues show excellent agreement with scaling based on the square root of the moment of inertia, which implies that benzene does exhibit significant translation−rotation coupling.

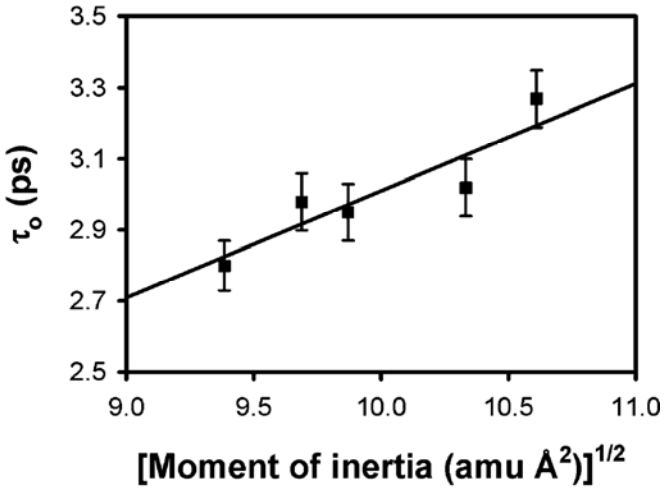

Figure 3.3 Collective orientational correlation times (τ_0) as a function of the square root of the tumbling moment of inertia. The line is a linear least-squares fit that passes through the origin.

We should note that, according to the DSE equation (Eq. 3.3), τ_o is not necessarily directly proportional to viscosity, insofar as the intercept *c* in this equation may not be zero. Measurements of the temperature dependence of the viscosity and the orientational correlation time are needed to determine the value of *c* for a liquid. No such information is available for the benzene isotopologues studied here. However, based on previously reported data for benzene,[64] we can determine a value of *c* for this liquid that is approximately 0.42 ps. If we assume, in a worst-case scenario, that the value of *c* is similar for each of the isotopologues studied here, we can test whether the dependence of the orientational correlation time on molecular weight or moment of inertia changes significantly. For both molecular weight and moment of inertia, the slope of a logarithmic plot increases by about 20% using this correction to calculate the viscosity. These changes in slope are relatively small, and do

not alter our conclusions regarding the importance of translation−rotation coupling in benzene.

Another means of estimating how *c* might vary for isotopologues is to consider a molecule for which the orientational correlation time and viscosity have been measured for two or more isotopologues. We have previously used OKE spectroscopy to measure the temperature-dependent, collective orientational correlation times for acetonitrile and acetonitrile-d_3.[64] Temperature-dependent viscosity data are also available for each of these liquids. DSE plots for the two liquids reveal that, within the experimental uncertainty, *c* scales with both molecular weight and the square root of the moment of inertia for these acetonitrile isotopologues. If the same scalings hold for the value of *c* for benzene, then linear scaling of τ_o with molecular weight and with the square root of moment of inertia found for the uncorrected viscosity will be unchanged for the corrected viscosity, which has taken the value of c into account.

The depolarized RSDs for the five liquids studied here are shown in Figure 3.4(a). As expected, the shapes of all of the RSDs are highly similar. The width of the RSD varies from liquid to liquid, although the total variation in width is less than 15% from the narrowest to the broadest RSD. Shown in Figure 3.4(b) are the same RSDs with the frequency axes scaled to have the best overlap with the benzene RSD. The overlap among the RSDs is excellent at frequencies of 50 cm^{-1} and above.

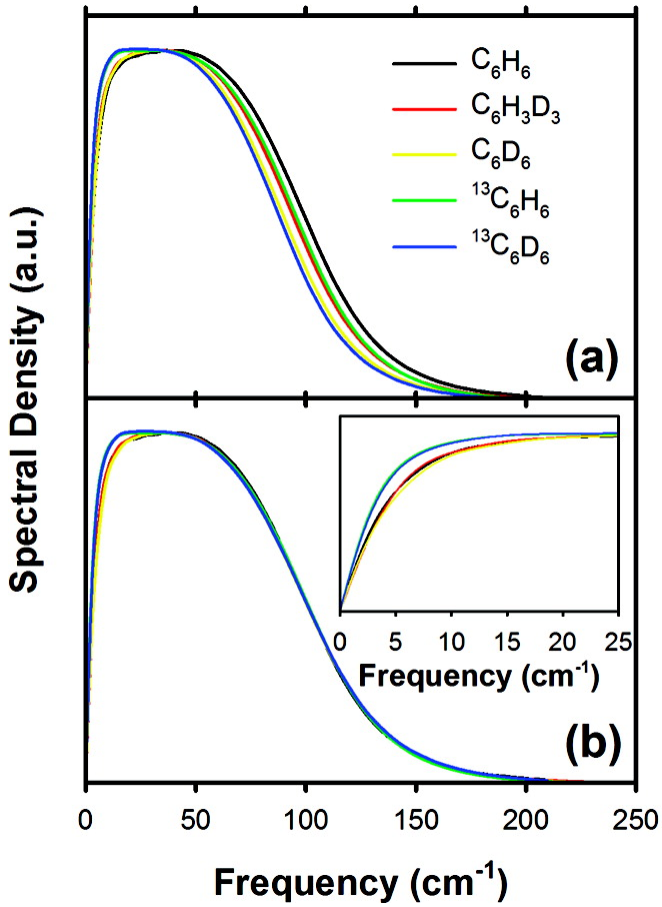

Figure 3.4 Normalized (a) RSDs and (b) RSDs with frequencies scaled for maximum overlap for benzene and its isotopologues: benzene (black), 1,3,5-benzene-d_3 (red), benzene-d_6 (yellow), $^{13}C_6H_6$ (green), and $^{13}C_6D_6$ (blue). The inset in (b) focuses on the scaled RSDs at frequencies of 25 cm^{-1} and less.

The frequency of a librational mode of a single molecule scales inversely with the square root of the molecule's moment of inertia. For a hindered translational mode of a single molecule, the frequency scales inversely with the square root of the molecular weight. In Figure 3.5(a), we show the RSDs frequency-scaled to that of benzene by the ratios of square roots of moments of inertia, and in Figure

3.5(b), we scale instead by the ratio of square roots of molecular weight. The overlap among the RSDs in Figure 3.5(a) looks better than the overlap among the RSDs in Figure 3.5(b).

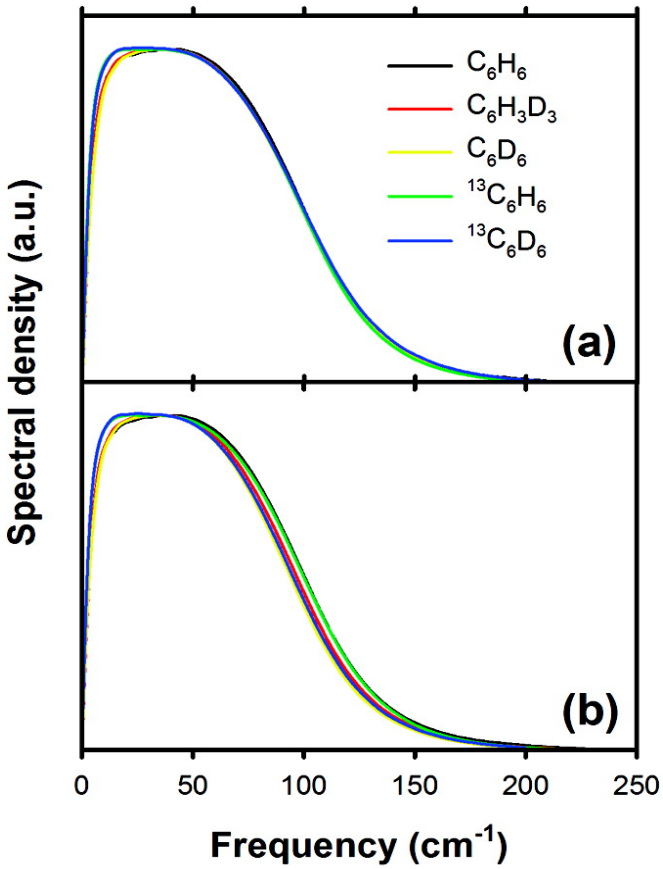

Figure 3.5 Scaled normalized RSDs with frequencies scaled by (a) the inverse square root of the moment of inertia relative to that of benzene and (b) the inverse square root of molecular weight relative to that of benzene: benzene (black), 1,3,5-benzene-d_3 (red), benzene-d_6 (yellow), $^{13}C_6H_6$ (green), and $^{13}C_6D_6$ (blue).

In Figure 3.6, we plot the observed frequency-scaling factor versus the scaling factors calculated on the basis of the moment of inertia and those calculated on the basis of molecular weight. It is further clear from this plot that the moment of

inertia scaling is virtually identical to the observed scaling, whereas the molecular weight scaling does not match the observed scaling well. These results suggest that the RSDs are dominated by librational scattering at the higher frequencies. This finding is in good agreement with our previous results for benzene and benzene-d_6[63] as well as for other pairs of related liquids.[30]

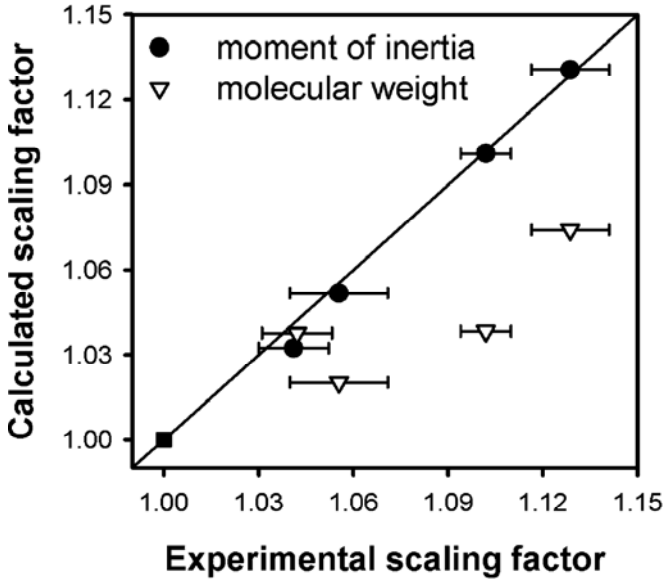

Figure 3.6 Frequency scaling factors based on moment of inertia (circles) and molecular weight (triangles) as a function of experimental scaling factors. The square represents the value for benzene, which by definition is unscaled. The line represents the points for which the experimental and calculated scaling factors are equal.

It has been noted previously that there is a high degree of similarity between the RSDs of biphenyl and benzene, even though biphenyl is twice as large as benzene and has a considerably larger moment of inertia.[67] Tao and Stratt developed a compelling argument to explain this observation.[68] They began by modeling these

molecules as being composed of equivalent effective atoms of mass *m* and suggested that for benzene and biphenyl these effective atoms could be viewed as C−H units. They also assumed that the fluctuating forces felt by each effective atom were statistically independent. Within this model, the moment of inertia about an axis in the plane of the molecule is given by[68]:

$$I_\alpha = m \sum_{i=1}^{N} \alpha_i^2, \qquad \text{(Eq. 3.4)}$$

where $\alpha = x$ or y (the two perpendicular axes in the plane of the benzene molecule) and N is the number of effective atoms in the molecule. They also showed that within this model the torque about axis α (which we denote here as T_α) follows

$$\langle T_\alpha^2 \rangle = f_\perp^2 \sum_{i=1}^{N} \alpha_i^2, \qquad \text{(Eq. 3.5)}$$

where $f_\perp$ is the magnitude of the fluctuating force perpendicular to the molecular plane. The Einstein frequency for libration is then given by

$$\omega_\alpha = \sqrt{\frac{\langle T_\alpha^2 \rangle}{I_\alpha k_B T}} = \sqrt{\frac{f_\perp^2}{m k_B T}}\,. \qquad \text{(Eq. 3.6)}$$

The result of this analysis is that the librational frequency depends on the mass of the effective atom rather than on the moment of inertia. Tao and Stratt further showed that the predicted librational frequency for biphenyl yields the same result, which explains why the RSDs of benzene and biphenyl are nearly identical.[68]

Although the above model was not developed to describe RSDs of isotopologues, (Eq. 3.6) might be taken to imply that the librational contribution to RSDs should scale with the inverse square root of molecular weight (with the molecular weight being proportional to the mass of the effective atomic units when comparing

isotopologues). However, as we have noted previously for benzene and benzene-d_6[63] and pyridine and pyridine-d_5,[30] as well as here for a range of benzene isotopologues, the scaling of the higher-frequency portion of the RSD matches quite closely with the inverse square root of the moment of inertia and poorly with the inverse square root of the molecular weight.

To resolve this apparent discrepancy, we consider the factors in Tao and Stratt's model that change in isotopologues of benzene and compare the full tumbling moment of inertia of a benzene isotopologue with that calculated with the effective-atom model of Tao and Stratt. The full moment of inertia about an axis of a molecule is given by

$$I_\alpha = \sum_{i=1}^{N} m_i \alpha_i^2, \qquad \text{(Eq. 3.7)}$$

where the index *i* refers to an individual atom, *N* is the number of atoms, m_i is the mass of atom *i*, and α_i is the value of the coordinate for atom *i*. In the case of benzene we can rewrite the moment of inertia as

$$I_\alpha = m_C \sum_{i=1}^{6} \alpha_{C,i}^2 + m_H \sum_{i=1}^{6} \left(\alpha_{C,i} + \alpha_{bond,i}\right)^2$$

$$= (m_C + m_H) \sum_{i=1}^{6} \alpha_{C,i}^2 + m_H \sum_{i=1}^{6} (2\alpha_{C,i}\alpha_{bond,i} + \alpha_{bond,i}^2), \qquad \text{(Eq. 3.8)}$$

where *bond, i* is the α projection of the relevant C-H bond, $\alpha_{C,i}$ is the coordinate of carbon atom *i*, and m_C and m_H refer to the masses of the carbon and hydrogen isotopes in question, respectively.

In the effective-atom model, the coordinate of the center of mass of a specific effective atom is given by:

$$\alpha_i = \alpha_{C,i} + \frac{m_H}{m_C+m_H}\alpha_{bond,i}\,. \qquad \text{(Eq. 3.9)}$$

We also assume that the mass of the effective atom is given by $m_C + m_H$. The moment of inertia in this approximation, I_α^*, is given

$$I_\alpha^* = (m_C + m_H)\sum_{i=1}^{6}\left(\alpha_{C,i} + \frac{m_H}{m_C+m_H}\alpha_{bond,i}\right)^2$$

$$= (m_C + m_H)\sum_{i=1}^{6}\alpha_{C,i}^2 + m_H\sum_{i=1}^{6}(2\alpha_{C,i}\,\alpha_{bond,i} + \frac{m_H}{m_C+m_H}\alpha_{bond,i}^2)\,. \qquad \text{(Eq. 3.10)}$$

The difference between two of the moment of inertia is given by

$$I_\alpha - I_\alpha^* = m_H\sum_{i=1}^{6}(1 - \frac{m_H}{m_C+m_H})\alpha_{bond,i}^2$$

$$= m_H\sum_{i=1}^{6}(\frac{m_H}{m_C+m_H})\alpha_{bond,i}^2 = \sum_{i=1}^{6}(\frac{m_C m_H}{m_C+m_H})\alpha_{bond,i}^2$$

$$= \sum_{i=1}^{6}\mu\alpha_{bond,i}^2\,, \qquad \text{(Eq. 3.10)}$$

where μ is the reduced mass of the actual atoms that comprise the effective atom. This term represents a relatively small portion of the moment of inertia, and so there is near agreement between the full result and the result within the approximation of Tao and Stratt.[68]

Changing the isotope of one type of atom in benzene can change both the mass *m* and the position of the effective atoms. However, the shapes of the benzene isotopologues are essentially identical, and so the positions at which the fluctuating forces (and therefore the torques) are felt should remain unchanged among isotopologues to first approximation. Thus, the ratio of the librational frequency of an isotopologue to that of benzene can be written as:

$$\frac{\omega_{\alpha,iso}}{\omega_{\alpha,ben}} = \frac{\sqrt{\frac{\langle T^2_{\alpha,iso}\rangle}{I_{\alpha,iso}k_BT}}}{\sqrt{\frac{\langle T^2_{\alpha,ben}\rangle}{I_{\alpha,ben}k_BT}}} \cong \sqrt{\frac{I_{\alpha,ben}}{I_{\alpha,iso}}}, \qquad \text{(Eq. 3.11)}$$

where the subscript iso denotes an isotopologue and *ben* denotes benzene. At this point, there is no need to employ the effective-atom model to evaluate the ratio of moments of inertia. However, if the ratio is evaluated in this manner, changes in the masses of the constituent atoms lead to changes in the positions of the effective atoms. As a result, the ratio of the moments of inertia does not reduce to a ratio of the masses of the effective atoms but rather is quite close to the ratio of the full moments of inertia. Thus, for molecules that are composed of the same effective atoms in different configurations, the librational frequency is expected to be relatively insensitive to molecular structure. However, for isotopologues, the librational frequency is expected to scale with the inverse of the square root of the moment of inertia, as observed here.

Although scaling by the inverse square root of the moment of inertia leads to RSDs that are highly similar to one another for the isotopologues studied here, a small but interesting effect is apparent in Figure 3.4(b): While the RSDs for isotopologues with six ^{13}C atoms can be superimposed by frequency scaling, they differ noticeably from the scaled RSDs of the other isotopologues at frequencies less than 30 cm^{-1}. The $^{13}C_6$ isotopologues have a somewhat higher spectral density in this region than do the other isotopologues studied here.

The reasons underlying the difference in the $^{13}C_6$ isotopologue RSDs at low frequencies are not obvious. We have argued previously that the shape of this region of the RSD is related to motional narrowing.[64] However, as can be seen in Table 3.1, the ratio of τ_o and τ_i and the ratio of the amplitudes of these decays are quite similar for all of the liquids studied here. Accordingly, we would expect the relative degree of motional narrowing to be the same for all of the liquids. It is useful in this regard to compare C_6D_6 and $^{13}C_6H_6$. These liquids have values of τ_o and τ_i that are nearly identical. C_6D_6 has a larger moment of inertia than does $^{13}C_6H_6$, yet after scaling the latter liquid has a larger RSD amplitude at low frequencies. These factors suggest that the vibrational densities of states themselves are higher at low frequencies in the $^{13}C_6$ isotopologues than in the other species studied here.

There is no clear relation between enhancement of the RSD at low frequencies and either the molecular weight or the moment of inertia. For instance, C_6D_6 and $^{13}C_6H_6$ have nearly identical molecular weights, yet only the latter liquid exhibits a low-frequency enhancement of the RSD. As shown in Figure 3.2, there is a linear relationship between molecular weight and the collective orientational correlation time for the isotopologues, but it is only the presence of ^{13}C atoms in our data that is correlated with low-frequency enhancement of the RSD.

We can also consider whether the low-frequency enhancement of RSDs arises from an electronic effect associated with different isotopes. For instance, having six ^{13}C atoms produces a measurable difference in the electron affinity of benzene due to the lower zero-point energy of the molecule,[69] but this effect leads

to a change on the order of 1%. Isotope effects can also play a role in the polarizability of a molecule,[70] but again, these effects are generally small. It is also unclear why any electronic isotope effect would show up only in the low-frequency portion of the RSD.

Isotopic substitutions also affect the vibrational modes of molecules. Although replacing H with D affects primarily the higher-frequency fundamental vibrational modes of a benzene molecule, replacing ^{12}C with ^{13}C lowers the frequencies of all of the vibrational modes. Thus, the population of excited vibrational modes in $^{13}C_6$ molecules will be greater than that of $^{12}C_6$ molecules at room temperature, which in turn will have some influence on the effective molecular shape. This effect again would be expected to be relatively minor, however, as evidenced by the fact that the volume per molecule is virtually identical for all of these isotopologues (based on the densities and molecular weights of the liquids[71]).

We can also discount the influence of any isotopic impurities on the enhancement of the RSD at low frequencies for $^{13}C_6$ isotopologues. Any ^{12}C impurities would lead to lower moments of inertia, and therefore would be expected to shift the RSD to higher rather than lower frequency. Molecules with ^{12}C impurities would also be expected to have slightly lower orientational correlation times, but this effect would not be expected to have any significant influence on the shape of the resulting RSD unless there were a high concentration of impurities. Unraveling the source of the low-frequency enhancement of the RSDs for $^{13}C_6$ species will require further experiments, and it will also be interesting to test whether this effect extends to other molecules.

We next consider fits of the isotopologue data to the sum of a BL function and an AG function, with relative amplitudes of A_{AG} and A_{BL}, respectively. As shown in Figure 3.7, the RSD for benzene can be fit well with these functions, as has been observed previously for benzene[30] and other aromatics.[63] The parameters derived from these fits are listed in Table 3.2.

Table 3.2 Parameters from fits of RSDs of benzene and its isotopologues to a sum of a BL function and an AG function (numbers in parentheses are uncertainties in the last digit).

Liquid	δ	ω_0 (cm^{-1})	ω_1 (cm^{-1})	σ (cm^{-1})	A_{AG}/A_{BL}
C_6H_6	0.82(2)	11.7(6)	51.1(13)	43.3(11)	4.3(2)
C_6D_6	0.90(2)	10.4(5)	42.4(11)	41.3(10)	5.1(2)
1,3,5-$C_6H_3D_3$	0.80(2)	10.8(5)	42.0(11)	44.1(11)	4.0(2)
$^{13}C_6H_6$	0.76(2)	11.2(6)	49.0(12)	41.7(10)	3.3(2)
$^{13}C_6D_6$	0.79(2)	10.0(5)	38.5(10)	41.6(10)	3.6(2)

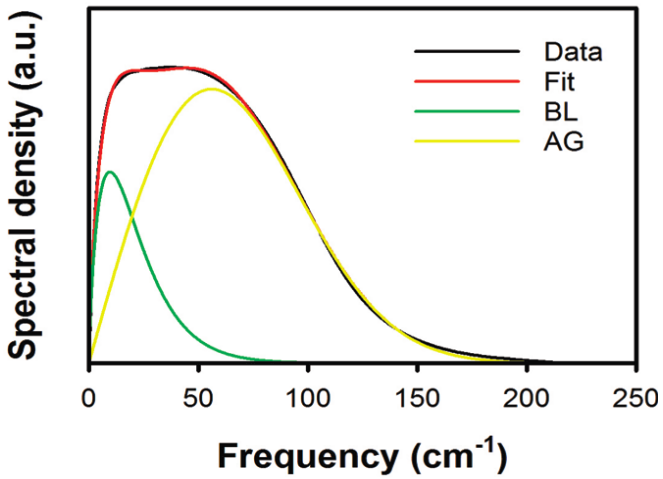

Figure 3.7 Representative fit to the RSD of benzene with the sum of a BL function and an AG function.

Given that all of the RSDs measured here can be scaled to that of benzene at the higher frequencies based on the inverse square root of the moment of inertia, we would expect that the AG portion of the fits would scale in the same manner. To test this idea, in Figure 3.8, we plot the first moment of the AG function in the fits as a function of the inverse square root of the moment of inertia. The predicted scaling is indeed observed, and the intercept of a linear least-squares fit to the data has a *y* intercept that is close to the origin. Accordingly, the intercept was constrained to pass through the origin in the line shown in Figure 3.8.

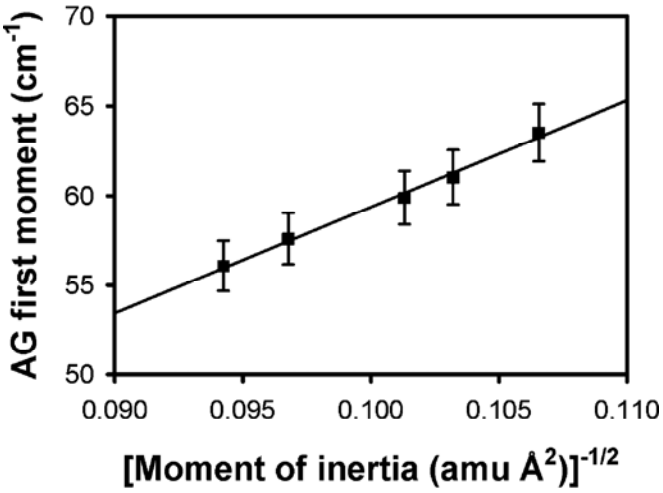

Figure 3.8 First moments of AG portion of fits to the isotopologue RSDs as a function of the inverse square root of the moment of inertia. The line is a linear least-squares fit that was constrained to pass through the origin.

The low-frequency edge of the RSDs does not superimpose with frequency scaling as well as the high-frequency edge does. The differences in the low-frequency portions of the RSDs for the $^{13}C_6$ species account for part of this discrepancy. However, it is also possible that the low-frequency portion of the spectrum has larger contributions from hindered translational motions, which could lead to

scaling based on the inverse square root of the molecular weight rather than the inverse square root of the moment of inertia. To assess these two possibilities, in Figure 3.9 we plot the first moment of the BL portions of the fits as a function of the inverse square root of the moment of inertia and in Figure 3.10 we plot the BL first moment as a function of the inverse square root of molecular weight. The fit based on the molecular weight is slightly better than the fit based on the moment of inertia. However, the linear least-squares fit to the data in Figure 3.9 has a y intercept that passes near the origin (and has been constrained to pass through the origin in the figure). On the other hand, the y intercept of the linear least-squares fit to the data in Figure 3.10 has a y intercept that is far from the origin. These observations suggest that scaling of the BL function based on the inverse square root of the moment of inertia is more appropriate than scaling based on the inverse square root of the molecular weight. The implication of this result is that hindered rotations play a major role throughout the RSD of benzene.

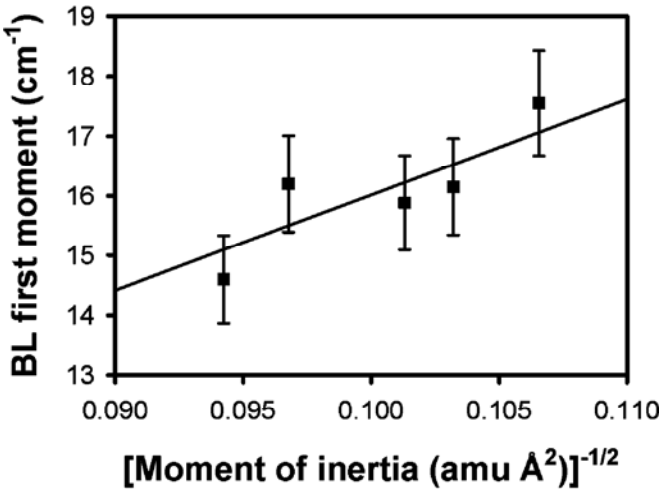

Figure 3.9 First moments of BL fits to the isotopologue RSDs as a function of the inverse square root of the moment of inertia. The line is a linear least-squares fit that was constrained to pass through the origin.

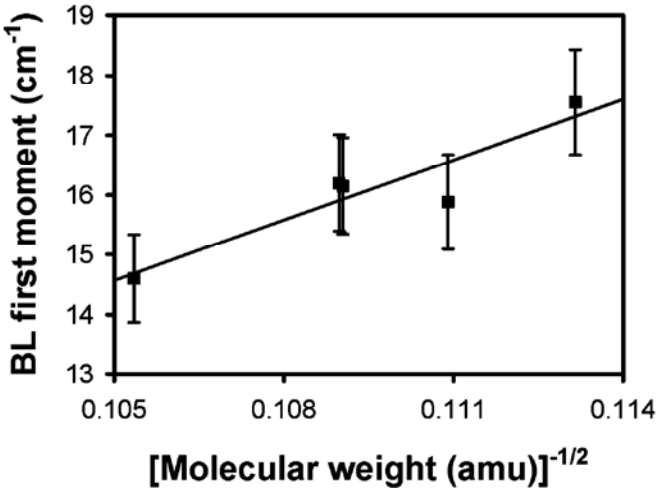

Figure 3.10 First moments of AG fits to the isotopologue RSDs as a function of the inverse square root of the molecular weight. The line is a linear least-squares fit.

The BL function was first developed to describe the shape of depolarized light-scattering spectra in noble-gas fluids,[63] in which all scattering arises from many-body effects. As a result, the BL function in fits to RSDs in molecular liquids

is often proposed to arise from contributions from hindered translations (density fluctuations). Heisler and Meech[63] have shown the BL function can provide good fits to isotropic RSDs in aromatic liquids, and that its first moment scales well with the inverse square root of the molecular weight (although they did not study any isotopologues). Their results suggest that the BL function that describes the isotropic RSDs arises primarily from hindered translations. However, our results tend to suggest that both the BL and AG contributions in depolarized RSDs arise primarily from hindered rotations. How can these observations be explained?

We should first note that the BL function was not developed to describe light scattering in atomic fluids at liquid densities. Indeed, a recent OKE study of these substances at liquid densities has revealed that the depolarized RSD is not described by a BL function.[72] Second, although interaction-induced scattering in noble-gas fluids arises necessarily from hindered translations, in molecular liquids, it can arise equally well from hindered rotations. Different simulation studies have given different pictures of the importance of hindered orientations in the OKE RSD for benzene. Ryu and Stratt[58] found that the II scattering for benzene is strongly dominated by hindered translations. On the other hand, Elola and Ladanyi[59] found that hindered translations play only a minor role in the depolarized OKE spectrum of this liquid. We believe that the differences among these studies reflect the different polarizability models employed. Ryu and Stratt used an anisotropic, point molecular polarizability,[58] whereas Elola and Ladanyi employed a distributed polarizability.[59] Although both types of models have their strong and weak points, we have argued previously[62] that point molecular polarizabilities tend to overestimate the

contribution of hindered translations to II scattering. For instance, using a point molecular polarizability model, Ryu and Stratt found that hindered translations play a major role in the depolarized OKE RSD of CS_2.[58] With a distributed polarizability model, however, we found that hindered rotations dominate even the II portion of this RSD. The experimental results presented here, which suggest that hindered rotations are the major contribution in the low-frequency region of the benzene isotopologue RSDs, are therefore in good accord with simulations based on distributed polarizability models. Additionally, the scaling of the collective orientational correlation time with the inverse square root of the moment of inertia discussed above indicates that there is strong translation−rotation coupling in benzene, which suggests that the nature of the low-frequency modes is highly complex (which is again consistent with simulation).

The far-infrared spectrum of liquid benzene has been compared previously with the OKE RSD and with the low-frequency Raman spectrum.[73] At frequencies of roughly 50 cm^{-1} and higher, there is a strong similarity between the RSD/Raman spectrum and the THz spectrum. This result suggests that, in this frequency range, the single-molecule motions that lead to Raman scattering are closely related to the motions that create the induced dipole moments that generate the THz spectrum. At lower frequencies, the Raman and THz spectra show less agreement. Hindered translational modes can lead readily to induced dipole moments, and so the THz spectrum is expected to contain a substantial contribution from these motions at

low frequencies. Thus, the comparison of these two types of spectra is also suggestive that the low-frequency portion of the OKE RSDs for benzene is dominated by hindered rotations.

In intramolecular Raman spectra, the modes that dominate depolarized spectra can be entirely different from the modes that dominate isotropic spectra. The same effect is likely to hold true for intermolecular spectra. Indeed, although the isotropic RSDs for aromatic liquids measured by Heisler and Meech fit well to BL functions,[61] the BL portions of the fits to depolarized RSDs in some of the same liquids[62] are completely different from the BL fits to the isotropic spectra. The first moments of the BL portions of the fits for the depolarized RSDs of benzene, 1,3,5-trifluorobenzene, and hexafluorobenzene,[62] for example, are approximately a factor of 3 smaller than the first moments for the BL fits to the isotropic spectra[62] in the same liquids. Thus, it is entirely reasonable to assume that the dominant scattering mechanisms in the low-frequency region of the depolarized and isotropic RSDs of the same liquid should be different.

It is also interesting to note that, in a recent study of the RSDs of 20 different aromatic liquids, Shirota and co-workers did not find any obvious correlation between the first moment of the AG function used in fits and the tumbling moment of inertia.[74] Their work reinforces the idea that molecular shape and the distribution of the polarizability both play important roles in determining the shape of the RSD for a liquid.[30] Any changes in shape and polarizability distribution for isotopologues are minor, however, which has allowed us to isolate the effects of moment of inertia on RSDs.

3.4 Conclusion

This chapter has presented depolarized OKE data for a series of benzene isotopologues. The collective orientational times of these liquids scale with the inverse square root of the tumbling moment of inertia, indicating that there is strong translation−rotation coupling in benzene, contrary to what has been found in previous reports that examined only benzene and C_6D_6.[66] The RSDs of all of the isotopologues can be superimposed at frequencies above approximately 50 cm^{-1} by scaling the frequency by the inverse square root of the moment of inertia. We have demonstrated that this result is consistent with the model developed by Tao and Stratt to explain the agreement between the depolarized RSDs of benzene and biphenyl.[68] Empirical fits to the RSDs also suggest the hindered rotations dominate the depolarized scattering over the entire intermolecular spectrum. We have also observed an enhancement in the low-frequency region of the RSDs for isotopologues containing six ^{13}C atoms. The source of this enhancement has not yet been explained adequately and will be an interesting topic for future research.

Chapter 4: Density Effects on the Dynamics of Liquids in Nanoconfinement

4.1 Introduction

Nanoconfined liquids have attracted considerable attention in recent decades.[40] There is a fundamental interest in understanding the physics and chemistry of nanoconfined liquids due to the fact that the properties of these liquids differ substantially from their bulk counterparts. In addition, the vast number of applications of nanoconfined liquids in fields of catalysis, lubrication, separation, oil recovery, and microfluidics also require a deep understanding of these liquids.

Porous materials that have a large surface area are commonly used nanoconfining media. Examples include zeolites,[47] Vycor® glass,[75] porous membranes,[48] and sol-gel glasses.[38] Among these, sol-gel glasses are the superior medium for our OKE studies due to their high optical quality, relatively large surface area, well-controlled pore size, and tunable surface chemistry.[40]

We have performed OKE experiments to study the structure and dynamics of benzene confined in sol-gel glasses previously.[40–43] In these studies, it has been found that benzene molecules in confinement can be divided into two populations: molecules in the pore centers and molecules in the vicinity of the confining surfaces. For benzene molecules that are near the confining surfaces, the orientational dynamics is an order of magnitude slower than that of the bulk liquid, but is independent of the pore diameter. For benzene molecules located in the pore centers,

however, the diffusive orientational dynamics depend on the pore diameter, becoming more rapid with increasing with pore diameter. These results imply that benzene molecules in vicinity of the surfaces exhibit a highly ordered structure, and that the dynamics of molecules in the pore centers can be affected by geometric factors through this structure. Meanwhile, the measured surface-layer thickness of the dynamically inhibited benzene suggests that the benzene molecules lie flat on the silica surfaces.

In this chapter, the OKE RSDs of benzene in nanoconfinement are reported. When RSDs of confined benzene are compared to that of bulk benzene, a blue shift in the high-frequency portion of the confined RSDs (in the frequency region of 50 cm^{-1} to 150 cm^{-1}) is observed. This shift is similar to that observed in bulk benzene with decreasing temperature. A good match between the RSDs of nanoconfinement benzene and the RSDs of bulk benzene can be obtained. It is believed that the similar shift in the RSDs of confined benzene arises from a density change.

To verify that the same shift of the RSD can be observed in other liquids, studies on pyridine and acetonitrile are presented in this chapter. Pyridine was chosen for comparison because it has the same molecular shape as, but different intermolecular structures than, benzene.[76] Acetonitrile is used in this study because it has a rod-like molecular shape, which is different from the disk-like molecular shape of benzene. Hence, a study on acetonitrile can help us to see whether the molecular shape can influence the density effect.

4.2 Experiments

The synthesis, characterization, and modification procedures of the monolithic nanoporous sol-gel glasses were introduced in Chapter 2. The pore diameters of the sol-gel glasses used in these experiments were 7.3 nm, 6.6 nm, 6.2 nm, 5.9 nm, 4.5 nm, 3.3 nm, 2.8 nm, 2.6 nm, and 2.4 nm.

The preparation of the confined liquid samples and the bulk liquid samples was also introduced in Chapter 2. For confined liquid samples, the sample holder was placed on the sample stage with the pump beam and the probe beam focused in the sol-gel monolith and spectra were collected at room temperature. For temperature-controlled experiments on bulk liquids, the samples were sealed and mounted on a brass sample holder in a continuous-flow vacuum cryostat (Janis ST-100). Nitrogen was allowed to flow into the system for at least 2 hours prior to data collection to ensure sufficient temperature stabilization. During the data collection process, the temperature was maintained by circulating nitrogen gas at liquid nitrogen temperature. A silicon-diode probe in contact with the sample was used to obtain an accurate temperature reading. If the temperature reading deviated from the set temperature by more than ±0.5 °C, data collection was aborted automatically.

OHD-OKE spectra were collected using two different scan lengths, each with evenly-spaced data points. To characterize the slower, diffusive orientational motion, scans with a point-spacing of 66.7 fs/step were performed. The total length of the scans was determined by the requirement that the experimentally measured scan must begin and end at zero intensity level to ensure that all of the diffusive relaxa-

tion was captured. To characterize the more rapid inertial and intermolecular dynamics, scans with a point-spacing of 0.667 fs/step were collected. For each sample, at least twenty sets of long-time scans and four sets of short-time scans were obtained and averaged separately into two data files. Between consecutive scans, the computer rotated the first polarizer on the path of the probe beam to switch the heterodyne angle. Laser pulse cross-correlations were measured using a KDP crystal. 10 sets of the cross-correlation scans were averaged into one data file.

4.3 Results and Discussion

4.3.1 Benzene

Logarithmic plots of the collective orientational correlation function ($C_{coll}(t)$, where t is the delay time between pump and probe) of benzene in bulk and in unmodified nanoconfinement are shown in Figure 4.1. From these plots it is clear that the OKE signal decays considerably more slowly in confinement than in the bulk. Previous studies on nanoconfined benzene have shown that a biexponential function in the form of:

$$A_1 \exp\left(-\frac{t}{\tau_1}\right) + A_2 \exp\left(-\frac{t}{\tau_2}\right), \qquad \text{(Eq. 4.1)}$$

can be used to fit $C_{coll}(t)$ from 2 ps on, where A_1 and A_2 are the amplitudes of the exponentials and τ_1 and τ_2 are the collective correlation time constants. In unconstrained fits, it is found that the value of τ_1 varies, whereas the value of τ_2 is nearly identical for benzene in various pore sizes. Therefore, these OKE data were refit with τ_2 constrained to be constant. The results of the τ_2-constrained fits are summarized in Table 4.1.

Table 4.1 Decay times (τ_1 and τ_2) and amplitudes (A_1 and A_2) from biexponential fits of the collective orientational correlation function for nanoconfined benzene. All amplitudes are normalized. The uncertainties are approximately 2% for τ_1, 5% for τ_2, and 5% for A_1 and A_2. R_s is the estimated surface layer thickness of benzene at the confining surfaces. The uncertainty is approximately 10% for R_s.

D (nm)	A_1	τ_1 (ps)	A_2	τ_2 (ps)	R_s (Å)
Bulk	1.00	3.18	---	---	---
6.6	0.86	3.17	0.14	33.3	2.4
6.2	0.85	3.30	0.15	33.3	2.5
4.5	0.81	3.45	0.19	33.3	3.0
3.3	0.68	3.77	0.32	33.3	2.9
2.6	0.67	3.93	0.33	33.3	2.4

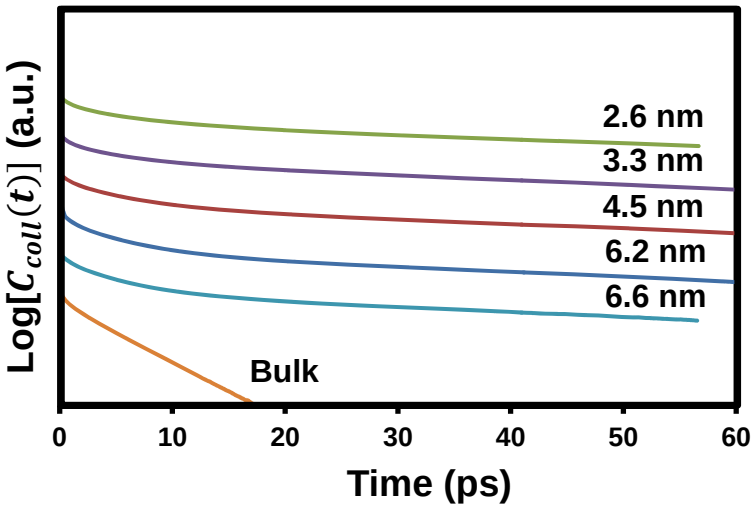

Figure 4.1 Logarithmic plots of the collective orientational correlation function of confined benzene at room temperature. The plots are offset for clarity.

Zhu *et al*[44] suggested that τ_1 arises from orientational relaxation of molecules in the pore centers of the sol-gel glass and varies linearly with pore curvature,

whereas τ_2 arises from the orientational relaxation of benzene in the vicinity of confining surfaces and is independent of pore size. The fact that τ_2 is an order of magnitude greater than τ_1 indicates that there is a strong interaction between benzene molecules and the pore surface. Because the pores of the sol-gel glass are known to be roughly cylindrical and the amplitudes of these two exponentials reflect the relative populations of molecules residing in the pore centers and at the pore surfaces, the thickness of the surface layer of molecules that has inhibited orientational dynamics can be estimated by using the relative populations in conjunction with the average pore radius with the equation:

$$R_s = \frac{D}{2}(1 - \sqrt{A_1}), \qquad \text{(Eq. 4.2)}$$

where A_1 is the relative amplitude of the exponential corresponding to τ_1, and D is the pore diameter. Note that, independent of the true morphology of the confining surfaces, the surface-to-volume ratio must be at least as large as that of a cylinder. Thus, estimates of the surface-layer thickness derived in this way should be viewed as the maximum possible values. The R_s values calculated from Eq. 4.2 are also shown in Table 4.1. The average value of R_s is 2.6 Å, which is significantly smaller than the size of a benzene ring. This result indicates that benzene molecules tend to be parallel to the confining surfaces. This picture is corroborated by the results reported by Nakasaka *et al.*[77], Yi and Jonas,[78] and Xia *et al.*[29] This configuration of benzene molecules at the surfaces might arise from the strong interactions between molecules and the surface. Simulations and scattering data have suggested that benzene is a relatively highly ordered liquid and that molecules tends to form local T-shape structures.[79,80] Therefore, because benzene molecules prefer to lie flat

on the surfaces, the T-shaped structure in liquids can be altered and the density of liquid can be changed significantly.

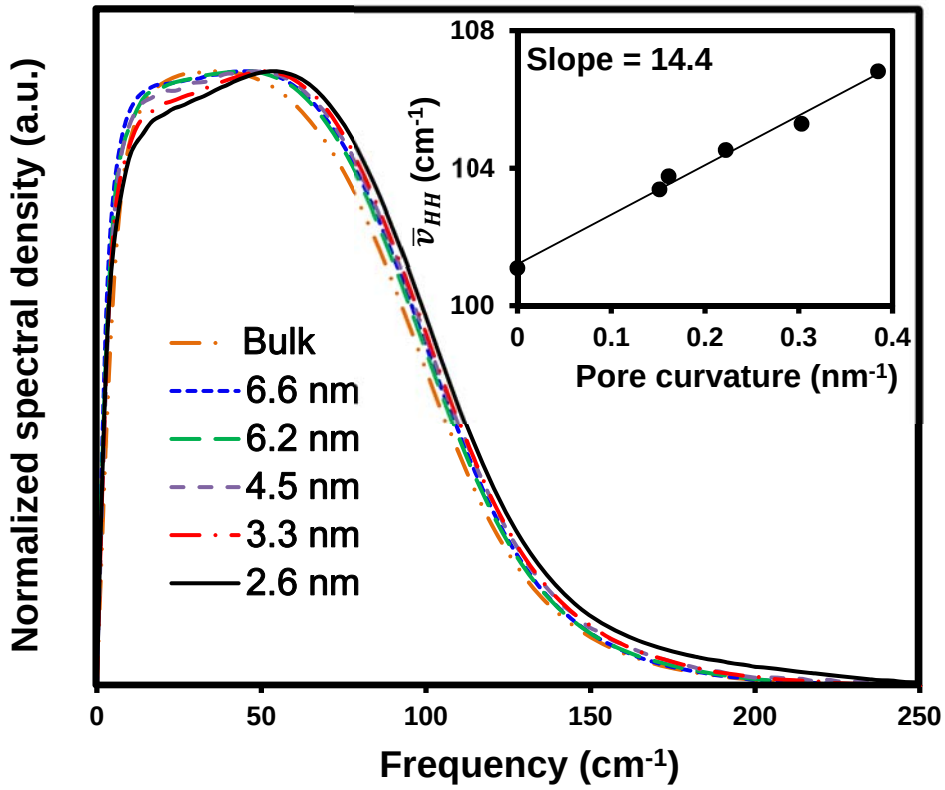

Figure 4.2 Height-normalized RSDs for bulk benzene and benzene in nanopores with diameters of 6.6, 6.2, 4.5, 3.3, and 2.6 nm. The inset is $\bar{\nu}_{HH}$, which is the frequency at which each RSD reaches half of its full height on the falling edge, plotted as a function of the pore curvature (1/diameter). There is a linear dependence of $\bar{\nu}_{HH}$ on the pore curvature that extrapolates to the bulk liquid (zero curvature). The line in the inset plot is a linear least-squares fit to the data.

The RSDs of the bulk and the confined benzene are shown in Figure 4.2. The high-frequency side of these spectra undergoes a clear blue shift with decreasing

pore diameter. To quantify the change of the high-frequency portion of the RSDs of confined benzene, in the inset is plotted the frequency at which each RSD reaches half of its full height ($\bar{\nu}_{HH}$) on the falling edge as a function of pore curvature (the inverse of the pore diameter). A linear dependence of $\bar{\nu}_{HH}$ on the pore curvature with a slope of 14.4 cm^{-1}/nm^{-1} is observed. In previous studies on bulk benzene using OHD-OKE spectroscopy, it was proposed that a similar behavior of the high-frequency part of the RSD is induced by stiffening of the intermolecular potential as the density of the liquid increases with lowering temperature.[62] Based on this result, this blue shift of the high-frequency part of the RSD is proposed to also arise from the change of the density of the liquid in confinement.

To verify our proposed mechanism, the RSDs of bulk benzene were collected at different temperatures. A similar shift of the high-frequency part as the change of the temperature was observed. The RSDs of benzene at temperatures ranging from 269 K to 295 K at an interval of 1 K are presented in Figure 4.3. In this figure, it is evident that the high-frequency side of the RSD shifts to higher frequency and the low-frequency side shifts to lower frequency as the temperature decreases. The shift of the high-frequency part of the RSD is induced by a change of the density of the liquid as temperature increases.[62] The shift of the low-frequency side of the RSD is more difficult to explain and has been related to a reduction in motional narrowing as the time scale of liquid dynamics becomes longer.[64]

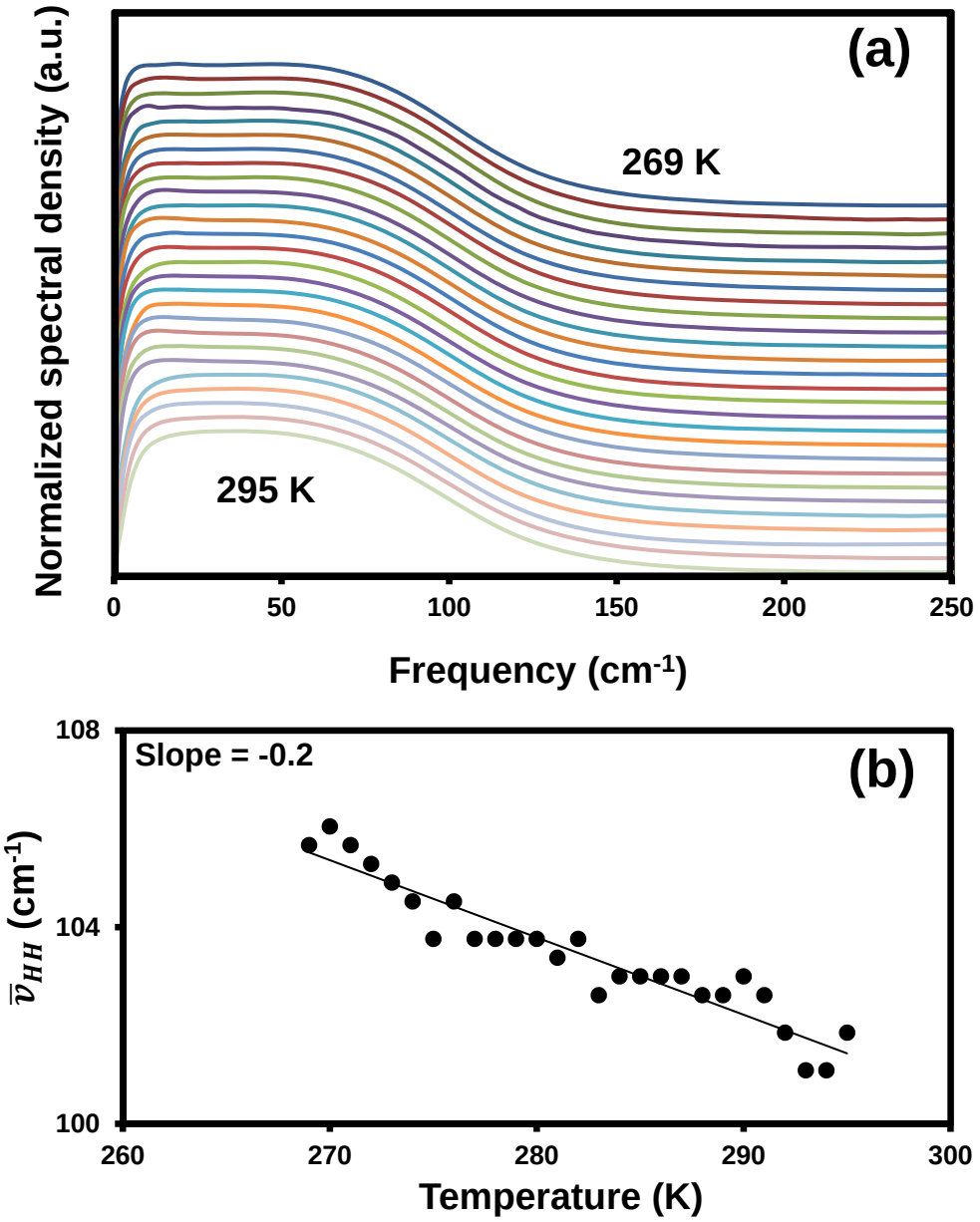

Figure 4.3 (a) Height-normalized RSDs for benzene at temperatures ranging from 269 K to 295 K in 1 K increments. (b) $\bar{\nu}_{HH}$ for the falling edge of the RSDs of bulk benzene liquid plotted as a function of the temperature. The RSDs have been offset for clarity. There is a linear trend in the dependence of $\bar{\nu}_{HH}$ on the temperature. The line is a linear least-squares fit to the data.

Because the RSDs of bulk benzene were collected at temperatures with broad range (269 K to 295 K) and small interval (1 K), it is possible to find an RSD of bulk benzene with density profile that is similar to that of the benzene confined in each pore size. Therefore, the RSDs of nanoconfined benzene were compared to the RSDs of benzene at different temperatures in the frequency region of 50 cm^{-1} to 150 cm^{-1}. By calculating the root-mean-square error (RMSE), I can find a good overlap (the RMSE $\leq$ 0.65%) between these two sets of RSDs. The overlap between RSDs are shown in Figure 4.4. This overlap between these two sets of RSDs suggests that density plays a key role in the shift of the high-frequency part of the RSDs of nanoconfined liquid.

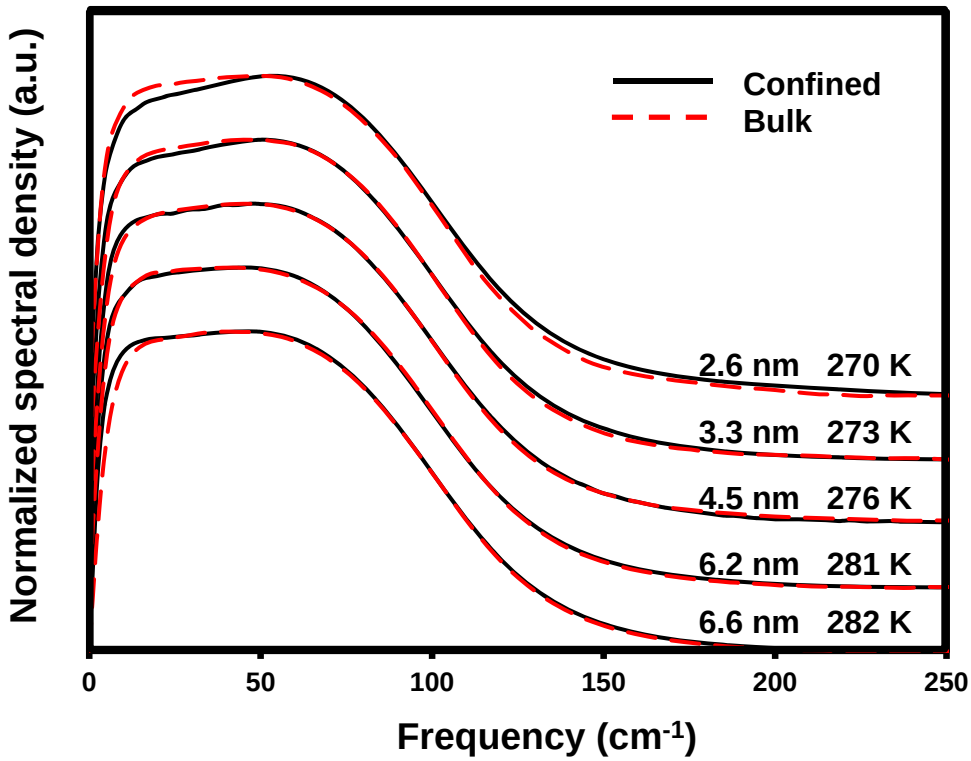

Figure 4.4 The best matches between RSDs of bulk benzene (red, dashed) and confined benzene (black, line). The RSDs have been offset for clarity.

Simulations performed by Coasne *et al.*[81] provided a plausible explanation that this phenomenon is a result of the Coulombic interaction between the π-electron cloud of the benzene aromatic ring and the partial charges carried by the silanol groups on the surface, which can induce the ordering of the adsorbed benzene molecules. This "benzophilic" nature of the silica surface could induce s.ignificant orientational ordering in the adsorbed benzene layer, resulting in densification of the confined benzene. As the density increases, benzene molecules move into a deeper potential well defined by their nearest neighbors and hence, the frequency of the librational motions shifts to higher frequency. If the surface organization of benzene contributes to its densification in confinement, this effect would be expected to be reduced (or even reversed) if the surfaces of the pores are rendered more "benzophobic." To test this idea, the pore surfaces of sol-gel glasses were functionalized with trimethylsilyl groups and benzene OKE RSDs were again obtained. As shown in Figure 4.5 and its inset, the high-frequency edge of the RSD in this case is invariant to the pore curvature (note that the pore curvature given is the pre-functionalization value). This result is consistent with the idea that the change of the density within the pores induces the shift of the high-frequency part of the RSD.

Simulations[81] suggest that the local density of benzene in the pore center and in the vicinity of the surfaces are independent of pore size. In Table 4.1, it is clear that the value of A_2 increases as the pore curvature increases, suggesting an increase of the population of molecules near the surface. Therefore, the density of benzene in a tighter confinement should be higher than that in larger pores, and the

librational frequencies should therefore be shifted most for benzene confined in smallest pores.

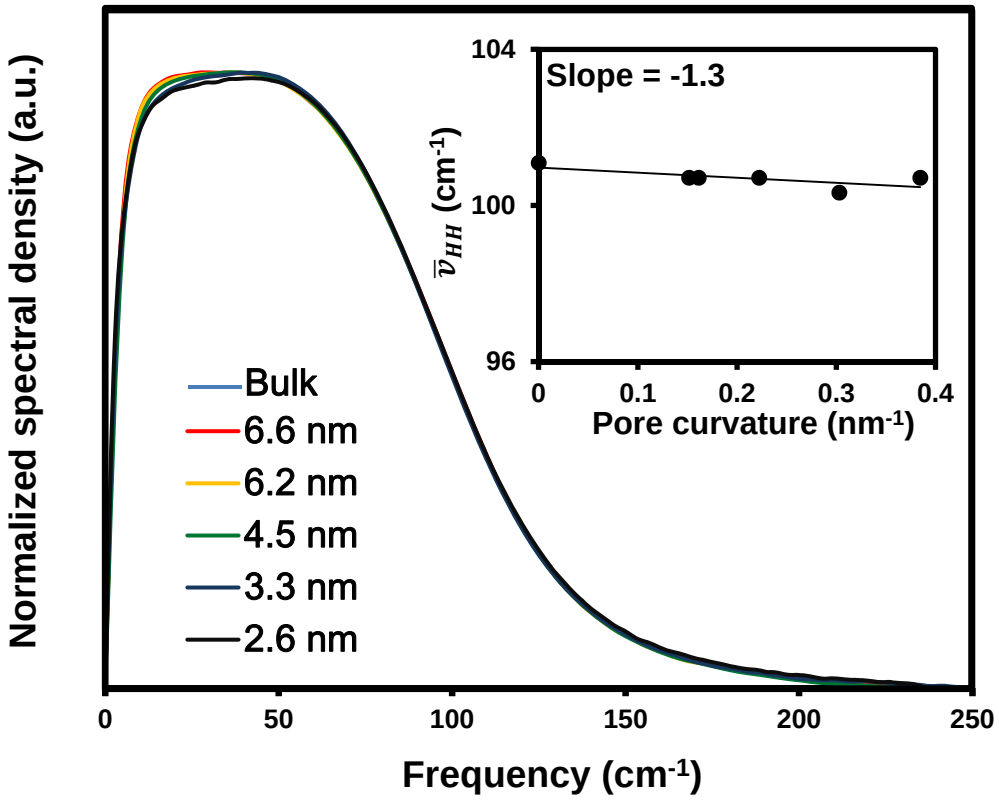

Figure 4.5 Height-normalized RSDs for benzene confined in surface-modified sol-gel glasses. The inset is $\bar{\nu}_{HH}$ plotted as a function of pore curvature (1/diameter). There is a linear dependence of $\bar{\nu}_{HH}$ on the pore curvature that extrapolates to the bulk liquid (zero curvature). The line in the inset plot is a linear least-squares fit to the data.

An alternative way of measuring the shift in the RSD is to fit the RSD to a sum of a BL function and an AG function. As shown in Figure 4.6, the RSD of the confined benzene can be fit well with the sum of these two functions. The parameters from these fits are listed in Table 4.2, Table 4.3, and Table 4.4 for the RSDs of

benzene confined in unmodified pores, in modified pores, and in the bulk, respectively.

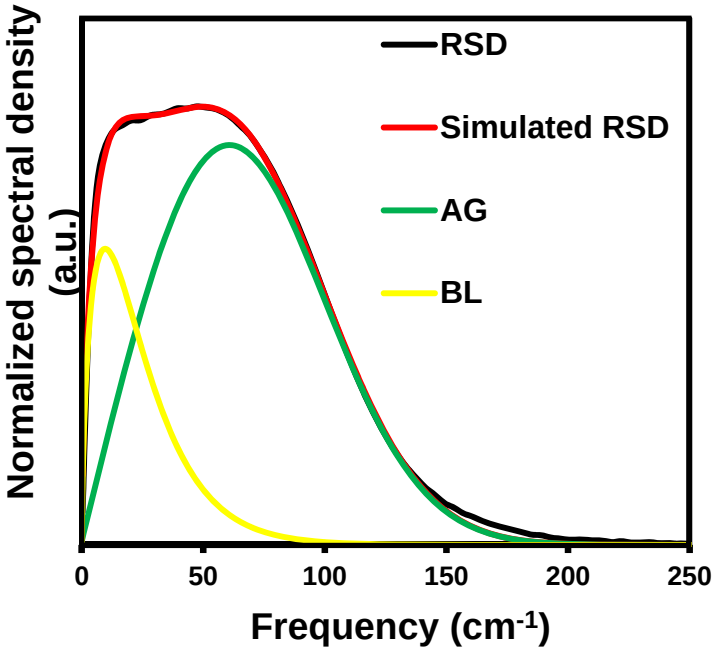

Figure 4.6 A representative fit to an RSD of confined benzene (in pores of 6.6 nm diameter) with the sum of a BL function and an AG function.

Table 4.2 Parameters from fits of RSDs of benzene in unmodified pores to a sum of a BL function and an AG function (numbers in parentheses are uncertainties in last digits solely arising from the fits; additional uncertainties inherent in the data are less than 10%).

D (nm)	ω_0 (cm^{-1})	ω_1(cm^{-1})	σ	δ	A_{AG}/A_{BL}
2.6	10.4(3)	49.8(1)	46.8(5)	0.81(3)	4.5(2)
3.3	10.6(3)	52.5(9)	44.1(4)	0.82(2)	4.2(2)
4.5	10.2(2)	50.7(9)	44.8(4)	0.88(2)	4.6(1)
6.2	11.7(2)	53.8(5)	42.8(5)	0.71(1)	3.5(1)
6.6	10.8(2)	52.2(7)	43.5(3)	0.86(2)	4.5(1)
Bulk	11.7(2)	51.2(6)	43.3(3)	0.81(1)	4.2(1)

Table 4.3 Parameters from fits of RSDs of benzene in modified pores to a sum of a BL function and an AG function (numbers in parentheses are uncertainties in last digits solely arising from the fits; additional uncertainties inherent in the data are less than 10%).

D (nm)	ω_0 (cm^{-1})	ω_1(cm^{-1})	σ	δ	A_{AG}/A_{BL}
2.6	10.8(2)	32(4)	50.0(9)	0.76(1)	5.0(6)
3.3	10.4(3)	30(5)	50.0(9)	0.81(1)	6.0(9)
4.5	10.0(2)	38(2)	48.1(5)	0.91(1)	5.9(3)
6.2	10.3(2)	37(2)	47.8(5)	0.81(1)	5.0(2)
6.6	10.3(2)	38(2)	48.1(7)	0.86(1)	4.9(3)
Bulk	11.7(2)	51.2(6)	43.3(3)	0.81(1)	4.2(1)

The AG function, which is intended to describe the contribution of librational motion,[14] dominates the high-frequency part of the RSD. If the high-frequency part of the RSD shifts due to the change of the librational frequency distribution, the first moment of the AG function (ω_1) would be expected to increase as the density increases. In Figure 4.7, ω_1 is plotted as a function of temperature for bulk benzene, this parameter increases linearly as temperature decreases, because density decreases with temperature. Similarly, in Figure 4.8, ω_1 is plotted as a function of the pore curvature for benzene in unmodified pores. The value of the first moment increases linearly as pore curvature increases, because density increases with pore curvature due to the benzophilic nature of the confining surfaces. Because the modification of the surface can change the "benzophilic" surface into a "benzophobic" one, the librational frequencies of benzene molecules are expected to be affected less by the methylated surfaces. As a result, the relationship between the first moment of the AG function and the pore curvature of benzene in modified pores is

different from that observed in unmodified pores. In Figure 4.8, ω_1 in the fits of RSDs of nanoconfined benzene in modified pores is plotted as a function of the pore curvature and compared to that of the benzene in unmodified pores. The slopes of these two plots are drastically different and are of opposite sign, suggesting that the modification has a significant impact on the librational motion of nanoconfined benzene molecules.

Table 4.4 Parameters from fits of RSDs of bulk benzene to a sum of a BL function and an AG function (numbers in parentheses are uncertainties in last digits solely arising from the fits; additional uncertainties inherent in the data are less than 5%).

T (K)	ω_0 (cm^{-1})	ω_1(cm^{-1})	σ	δ	A_{AG}/A_{BL}
269	11.9(4)	58.1(7)	41.5(4)	0.74(2)	3.5(2)
270	12.5(5)	58.1(9)	41.8(5)	0.64(2)	2.7(1)
271	13.6(5)	61.1(6)	39.3(3)	0.66(2)	3.0(2)
272	12.8(4)	59.5(7)	40.4(4)	0.68(2)	3.0(2)
273	12.3(4)	58.6(7)	40.7(4)	0.73(2)	3.4(2)
274	11.2(3)	53.4(9)	43.8(5)	0.74(2)	3.4(2)
275	11.8(2)	56.0(5)	41.4(3)	0.72(1)	3.2(2)
276	11.5(2)	53.3(6)	43.8(3)	0.68(1)	3.0(2)
277	11.5(3)	52.3(9)	44.1(4)	0.69(1)	3.0(1)
278	11.0(2)	52.8(7)	43.7(3)	0.80(1)	3.8(1)
279	11.4(3)	55.3(6)	42.2(3)	0.81(1)	4.0(1)
280	11.6(2)	55.5(4)	42.2(2)	0.77(1)	3.5(1)
281	11.9(2)	55.8(5)	41.8(3)	0.74(1)	3.3(1)
282	12.5(2)	56.9(4)	41.4(2)	0.70(1)	3.1(1)
283	11.6(2)	53.2(6)	43.0(3)	0.78(1)	3.8(1)
284	11.5(2)	54.7(5)	42.3(2)	0.84(1)	4.3(1)
285	11.3(2)	53.8(5)	42.8(2)	0.77(1)	3.5(1)
286	10.9(2)	52.2(6)	43.5(3)	0.83(1)	3.9(1)
287	10.6(2)	50.5(7)	44.7(3)	0.84(1)	4.0(1)
288	10.9(2)	53.5(5)	42.6(2)	0.85(1)	4.2(1)
289	11.1(2)	51.4(7)	43.6(3)	0.89(2)	4.8(2)
290	10.8(2)	47(1)	46.0(4)	0.85(1)	4.4(2)
291	10.6(2)	44(2)	47.3(6)	0.88(2)	4.9(3)
292	10.3(2)	42(2)	47.4(7)	0.86(2)	4.5(3)
293	11.7(2)	54.4(4)	41.2(2)	0.85(1)	4.2(1)
294	10.2(2)	32(5)	50(1)	0.88(2)	6(1)
295	11.7(2)	51.2(6)	43.3(3)	0.81(1)	4.2(1)

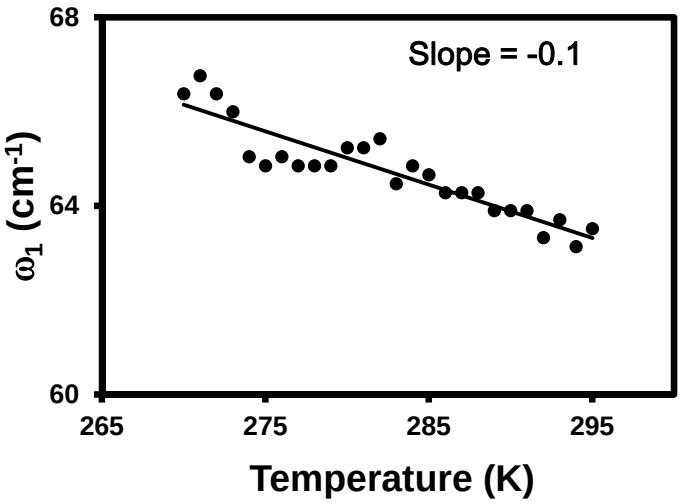

Figure 4.7 First moments of the AG portion of fits to RSDs of the bulk benzene are plotted as a function of the temperature. The line is a linear least-squares fit to the data.

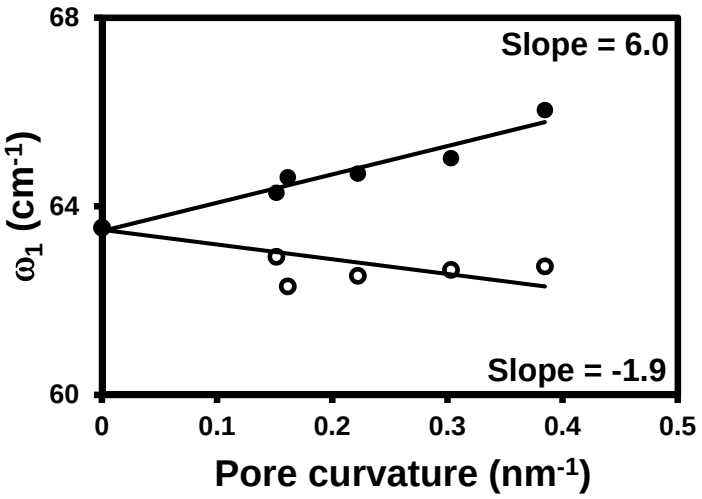

Figure 4.8 First moments of the AG portion of fits to RSDs of benzene confined in unmodified pores (solid symbols) and modified pore (open symbols) are plotted as a function of the pore curvature. The lines are linear least-squares fits to the data.

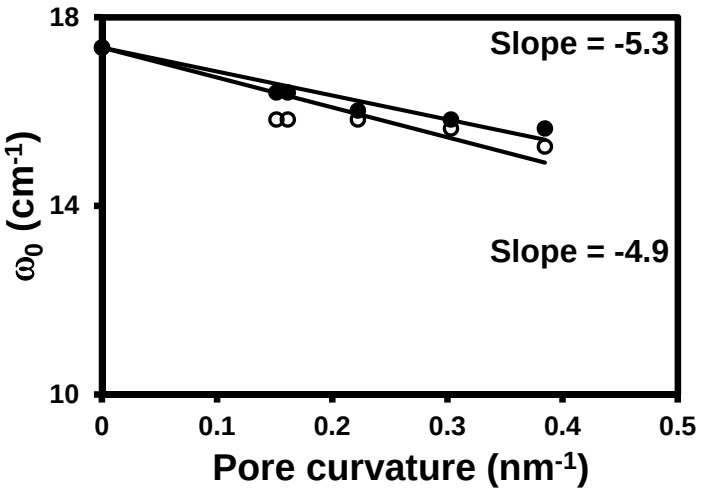

Figure 4.9 First moments of the BL portion in the RSDs of confined benzene in unmodified pores (solid symbols) and modified pores (open symbols) are plotted as a function of the pore curvature. The lines are linear least-squares fits to the data.

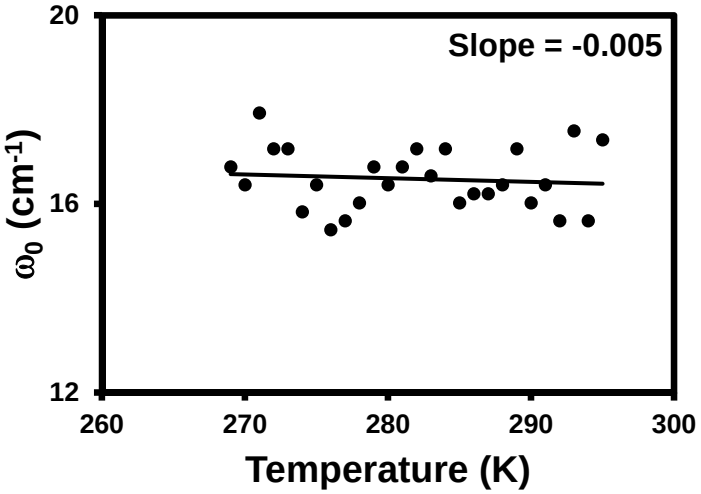

Figure 4.10 First moments of the BL portion of fits to RSDs of the bulk benzene are plotted as a function of the temperature. The solid line is a linear least-squares fits to the data.

4.3.2 Pyridine

To explore the effects of density on the dynamics of confined liquids further, we moved to pyridine, a molecule with nearly identical shape and size but significantly different intermolecular potential from benzene.[82] Pyridine has a sizable dipole moment of 2.15 Debye, whereas benzene is a non-polar molecule. Therefore, the intermolecular structures of pyridine differ from those in benzene. In addition, when pyridine is confined in sol-gel glasses, the nitrogen in the pyridine ring can accept a hydrogen bond from a silanol group on the confining surface,[83] which could make pyridine molecules take on different configurations at the confining surface than does benzene.

The logarithmic plots of the collective orientational correlation function for bulk pyridine and nanoconfined pyridine are shown in Figure 4.11. Eq. 4.1 was used to fit the data from 3 ps. Similar to benzene, the faster time constant (τ_1) of pyridine grows as the pore size decreases whereas the slower time constant (τ_2) remains the same in all pore sizes. Therefore, τ_2 was constrained to be a constant in all pore sizes, and then the data were refit with a biexponential function. Results of these fits are summarized in Table 4.5. Because τ_1 is similar to the orientational relaxation time of bulk pyridine, this time constant is assumed to arise from the relaxation of pyridine at the center of the pore. τ_2 is about an order of magnitude greater than τ_1, and is proposed to arise from the hindered reorientation of molecules at the confining surfaces.[30]

Table 4.5 Decay times (τ) and amplitudes (A) from biexponential fits of the collective orientational correlation functions for confined pyridine. All amplitudes are normalized. The uncertainties are approximately 2% for τ_1, 5% for τ_2, and 5% for A. R_s is the estimated surface-layer thickness of dynamically inhibited pyridine at the confining surface. The uncertainty is approximately 10% for R_s.

D (nm)	A_1	τ_1 (ps)	A_2	τ_2 (ps)	R_s (Å)
Bulk	1	4.01	---	---	---
7.3	0.82	4.27	0.18	21.8	3.5
5.9	0.80	4.60	0.20	21.8	3.1
2.4	0.35	4.79	0.65	21.8	4.9

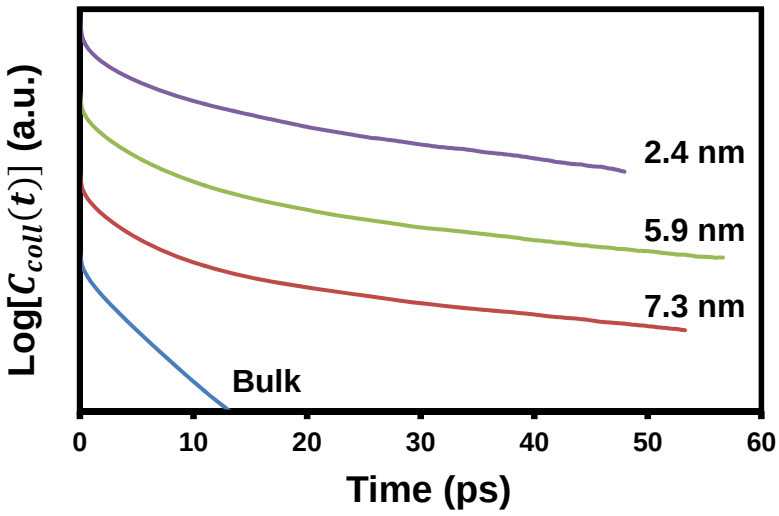

Figure 4.11 Logarithmic plots of the collective orientational correlation functions for nanoconfined pyridine. The data are offset for clarity.

The average thickness of the dynamically inhibited surface layer of molecules of nanoconfined pyridine is 3.8 Å. This value is greater than that observed for benzene. This result indicates that pyridine molecules are more likely to stand

on the surface, with their nitrogen atom interacting strongly with the surface hydroxyl groups through H-bonding. The collective orientational correlation time of interfacial pyridine (~22 ps) is smaller than that of benzene (~33 ps), which is also consistent with our proposed picture of the interfacial structure.

The RSDs of pyridine confined in sol-gel glasses with pore diameters of 7.3, 5.9, and 2.4 nm at room temperature are shown in Figure 4.12. The RSDs of benzene and pyridine bear a strong resemblance to one another because the molecular shape plays an important role in determining the form of RSDs.[58] The results from NMR studies on the dynamics of confined pyridine have shown that the pyridine tends to have a ordered surface structure in confinement,[83,84] leading to a change of the liquid density. Therefore, in analogy to benzene, this shift of the high-frequency feature in the RSDs of pyridine can also be ascribed to a change in liquid density as it is confined in pores. The inset of Figure 4.12 shows that there is a linear dependence of $\bar{\nu}_{HH}$ on the pore curvature, with a slope of 18.7 cm^{-1}/nm^{-1}. This slope is greater than that observed for nanoconfined benzene. Because pyridine molecules and the confining surfaces interact mainly through H-bonding and prefer to "stand" on the surfaces, the difference in the slopes presumably reflects the difference in the configurations of molecules near the surfaces for these two liquids.

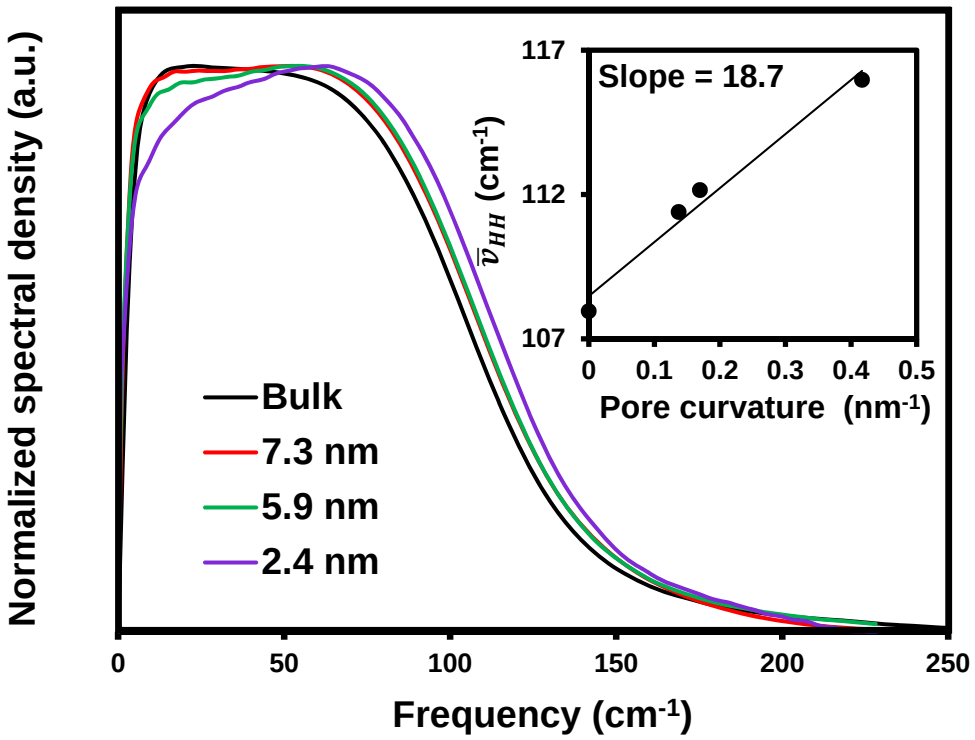

Figure 4.12 Height-normalized RSDs for the bulk pyridine and pyridine confined in sol-gel glasses of pore diameters at 7.3, 5.9, and 2.4 nm. The inset is $\bar{\nu}_{HH}$ on the falling edge of the RSD plotted as a function of the pore curvature. There is a linear dependence of $\bar{\nu}_{HH}$ on the pore curvature that extrapolates to the bulk liquid (zero curvature). The line in the inset plot is a linear least-squares fit to the data.

RSDs of bulk pyridine at temperatures ranging from 263 K to 290 K are shown in Figure 4.13(a). The high-frequency edge of the RSD shifts to higher frequency as temperature is decreased. As in the case of benzene, the blue shift of the high-frequency edge of the RSD may reflect an increase in the density with decreasing temperature. In Figure 4.13(b), $\bar{\nu}_{HH}$ of RSDs for bulk pyridine is plotted as a function of temperature. There is a linear dependence of $\bar{\nu}_{HH}$ on temperature. The slope of the linear fit of this plot is similar to that of the plot of bulk benzene.

In the best match of each confined RSD at frequencies between 50 cm^{-1} and 150 cm^{-1} in RSDs of bulk pyridine, which is shown in Figure 4.14, it is evident that the smaller the pore diameter, the lower the temperature of the corresponding RSD of bulk pyridine. Also, the plots of $\bar{\nu}_{HH}$ versus either the temperature or the pore curvature have slopes of the same order of magnitude for benzene and pyridine. Because we believe that the shift of $\bar{\nu}_{HH}$ largely depends on the change of the liquid density, the similarity in the results of pyridine and benzene suggests that the change of the density is also the driving force in the shift of $\bar{\nu}_{HH}$ of nanoconfined pyridine.

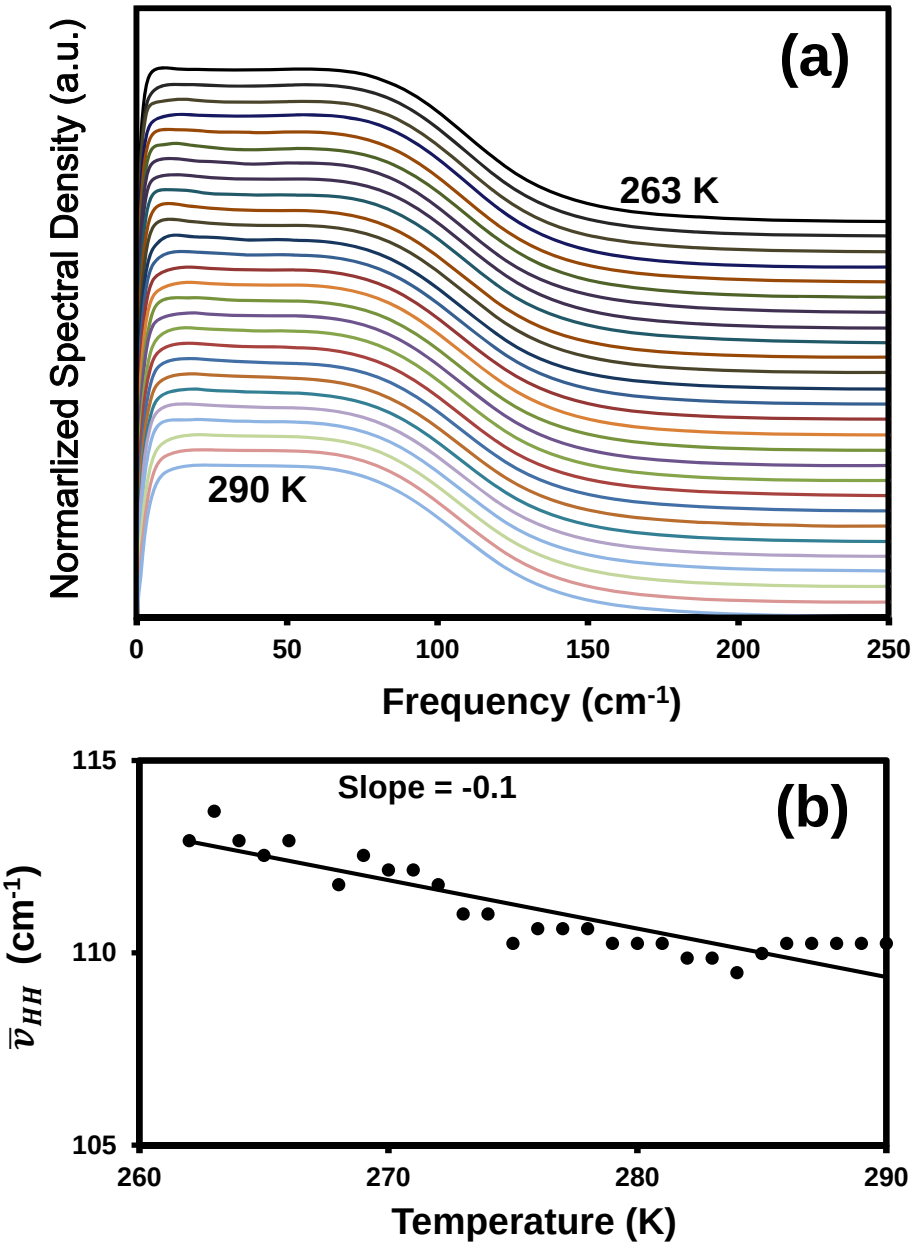

Figure 4.13 (a) Height-normalized RSDs for pyridine at temperatures ranging from 263 K to 290 K. The data have been offset for clarity. (b) $\bar{\nu}_{HH}$ for the falling edge of RSDs is plotted as a function of temperature of bulk pyridine. There is a linear trend in the dependence of $\bar{\nu}_{HH}$ on the temperature. The line is a linear least-squares fit to the data.

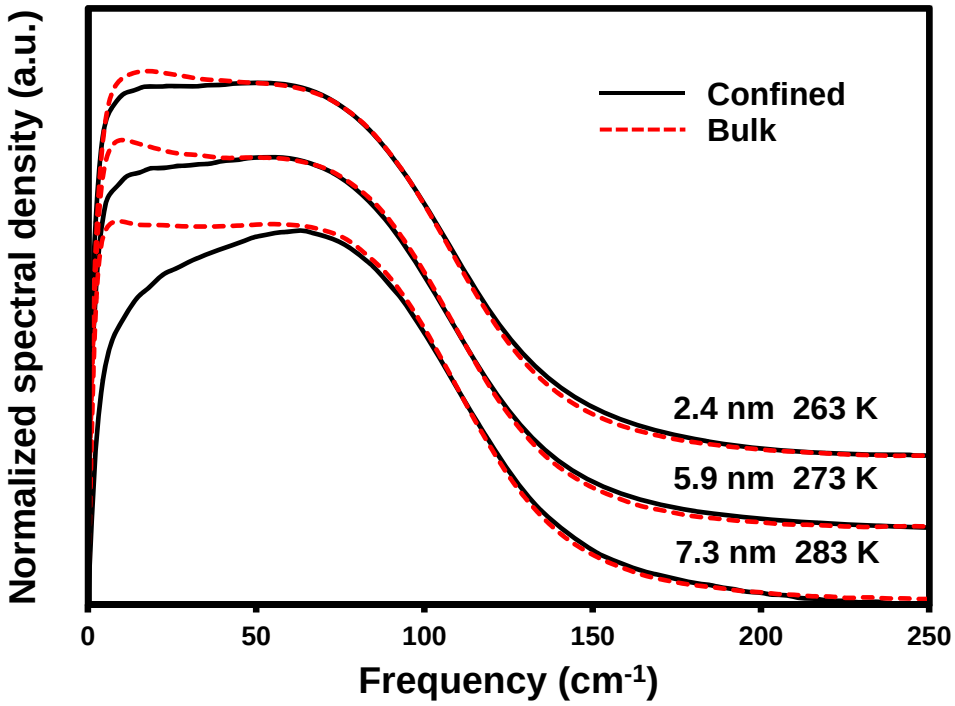

Figure 4.14 Comparisons of the best match between RSDs of bulk pyridine (red) and confined pyridine (black). The data have been offset for clarity.

The results from the fitting of the RSDs of pyridine at different temperatures and in nanoconfinement using the sum of an AG and a BL function are presented in Table 4.6 and Table 4.7. In Figure 4.15 and Figure 4.16, the first moment of the AG function is plotted as a function of temperature and pore curvature, respectively. It is evident from Figure 4.15 that the first moment of the AG function increases linearly as the temperature decreases. The linear fit of the plot of first moment of the AG function as a function of temperature has a slope (-0.1 cm^{-1}/K) that is comparable to that of benzene. In Figure 4.16, the first moment of the AG function is plotted as a function of the pore curvature for confined pyridine. Similar to benzene, the first moment increases with the pore curvature. However, the linear fit of the plot in Figure 4.16 has a slope of 15.4 cm^{-1}/nm^{-1}, which is 2.5 times greater than

that of benzene (6.0 cm^{-1}/nm^{-1}). Because pyridine molecules in the vicinity of the confining surfaces tend to use the nitrogen atom form hydrogen bonds with the silanol groups, the differences in the slopes of the plots presumably reflect differences in the strength of the interaction between the liquid molecules and the surface silanol groups. Figure 4.2 and Figure 4.12 indicate that the slope of the $\bar{\nu}_{HH}$ plot of confined pyridine is greater than that of confined benzene, which is in agreement with the first moment of the AG function. Therefore, the change in the $\bar{\nu}_{HH}$ may be treated as an indication of the change of the density for benzene and pyridine.

A couple of natural extensions of the current work can be planned as follows: (1) Confining pyridine in surface-modified sol-gel glasses to assess the role of the hydrogen bonding. By functionalizing the pores with trimethylsilyl groups, the hydrophilic surfaces are turned into hydrophobic ones. The plots of $\bar{\nu}_{HH}$ as a function of the pore curvature of pyridine in unmodified pores and modified pores should be compared. (2) MD simulations of bulk pyridine at atmospheric pressure, constant temperature, and constant density could be performed for further evaluation of the relative importance of the temperature and the density in the spectroscopic shift of RSDs of bulk pyridine. (3) Pyridine molecules can be fluorinated to weaken the interaction between pyridine molecules and the surface hydroxyl groups. Because perfluoropyridine is not a good H-bond acceptor, it is expected that the confined perfluoropyridine would behave similarly to bulk perfluoropyridine.

Table 4.6 Parameters from fits of RSDs of bulk pyridine to a sum of a BL function and an AG function (numbers in parentheses are uncertainties in last digits solely arising from the fits; additional uncertainties inherent in the data are less than 5%).

T (K)	ω_0 (cm^{-1})	ω_1(cm^{-1})	σ	δ	A_{AG}/A_{BL}
262	16.2(6)	68.6(7)	39.3(4)	0.49(2)	1.8(1)
263	16.5(7)	68.0(7)	40.1(4)	0.46(2)	1.8(1)
264	17.0(8)	68.5(7)	39.6(4)	0.46(2)	1.8(1)
265	18.0(8)	68.8(7)	39.1(4)	0.42(2)	1.6(1)
266	17.5(7)	69.0(7)	39.1(4)	0.47(1)	1.8(1)
268	15.3(6)	66.2(7)	40.5(4)	0.51(2)	1.9(1)
269	14.9(5)	66.5(7)	40.8(4)	0.52(2)	1.9(1)
270	14.8(8)	66(1)	41.3(6)	0.50(2)	1.8(1)
271	15.6(8)	66.7(9)	40.6(5)	0.49(2)	1.8(1)
272	14.0(6)	65(1)	41.7(5)	0.55(2)	2.0(1)
273	14.0(6)	64.9(9)	41.1(5)	0.58(2)	2.0(1)
274	14.0(6)	64.9(9)	41.0(5)	0.58(2)	2.1(1)
275	15.4(7)	66.2(8)	39.7(4)	0.57(2)	2.1(1)
276	15.4(7)	66.1(8)	39.9(5)	0.57(2)	2.2(1)
277	15.3(7)	66.0(8)	40.0(4)	0.57(2)	2.2(1)
278	15.6(7)	66.5(8)	39.7(4)	0.58(2)	2.2(1)
279	14.0(5)	65.3(8)	40.3(4)	0.65(2)	2.5(1)
280	15.4(6)	66.3(8)	39.6(4)	0.58(2)	2.2(1)
281	14.5(5)	65.4(7)	40.2(5)	0.64(2)	2.5(1)
282	14.2(6)	64.4(9)	40.9(5)	0.64(2)	2.5(1)
283	13.8(6)	64.4(9)	41.1(3)	0.67(2)	2.6(1)
284	14.2(4)	64.3(6)	41.0(3)	0.65(2)	2.6(1)
285	13.9(4)	64.1(6)	41.1(4)	0.67(2)	2.7(1)
286	13.7(4)	63.7(6)	41.5(4)	0.64(2)	2.5(1)
287	13.1(4)	62.6(7)	42.0(3)	0.67(2)	2.6(1)
288	13.8(4)	64.0(6)	41.3(3)	0.69(2)	2.9(1)
289	13.6(4)	64.3(5)	40.6(4)	0.73(2)	3.2(1)
290	12.8(4)	62.2(7)	42(1)	0.76(2)	3.4(1)

Table 4.7 Parameters from fits of RSDs of pyridine in unmodified pores to a sum of a BL function and an AG function (numbers in parentheses are uncertainties in last digits solely arising from the fits; additional uncertainties inherent in the data are less than 10%).

D (nm)	ω_0 (cm^{-1})	ω_1(cm^{-1})	σ	δ	A_{AG}/A_{BL}
2.6	20.0(7)	68.8(5)	42.3(3)	0.41(1)	2.1(1)
5.9	15.2(4)	62.3(6)	43.6(3)	0.50(1)	2.1(1)
7.3	14.2(3)	61.4(6)	43.9(3)	0.55(1)	2.3(1)
Bulk	11.7(5)	57(1)	44.6(7)	0.79(3)	3.5(2)

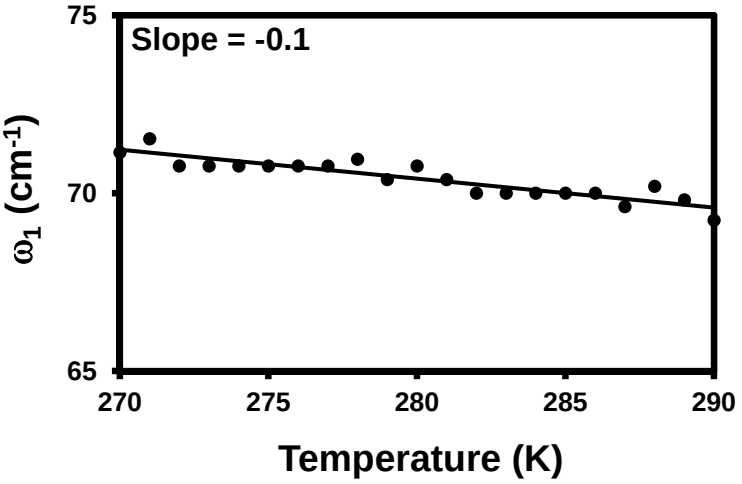

Figure 4.15 First moments of the AG portion of fits to the RSDs of the bulk pyridine plotted as a function of the temperature. The line is a linear least-squares fit to the data.

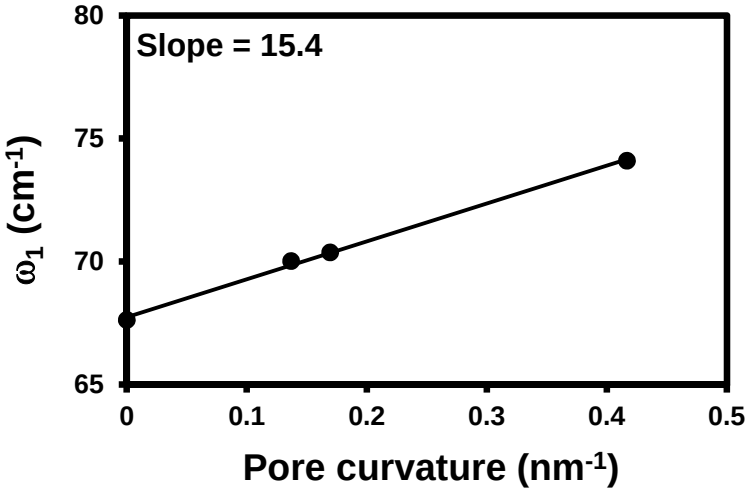

Figure 4.16 First moments of the AG portion of fits to RSDs of pyridine confined in unmodified pores plotted as a function of the pore curvature. The line is a linear least-squares fit to the data.

4.3.3 Acetonitrile

Given that benzene and pyridine both have a disk-like molecular shape, it is interesting to compare their dynamics in nanoconfinement to those of other strongly wetting liquids with a rod-like shape. To serve this purpose, this section focuses on one prototypical, strongly-wetting, linear molecule: acetonitrile. Acetonitrile has a sizeable dipole moment of 3.92 Debye and can accept hydrogen bonds from silanol groups on the confining surfaces.[51] Due to the significant dipole moment of this molecule, it has a strong tendency to form antiparallel dimers in the bulk liquid.[85] Different behavior mighty therefore be expected in confinement.

OHD-OKE transients of acetonitrile confined within sol-gel glasses of pore diameters of 6.6, 5.6, 3.3, and 2.8 nm have been measured at room temperature.

Logarithmic plots of the collective orientational correlation function of nanoconfined acetonitrile are shown in Figure 4.17. All of these decays can be fit by a sum of three exponential functions:

$$C_{coll}(t) = A_1 \exp\left(-\frac{t}{\tau_1}\right) + A_2 \exp\left(-\frac{t}{\tau_2}\right) + A_3 \exp(-\frac{t}{\tau_3}), \quad \text{(Eq. 4.3)}$$

where A_n is for the amplitude of exponential n and τ_1, τ_2, and τ_3 are the time constants of each exponential. The results of the fits are summarized in Table 4.8. The smallest time constant of these three exponentials (τ_1) is the same as that observed in the bulk liquid. The intermediate time constant, τ_2 is approximately three times greater than τ_1 and is found to be nearly identical in all pore diameters. The third time constant, τ_3, is more than an order of magnitude greater than τ_1, and also is identical over all pore diameters.

Table 4.8 Decay times (τ) and amplitudes (A) from triexponential fits of the collective orientational correlation functions of confined acetonitrile. All temperatures are in Kelvin and all decay times are in ps. The sum of A_1, A_2, and A_3 is one. The uncertainties are approximately 2% for τ_1, 5% for τ_2, 10% for τ_3, and 5% for A_1, A_2, and A_3.

D (nm)	A_1	τ_1 (ps)	A_2	τ_2 (ps)	A_3	τ_3 (ps)
Bulk	1	1.66	--	--	--	--
6.6	0.50	1.61	0.32	5.67	0.18	27.3
5.6	0.35	1.70	0.33	5.67	0.32	27.3
3.3	0.30	1.73	0.32	5.67	0.38	27.3
2.8	0.30	1.64	0.35	5.67	0.35	27.3

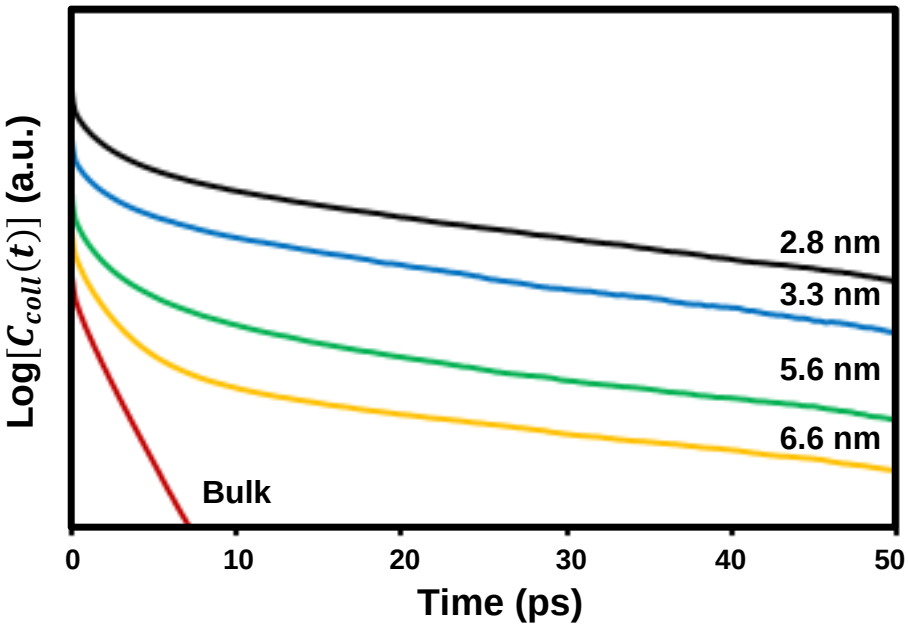

Figure 4.17 Logarithmic plots of the collective orientational correlation functions of acetonitrile in sol-gel glasses at room temperature. The plots are shifted for clarity.

A model has been developed to account for the decay times for orientational dynamics of nanoconfined acetonitrile observed in the OKE data.[51] In nanoconfined acetonitrile, approximately half of the interfacial molecules at the pore surfaces accept hydrogen bonds from surface silanol groups; the other half of the interfacial molecules face in the opposite direction and are interdigitated with the H-bonded molecules. In the pore centers, the dynamics of acetonitrile molecules is not affected by the confining surfaces, and therefore the relaxation of these molecules is similar to that of the bulk liquid.[21,51] The relaxation of the hydrogen-bonded molecules in the vicinity of the confining surfaces accounts for the slowest exponential decay observed. The interdigitated molecules have dynamics that mirror those of the hydrogen-bonded molecules, but the interdigitated molecules can also

migrate into the bulk-like population of the liquid. This phenomenon provides a new channel for relaxation that is believed to account for the intermediate relaxation time. Several simulations on the structure and dynamics of acetonitrile confined in silica nanopores have supported this model.[86,87,88] Cheng *et al*.[86] used their simulation results to describe the structure of acetonitrile liquid confined in a cylindrical silica pore. They suggested that the acetonitrile molecules located in the vicinity of the surface can form a bilayer structure with two antiparallel oriented sublayers, whereas acetonitrile molecules in the closest sublayer are pointing towards the surface with nitrogen atoms. This layering and antiparallel structure can propagate into the acetonitrile for at least 1.75 nm.[86] This result agrees with Ding *et al*.'s work[89] on acetonitrile on the flat silica surface. Due to this layering structure, Cheng *et al*.[86] also suggested that the population-specific dynamic properties are not sensitive to pore curvature.

Figure 4.18 shows RSDs collected at room temperature for bulk and nano-confined acetonitrile. The RSD of acetonitrile has a "triangular" shape, which distinguishes itself from the "rectangular" RSD of benzene and pyridine. The RSDs of confined acetonitrile bear a strong resemblance to that of the bulk acetonitrile. It is clear in Figure 4.18 that the high-frequency edge of the spectra undergoes a blue shift with increasing pore curvature. In the inset, $\bar{\nu}_{HH}$ is plotted as a function of the pore curvature. The plot of $\bar{\nu}_{HH}$ over pore curvature can be fit linearly with a slope of 18.3 cm^{-1}/nm^{-1}, which is similar to that of benzene.

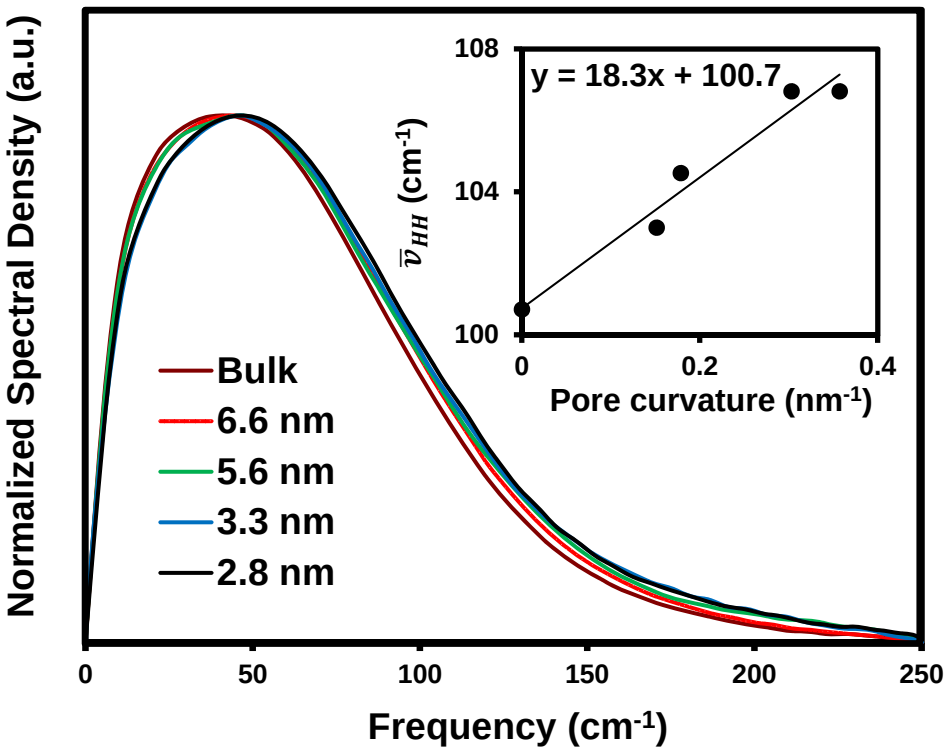

Figure 4.18 Height-normalized RSDs for bulk acetonitrile and acetonitrile confined in sol-gel glasses at room temperature. The inset is $\bar{\nu}_{HH}$ as a function of pore curvature. There is a linear trend in the dependence of $\bar{\nu}_{HH}$ on the pore curvature extrapolating to zero curvature (the bulk liquid). The line in the inset plot is a linear least-squares fit to the data.

The RSDs of bulk acetonitrile at temperatures ranging from 295 K to 225 K are shown in Figure 4.19. It is evident that the high-frequency feature of the RSD moves to higher frequencies with decreasing temperature. Similar to benzene and pyridine, RSDs of bulk acetonitrile can be found at lower temperature to match to each nanoconfined RSD at frequencies between 50 cm^{-1} and 150 cm^{-1}. The best overlapped RSDs are shown in Figure 4.20. The RSD of nanoconfined acetonitrile can be overlapped with the RSD of bulk acetonitrile at temperatures lower than the

room temperature. Despite the possibility that the AG function might not be the adequate descriptor of the triangular RSDs,[62] similar fitting is performed for ease of comparison to those of benzene. The fitting results of the RSDs of nanoconfined and bulk acetonitrile to a sum of AG and BL function are shown in Table 4.9 and Table 4.10. The first moment of the AG function is plotted over temperature and pore curvature in Figure 4.21 and Figure 4.22, respectively. In Figure 4.21, the first moment of AG function decreases linearly as the temperature increases, which is similar to what was observed in benzene and pyridine. In both acetonitrile and benzene, this linear relationship can be explained by the fact that the density decreases as temperature increases, and thus the libration shifts to lower frequencies. Previously, I have shown that $\bar{\nu}_{HH}$ shifts linearly as a function of the pore curvature. As shown in Figure 4.22, a plot of the first moment of AG portion as a function of pore curvature for acetonitrile, the linear fit of the data has a slope of -0.1 cm^{-1}/nm^{-1}, whereas that of benzene is more than an order of magnitude greater. This difference in the slopes indicates that compared to nanoconfined benzene, the change of the librational frequency as a function of the pore curvature is much less dramatic in nanoconfined acetonitrile.

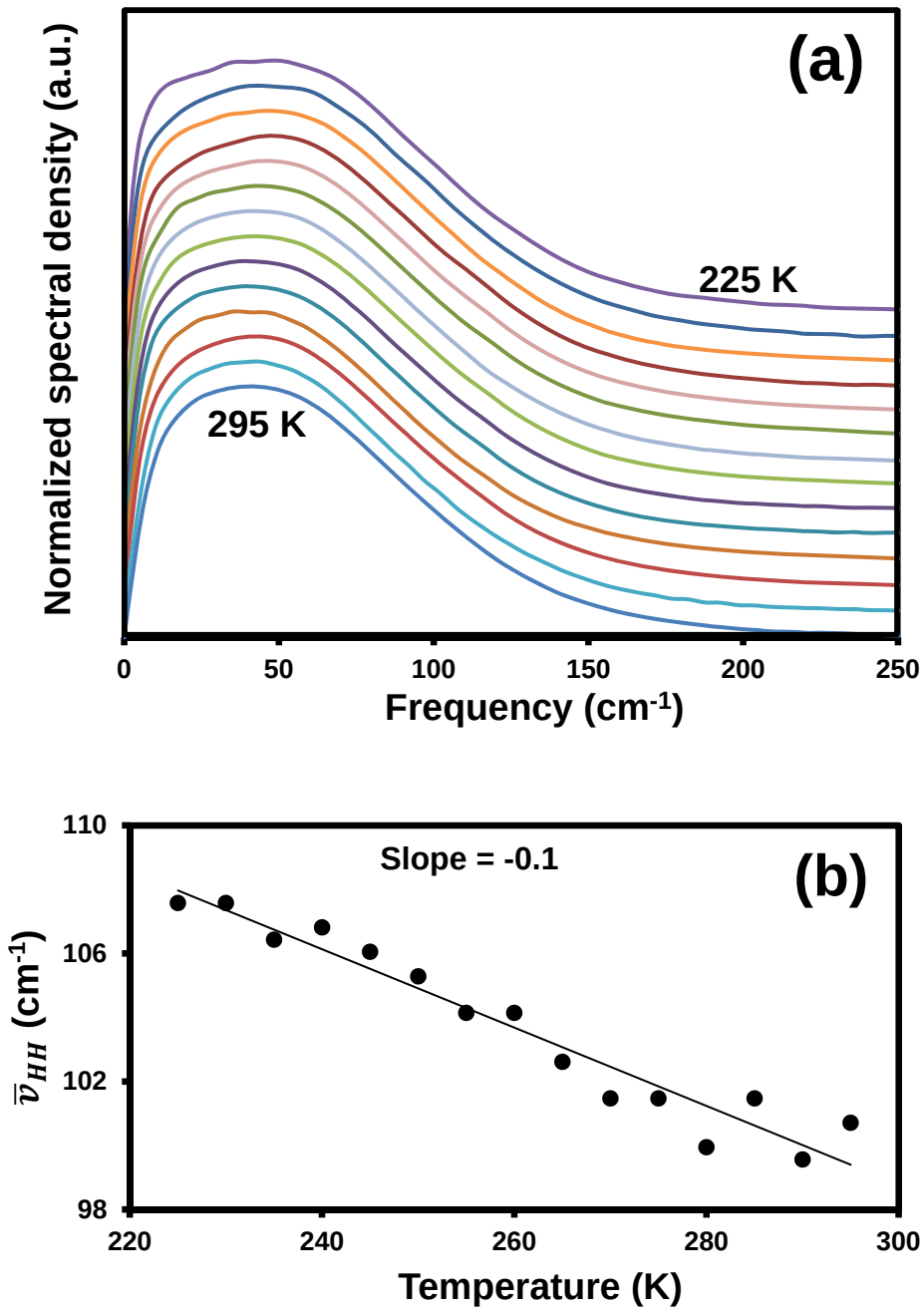

Figure 4.19 (a) Height-normalized RSDs for acetonitrile at temperatures ranging from 225 to 295 K. (b) $\bar{\nu}_{HH}$ is plotted as a function of temperature for bulk acetonitrile liquid. The data have been offset for clarity. There is a linear trend in the dependence of $\bar{\nu}_{HH}$ on the temperature. The line is a linear least-squares fit to the data.

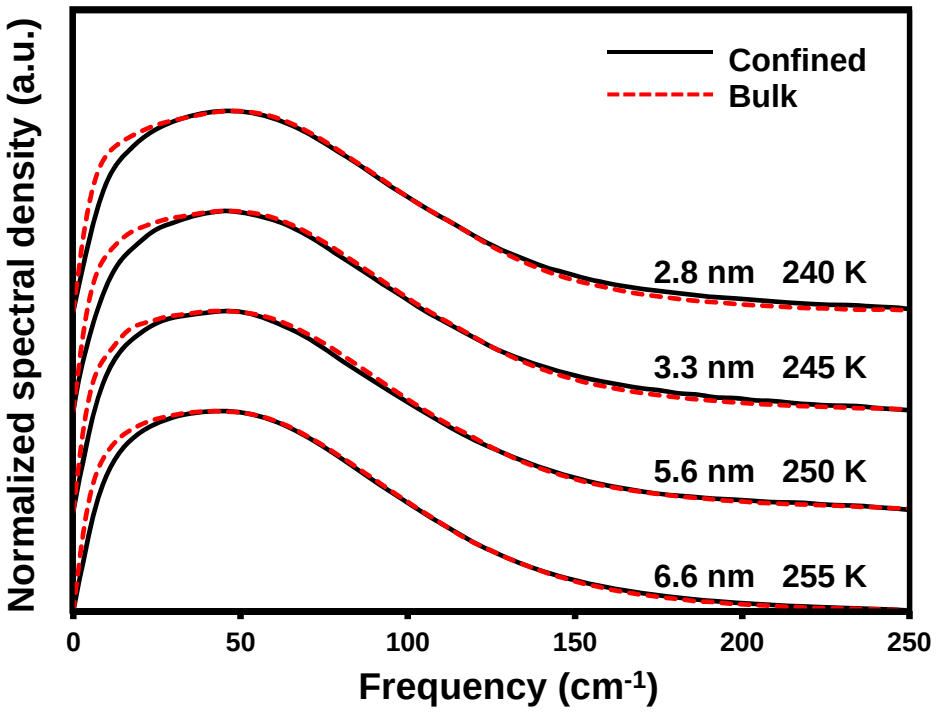

Figure 4.20 Comparison of the best matches between RSDs of bulk acetonitrile (red, dashed) and confined acetonitrile (black, solid). The RSDs have been offset for clarity.

Table 4.9 Parameters from fits of RSDs of acetonitrile in unmodified pores to a sum of a BL function and an AG function (numbers in parentheses are uncertainties in last digits solely arising from the fits; additional uncertainties inherent in the data are less than 10%).

D (nm)	ω_0 (cm^{-1})	ω_1(cm^{-1})	σ	δ	A_{AG}/A_{BL}
2.8	40.3(3)	71.6(8)	33.6(7)	0.80(1)	2.3(1)
3.3	41.2(5)	68(1)	35(1)	0.78(1)	2.3(2)
5.6	39.8(3)	70(1)	34.7(8)	0.77(1)	1.9(1)
6.6	37.9(3)	70.9(9)	34.7(7)	0.78(1)	2.2(1)
Bulk	36.5(2)	70.3(8)	33.4(7)	0.79(1)	2.0(1)

Table 4.10 Parameters from fits of RSDs of bulk acetonitrile to a sum of a BL function and an AG function (numbers in parentheses are uncertainties in last digits solely arising from the fits; additional uncertainties inherent in the data are less than 5%).

T (K)	ω_0 (cm^{-1})	ω_1(cm^{-1})	σ	δ	A_{AG}/A_{BL}
225	43.8(5)	72.2(8)	36.2(7)	0.46(1)	1.3(1)
230	42.4(7)	69(1)	40(1)	0.48(2)	1.7(1)
235	41.1(4)	71.6(8)	36.4(7)	0.54(1)	1.6(1)
240	41.1(7)	69(1)	39(1)	0.56(2)	1.9(2)
245	42.4(4)	70(1)	36.5(8)	0.57(1)	1.7(1)
250	43.3(5)	71(1)	34.2(9)	0.57(1)	1.4(1)
255	40.6(4)	69.8(9)	36.3(8)	0.58(1)	1.6(1)
260	41.7(5)	71(1)	34(1)	0.59(1)	1.4(1)
270	40.1(5)	71(1)	34(1)	0.62(2)	1.5(1)
275	39.8(5)	71(1)	33(1)	0.63(2)	1.4(1)
280	39.5(4)	70(1)	31(1)	0.68(1)	1.3(1)
285	39.1(5)	68(1)	35(1)	0.66(2)	1.8(1)
290	36.4(3)	69(1)	34(1)	0.75(1)	1.9(1)

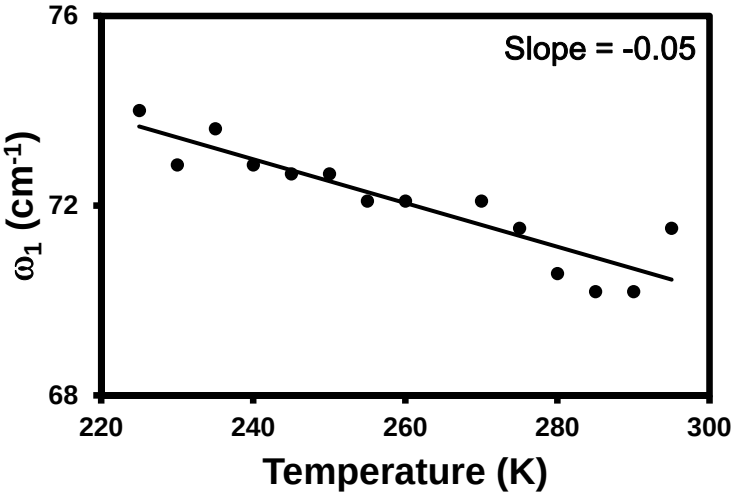

Figure 4.21 First moments of the AG portion of fits to RSDs of bulk acetonitrile plotted as a function of the pore curvature. The line is a linear least-squares fit to the data.

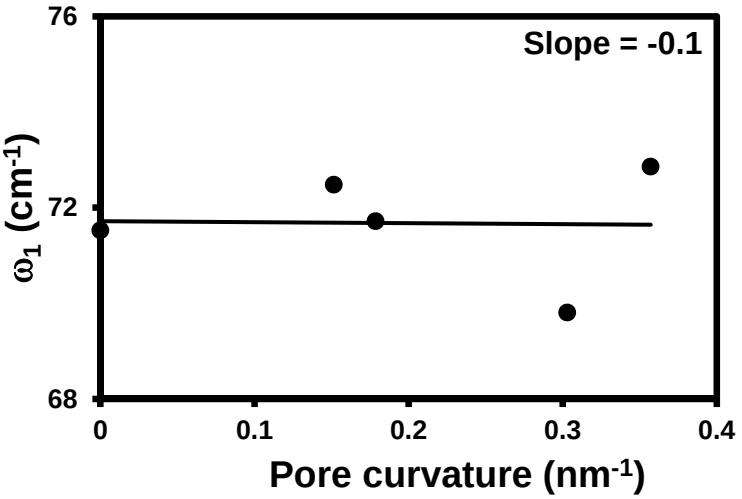

Figure 4.22 First moments of the AG portion of fits to RSDs of acetonitrile confined in unmodified pores are plotted as a function of the pore curvature. The line is a linear least-squares fit to the data.

4.4 Conclusions

In this chapter, the dynamics of benzene, pyridine, and acetonitrile confined in sol-gel glasses was investigated using ultrafast OKE spectroscopy in the time and the frequency domains.

In the study of benzene, it was shown that the high-frequency band of the low-frequency Raman spectra of the nanoconfined benzene shifts to higher frequencies as the pore size decreases. Because a similar phenomenon is also observed in bulk benzene as the temperature decreases, this phenomenon is proposed to arise from the density increase of the liquid in the vicinity of the confining surfaces. The change of the local density of benzene near the surface is mainly induced by the interaction between the π-electrons of benzene molecules and the silanol groups on the surface, which is supported by the fact that the benzene molecules prefer to lie

flat on the surface in the simulations carried out by Coasne *et al*.[81] The empirical fitting of the RSDs for nanoconfined benzene and bulk benzene at different temperatures shows that the first moment of the AG function increases linearly with the enlargement of the pore curvature. This result confirms that the change of the density induces the shift of the high-frequency band of the RSD for nanoconfined benzene.

The study was extended to pyridine, which bears strong similarity to benzene in its RSDs.[12,30] Although pyridine has a sizable dipole moment and can interact with the silanol groups through H-bonding, when it is compared to benzene, a similar shift of the $\bar{\nu}_{HH}$ can be observed. The fitting results of the RSDs for nanoconfined pyridine has similar trend in the first moment of the AG function as a function of the pore curvature. The plots of fractional shift $\bar{\nu}_{HH}/\bar{\nu}_{HH,bulk}$ versus pore curvature of benzene and pyridine are shown in Figure 4.23. The slopes of these plots are on the same order of magnitude: 1.2 /nm^{-1} for benzene and 1.9 /nm^{-1} for pyridine. The differences in the slope is possibly ascribed from the different interactions between molecules.

Nanoconfined acetonitrile also exhibits a blue shift of the high-frequency edge of RSDs as the increase of the pore curvature. Based on the results of the temperature-controlled experiments in bulk acetonitrile, it is evident that the increase of the liquid density can induce a blue shift of the high-frequency edge of the RSDs. Fitting indicates that the first moment of the AG function has a similar shift as the change of $\bar{\nu}_{HH}$, suggesting that the change of density can contribute to the change of the frequency of librational motions. The same blue shift of the high-

frequency edge of the RSDs has been observed in nanoconfined acetonitrile, however, the fitting result of the RSDs shows that little variation in the first moment of the AG function as the pore curvature increases.

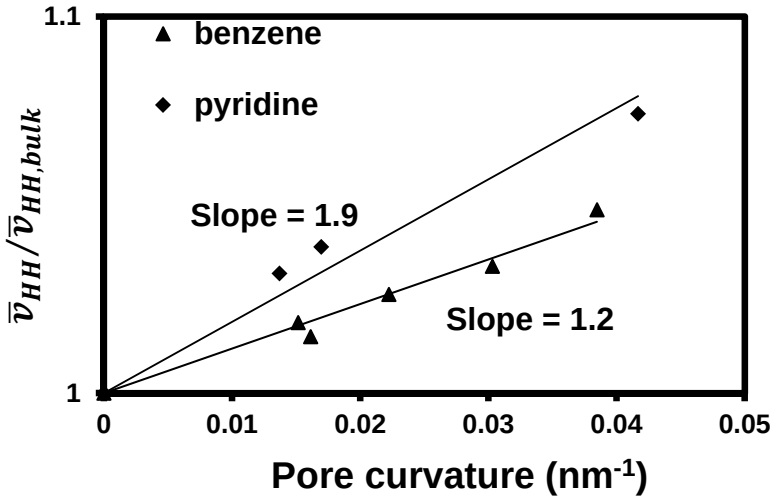

Figure 4.23 Plots of fractional shift ($\bar{\nu}_{HH}/\bar{\nu}_{HH,bulk}$) on the falling edge of RSDs as a function of pore curvature of the confinement for benzene (triangle) and pyridine (diamond). The lines are linear least-squares fits to the data.

To explore this idea further, molecular dynamics simulations should be performed to evaluate the relative importance of density and temperature in the shift of $\bar{\nu}_{HH}$ in the RSDs of the bulk benzene, pyridine, and acetonitrile.

Chapter 5: The Structure and Dynamics of Liquid Alkyl Cyanides at Interfaces

5.1 Introduction

Alkyl cyanides, which are composed of a polar cyanide group and an alkyl tail, are an interesting class of liquids for studying interfacial behavior.[89] The alkyl moiety is nonpolar and does not interact strongly with other functional groups, whereas the cyanide group is highly polar and has some tendency to dipole pair in the liquid state.[86] The cyanide group also has the ability to accept hydrogen bonds and to interact with other polar groups.[90] These interactions can induce interesting structural phenomena in liquids and can influence the organization of the alkyl cyanide molecules at interfaces.[45,63,91,92]

Although much is known about the structure and dynamics of alkyl cyanides, probing them at surfaces has proven to be challenging.[89] In general, a lack of surface-selective techniques and the relatively small amount of the molecules at surfaces makes the detection difficult. Our group has used vibrational sum-frequency-generation (VSFG) spectroscopy to gain insight into the interfacial organization of alkyl cyanides.[89,93–98] Meanwhile, OHD-OKE spectroscopy, which offers extraordinarily high signal-to-noise ratios, can be used to explore the dynamics of these liquids in confinement.[40,44,89,99] In previous studies in our group,[89] it was shown that this combination of OHD-OKE and VSFG spectroscopies can provide a detailed picture of interfacial behavior of liquids at silica surfaces.

Acetonitrile is the simplest alkyl cyanide, and its interfacial structure and dynamics have been studied extensively previously through molecular dynamics simulations and spectroscopic methods.[21,87,88,100,89] Acetonitrile molecules have a tendency for antiparallel dipole pairing in the liquid state, and further can form a lipid-like bilayer at surfaces and interfaces.[86,88] It has also been found that the signature of this bilayer structure can propagate more than 20 Å from a silica surface.[86,88,89]

The interfacial structure and dynamics of other alkyl cyanides have received less attention. Compared to acetonitrile, the longer chain in other alkyl cyanides introduces additional steric hindrance and packing constraints that can influence intermolecular ordering at interfaces. At the same time, increasing the length of the alkyl tail changes the balance between polar and dispersive interactions among the liquid molecules, which also has impact on the interfacial structure and dynamics of the liquid.[45] For alkyl cyanides with bulkier alkyl tails, the formation of an interdigitated or entangled bilayer is expected to be precluded.[94] However, whether the steric constraints presented by the structure of a bulky alkyl tail can prevent bilayer formation is unknown.

The goal of the work presented in this chapter is to investigate the effects that increasing the length of the alkyl tail (in this case, by one methylene group to make propionitrile, also known as ethyl cyanide) and the size of the terminal group (in this chapter, trimethyl acetonitrile, which has a *tert*-butyl group) have on the interfacial structure and dynamics of these liquids. My results is complementary to those of VSFG spectroscopy studies performed by my colleagues.[93,94] The combination of these results obtained from these two techniques offers a deeper understanding

of the microscopic interfacial behavior of longer and bulkier alkyl cyanides at silica surfaces.

5.2 Experiments

Spectrophotometric grade propionitrile and trimethyl acetonitrile (TMACN, Aldrich, 99+%) were used for the studies presented in this chapter. The OKE apparatus and the preparation of confined liquid samples were described in Chapter 2. The four sol-gel samples used in studies of propionitrile had average pore diameters of 25 Å, 26 Å, 43 Å, and 73 Å. Another four sol-gel samples were used in studies of TMACN, with average pore diameters of 28 Å, 42 Å, 59 Å, and 73 Å. All of these samples had an average deviation in pore diameter of about ±10% (as measured by nitrogen adsorption and desorption[54]). One piece of the sol-gel monolith sample of each pore diameter was sealed in a 2-mm-path-length cell that is filled with the appropriate liquid. OKE data were obtained for the different pore sizes by ensuring that the pump and the probe beams overlapped spatially only within the monolith. Bulk OKE data were obtained in the same sample cell. All data were collected at a temperature of 295 K.

10 OKE scans with a stepsize of 0.667 fs were taken for each sample, with 5 scans at a positive heterodyne angle and the rest at a negative heterodyne angle. After averaging the decays for each heterodyne angle independently, the averaged data sets for opposite heterodyne angles were subtracted to obtain the pure heterodyne decay. The decays were then integrated to obtain the collective orientational correlation function. Data analysis was performed with a LabView program.

5.3 Results and Discussion

5.3.1 Propionitrile

VSFG is a spectroscopic technique that can be used to provide information regarding the molecular organization at interfaces.[97] This technique is highly sensitive to the chemical composition, orientation, and ordering of molecular groups at an interface.[101] The input beams used for broadband VSFG spectroscopy are a frequency-fixed visible beam and a frequency-tunable infrared beam. These two beams are overlapped temporally and spatially at the interface to generate the output signal beam. The frequency of the signal is the sum of the frequencies of the two input beams. By tuning the frequency of the infrared beam, vibrations with different frequencies can be probed.

The incident or output beams can be either *S*-polarized or *P*-polarized, as defined in Figure 5.1. There are four typical combinations of these polarizations: *SSP*, *SPS*, *PPP*, and *PSS*. Conventionally, we name the spectrum according to the polarization combination of beams in the order of decreasing frequency. For example, the *SSP* spectrum is the spectrum collected with the signal beam *S*-polarized, the visible beam *S*-polarized, and the infrared beam *P*-polarized.

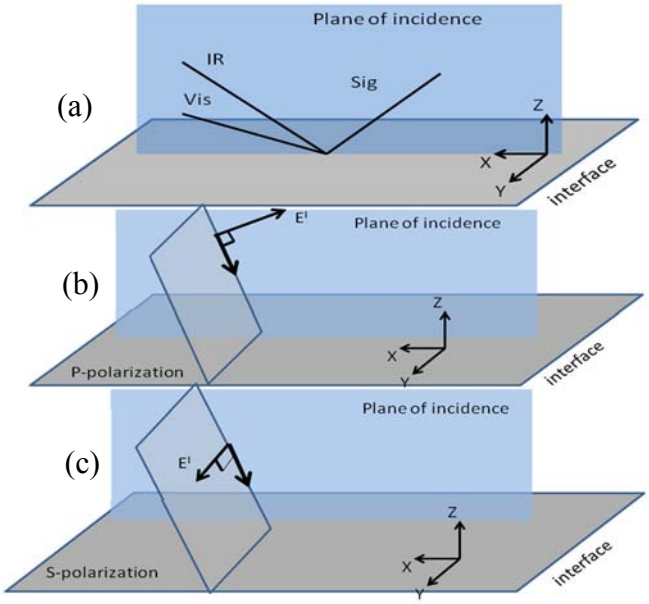

Figure 5.1 Illustration of the beam polarizations in VSFG spectroscopy. (a) Three beams are involved in VSFG spectroscopy. (b) For *P*-polarized light, the electric field (E^I) of the incident light is in the plane of incidence. (c) For *S*-polarized light, E^I is perpendicular to the plane of incidence. This figure is adapted from the reference 100.[101]

At the silica/liquid interface of propionitrile, the VSFG spectra under the *SSP* and *PPP* polarization conditions are dominated by a single peak at 2940 cm^{-1}, as shown in Figure 5.2. The dominant peak arises from the symmetric methylene stretch of propionitrile, which occurs at a different frequency for molecules in the liquid as opposed to molecules that interact directly with the silica surface.[93] Compared to the silica/vapor interface or liquid/vapor interface of propionitrile,[93] the spectrum at the silica/liquid interface does not have many peaks, indicating a strong cancellation caused by the lipid-bilayer-like structure at the interface. This picture is further supported by the fact that spectra at different polarizations can be best fit

by a sum of two Lorenztians with opposite signs and different center frequencies, as is the case for acetonitrile.[89]

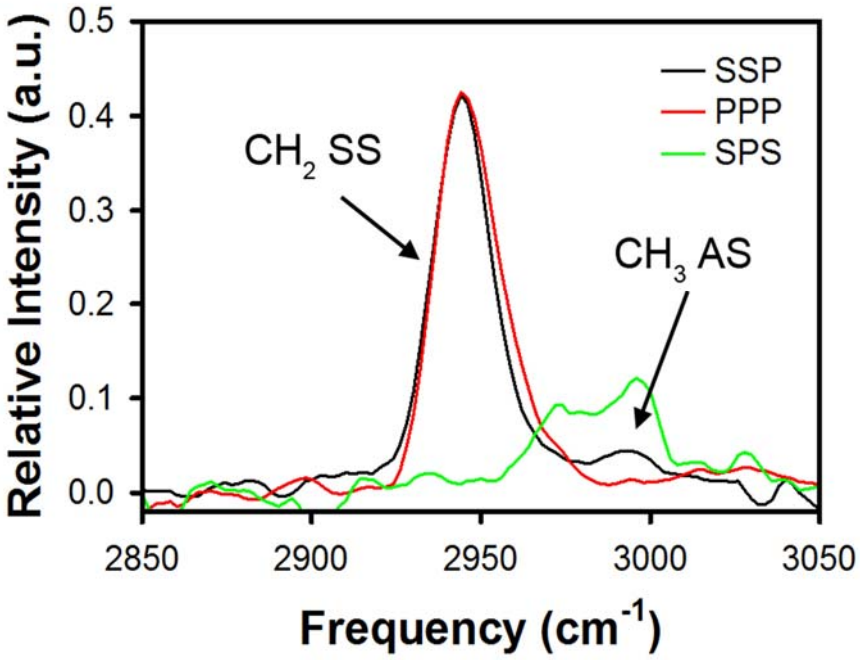

Figure 5.2 VSFG data for propionitrile at the silica/liquid interface under *SSP* (black), *PPP* (red) and *SPS* (green) polarization conditions. These data were obtained by Ding *et al*.[93]

The collective orientational correlation functions corresponding to the OKE decays for bulk and confined propionitrile are shown in Figure 5.3. The logarithmic plot of the collective orientational decay for bulk propionitrile is linear at long times, indicating that this portion of the decay can be fit by a single exponential function. The fitting of the data of bulk propionitrile liquid yields time constant of 2.98 ps, which is in good agreement with previous results.[45]

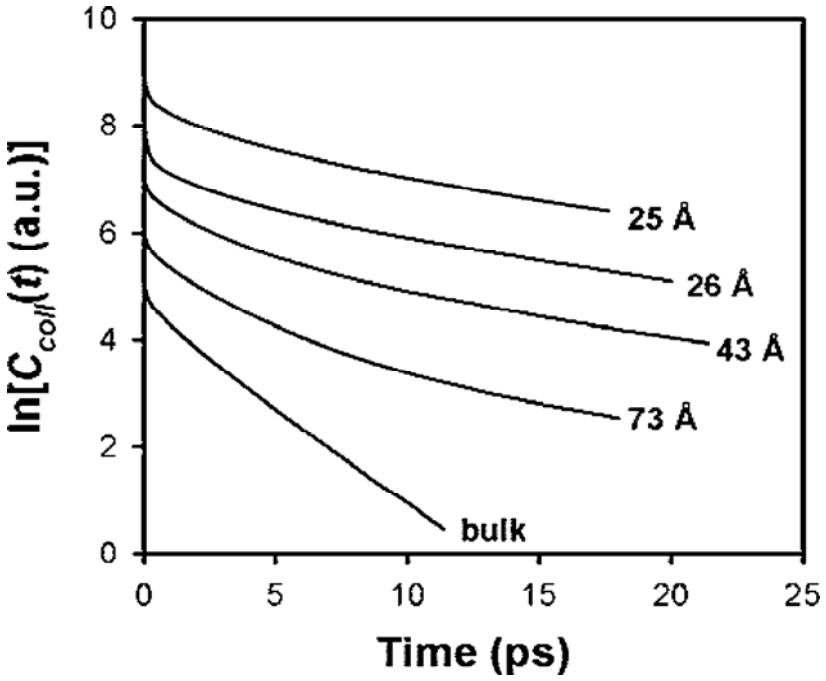

Figure 5.3 Collective orientational correlation functions for liquid propionitrile in the bulk and confined in silica sol-gel glasses with different pore diameters. The correlation functions have been offset for clarity.

Confined liquids exhibit collective orientational diffusion that is considerably slower than that of the bulk liquid, with smaller pores having larger average decay times. The diffusive orientational portion of the integrated OKE data for the confined liquids in each pore size was fit to a biexponential decay of the form:

$$C_{coll}(t) = A_1 \exp\left(-\frac{t}{\tau_1}\right) + A_2 \exp\left(-\frac{t}{\tau_2}\right), \qquad \text{(Eq. 5.1)}$$

where we define τ_1 to be the faster of the two orientational correlation times. The value of τ_1 was close to the collective orientational correlation time for the bulk liquid, and the exponential with a slower decay constant had nearly the same time constant in all pore sizes (13.3 ps). We therefore refit the data by constraining τ_1 to be the same as the bulk collective orientational time, constraining τ_2 to be 13.3

ps, and allowing only the values of A_1 and A_2 to vary. The resultant amplitudes for these new biexponential fits are given in Table 5.1.

Table 5.1 Parameters from fits of integrated propionitrile OKE data. The fitting function is given in Eq. 5.1 with τ_1 = 2.98 ps (the bulk relaxation time) and τ_2 = 13.3 ps.

Pore Diameter	A_1/A_2
73 Å	4.2(2)
43 Å	1.8(1)
26 Å	0.86(4)
25 Å	0.90(4)

For many different confined liquids (including acetonitrile), we have observed multiexponential OKE decays[20] in which the fastest component of the collective orientational diffusion has a time constant that matches that of the bulk liquid. Our interpretation for this type of behavior is that liquid molecules in the pore centers have bulk-like dynamics, whereas liquid molecules that interact with the pore surfaces have inhibited orientational dynamics that result in slower decays. The inhibition of surface dynamics can arise from a combination of geometrical effects, an increased hydrodynamic volume for reorientation, and specific interactions with the surface. In the case of propionitrile, specific interactions arise from the polar and hydrogen-bond-donating nature of the silica surface.

The amplitudes of the two exponentials can be used to estimate the thickness of the surface layer with inhibited dynamics (R_s) using the equation[41]:

$$R_s = \frac{D}{2}\left(1 - \sqrt{A_1}\right), \qquad \text{(Eq. 5.2)}$$

where D is the pore diameter of the sol-gel glass. This formula assumes that the pores are cylindrical. The true surface area of the pores is undoubtedly greater than for a cylindrical system, and so this equation can be viewed as providing an upper limit to the surface-layer thickness. The estimated thickness as a function of the pore size is shown in Figure 5.4. The measured thicknesses are the same to within the uncertainty in these estimates, and the average thickness is about 4.0 Å.

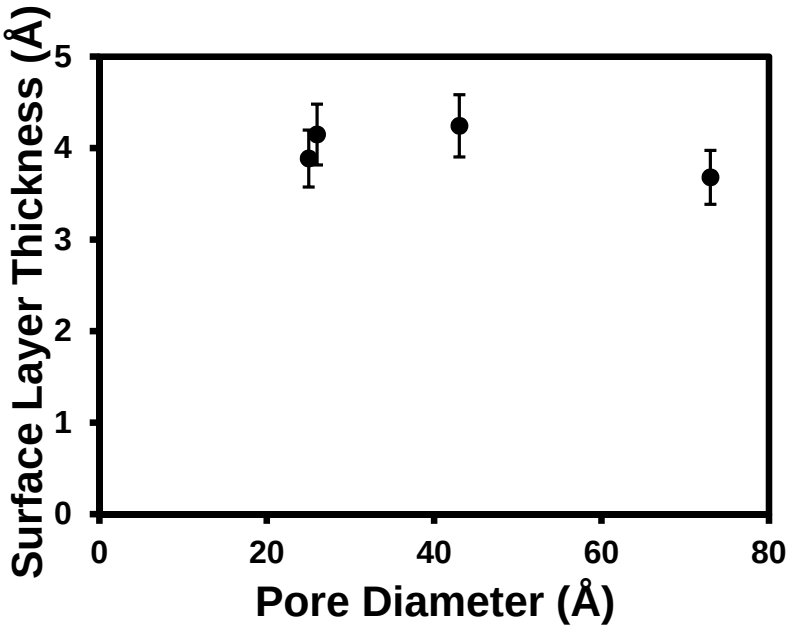

Figure 5.4 Estimated thickness of the surface layer of propionitrile molecules with inhibited orientational dynamics as a function of pore diameter.

For confined acetonitrile, the entire surface layer has dynamics that are slower than those of the bulk, and half of the surface layer has extremely slow dynamics.[51] Therefore, it was proposed that about half of the surface molecules are

hydrogen-bonded to the surface and that the other half are interdigitated among them, with the cyanide group pointing away from the surface.[51] The molecules bonded to the surface are the ones with the extremely slow dynamics, whereas the rest can relax more rapidly by exchanging into the bulk-like portion of the confined liquid.[51] The thickness of the dynamically inhibited surface layer at room temperature was approximately the length of one molecule (slightly greater than 4 Å).[89]

We expect the structure and dynamics of propionitrile at the liquid/silica interface to differ from those of acetonitrile. In the simulations performed by performed by Liu *et al*,[102] it has been shown that although the alkyl group of propionitrile is longer than that of acetonitrile, the thickness of the bilayer is about the same for the two liquids. This result implies that the alkyl tails of propionitrile are significantly entangled, which could prevent exchange of molecules from the second sublayer into the bulk-like population of liquid. In our OKE studies, the thickness of the surface layer with inhibited dynamics is smaller in propionitrile than it is for acetonitrile, but is in good agreement with the bilayer thickness observed in simulations (although the full bilayer thickness in the simulation is about 4.9 Å, a vast majority of the molecules in the first density peak have their center of mass at a distance of 4 Å or less from the surface).[102] We therefore conclude that both sublayers of the surface propionitrile bilayer have inhibited dynamics. The simulations also indicate that there are additional propionitrile bilayers at greater distance from a flat silica interface,[102] and this is likely to be the case in silica pores based on simulations of acetonitrile.[87] However, it is the strong interaction of the first bilayer with the pore surface that leads to the inhibited orientational dynamics, and we

expect additional bilayers to have orientational dynamics that are similar to those of the bulk liquid.

5.3.2 Trimethyl acetonitrile (TMACN)

The VSFG spectra for the silica/liquid interface of TMACN are less complex than those for other interfaces (Figure 5.5). The signal intensity is also relatively low in the silica/liquid spectra,[94] suggesting that there is a substantial amount of signal cancellation at the silica/liquid interface. However, the existence of a significant signal under all polarization conditions suggests that there is not a well-formed bilayer at this interface, in contrast to the results for acetonitrile and propionitrile.

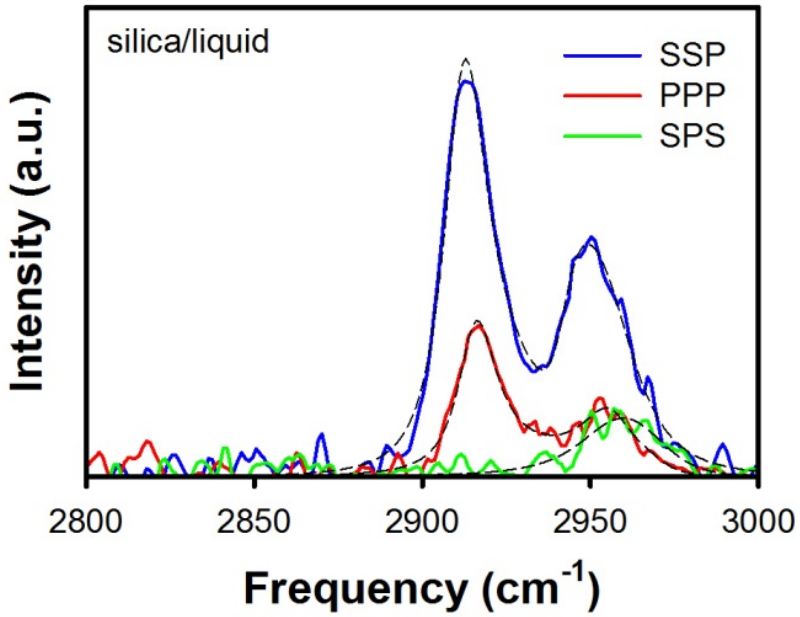

Figure 5.5 VSFG spectra (solid lines) for TMACN at the silica/liquid interface. The *SSP* spectrum is shown in blue, the *PPP* spectrum is shown in red, and the *SPS* spectrum is shown in green. The dashed lines are fits to a sum of Lorentzians. These data were obtained by Ding *et al*.[94]

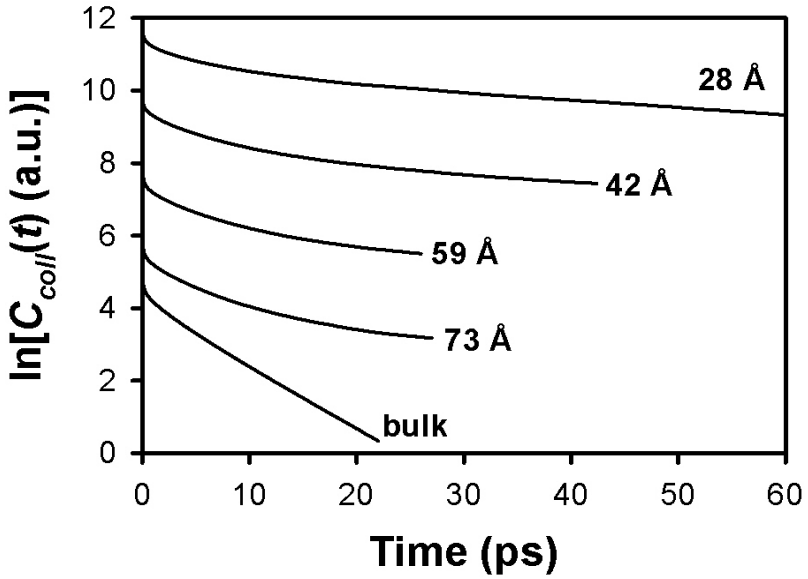

Figure 5.6 Collective orientational correlation functions for TMACN in the bulk and in silica pores of different diameters. The correlation functions have been offset for clarity.

The collective orientational correlation functions for TMACN in the bulk and confined in silica pores of different diameters are shown in Figure 5.6. The diffusive contribution to $C_{coll}(t)$ for the bulk liquid is clearly exponential, and a fit yields a time constant of 5.98 ps. Similar to propionitrile, the collective diffusion of confined TMACN is slower than that of the bulk liquid, with smaller pores having larger average decay times. The data can be well fit by a sum of two exponentials. The faster of the two observed relaxations has a time constant that is the same as that of the bulk liquid to within the accuracy of the fits. The slower relaxation has the same time constant in all pore sizes studied to within the accuracy of the fits. Therefore, all the decays were refit with the constraints that τ_1 = 5.98 ps and

τ_2 = 50 ps (the average value from free fits of the collective orientational correlation functions for the confined liquid). The fitting results are listed in Table 5.2.

Table 5.2 Parameters from fits of integrated TMACN OKE data. The fitting function is given in Eq. 5.1 with τ_1= 5.98 ps (the bulk relaxation time) and τ_2= 50 ps.

Pore Diameter	A_1/A_2
73 Å	3.7(2)
59 Å	2.3(1)
42 Å	1.9(1)
28 Å	0.96(5)

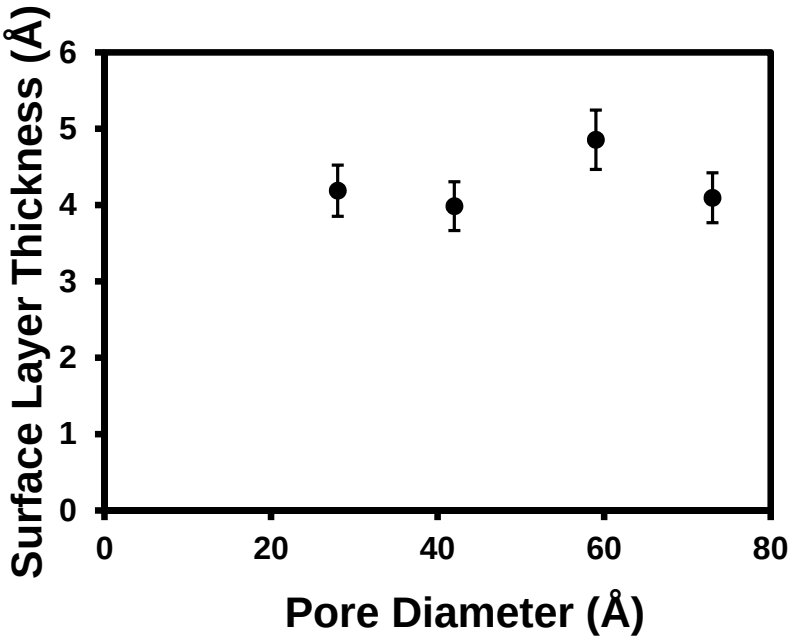

Figure 5.7 Estimated thickness of the surface layer of TMACN with inhibited dynamics as a function of pore diameter.

Using Eq. 5.2, the surface-layer thickness of molecules with inhibited dynamics was calculated. The resultant thicknesses in different pores are presented in Figure 5.7. The averaged thickness of the surface layer for TMACN is 4.3 Å. To within the uncertainty of the estimate, the surface layer thickness is identical for all pore sizes and this value is roughly the length of one TMACN molecule, which suggests that there is a surface monolayer of TMACN molecules that accept hydrogen bonds from the silica surface and thus experience hindered dynamics. As the *tert*-butyl groups of TMACN molecules are too bulky to permit interdigitation or entanglement, this surface layer thickness is consistent with hindered orientational dynamics being experienced only by molecules that accept hydrogen bonds or otherwise interact directly with the pore surfaces. The bulk of the *tert*-butyl group should also prevent the C≡N groups of these surface molecules from adopting as large an angle with surface normal as that observed in propionitrile.

Comparing all the figures and tables above, it is evident that the orientational behavior of TMACN in confinement closely resembles that of propionitrile. TMACN molecules within the confinement can be divided as hydrogen-bonded interfacial molecules, which have extremely slow orientational motion, and bulk-like molecules, which can reorient just like molecules in bulk TMACN. Therefore, as expected, the bulk of the *tert*-butyl group in TMACN prevents it from forming an interdigitated structure at the silica/liquid interface. This conclusion is also consistent with the VSFG results.

5.4 Conclusions

In this chapter, the dynamics of confined propionitrile and confined TMACN were investigated and compared to those of acetonitrile. Interactions with the silica interface manifested dynamically by a significant increase in the orientational correlation time of the adsorbed layer of molecules in confined propionitrile and confined TMACN liquid.

In confined propionitrile, the orientational dynamics of the non-adsorbed molecules in the bilayer resemble those of the remaining liquid in the pores. The measured surface-layer thickness of dynamically inhibited molecules is similar to that of acetonitrile, which suggests that the alkyl chains are entangled for the absorbed layer of molecules.

As the alkyl group of acetonitrile is replaced with *tert*-butyl group, the scenario is quite different from the one for increasing the length of the alkyl group. OKE studies on TMACN indicate that only one monolayer of TMACN molecules experiences dynamic inhibition at the surfaces of silica pores.

Taken together, our results highlight the importance of the structure of the alkyl chains in determining the molecular organization and dynamics of alkyl cyanides in confinement. It will be of great interest to explore how longer and/or bulkier alkyl groups (and the corresponding changes in intermolecular forces) influence the interfacial behavior in other liquid alkyl cyanides.

Chapter 6: Conclusions and Future Prospects

6.1 Conclusions

The research presented in this thesis demonstrates that OKE spectroscopy is a powerful nonlinear optical technique for probing the collective orientational dynamics and the intermolecular dynamics of liquids. A few important conclusions have been reach that point the way towards additional fertile areas of research on the dynamics of liquids.

OKE spectroscopy allows for the acquisition of high-quality, Bose-Einstein-corrected, low-frequency Raman spectra in liquids. Although the molecular interpretation of these spectra remains an open problem, the studies presented in this thesis demonstrate the potential of using the RSD to understand the intermolecular dynamics of liquids.

The high-frequency portion of the RSDs of benzene and its isotopologues can be superimposed. The observed frequency-scaling factors are virtually identical to the scaling factors calculated based on the moment of inertia, but do not match with the scaling factors calculated based on molecular weight scaling. This result implies that the high-frequency portion of the RSD is dominated by librational scattering. The empirical fitting of RSDs to the sum of a BL and an AG function is employed to evaluate the relative importance of hindered rotations and hindered translations in the RSD. The first moment of the AG portion and the first moment of the BL portion of the fits can both scale linearly with the inverse of the square root of the moment of inertia. This result suggests that hindered rotations

are the major contributor to the RSD. In addition, a strong translation-rotation coupling is revealed for benzene, because the decay times of the orientational relaxation of benzene and its isotopologues scale linearly with the inverse of molecular weight as well as the inverse of the square root of the moment of inertia.

OKE spectroscopy was also used to study the dynamics of nanoconfined liquids. In the study on nanoconfined benzene, the thickness of the surface-layer molecules is found to be 2.6 Å, implying that the benzene molecules lie flat on the confining surfaces. A shift of the high-frequency portion of the RSD of confined benzene has been observed and is proposed to arise from the change of liquid density. This model has been tested in similar studies on pyridine and acetonitrile. Although pyridine and acetonitrile are different from benzene in many ways, similar phenomena have been observed in their RSDs. Thus, it is believed that this density effect in the RSD is likely to hold for a wide variety of confined liquids.

To investigate the effects of increasing the length of the alkyl tail and the size of the terminal group on the interfacial structure and dynamics of the alkyl cyanides in confinement, OKE spectroscopy has been used to study the dynamics and structure of the nanoconfined propionitrile and trimethyl acetonitrile. The OKE spectra suggest that the thickness of the dynamically inhibited surface-layer is about the same for propionitrile and acetonitrile. This result suggests that propionitrile molecules are prone to be entangled at the confining surface. As a result of this entanglement, propionitrile molecules in confinement can be grouped into interfacial molecules, which can form two antiparallel entangled sublayers and have extremely slow orientational motion, and bulk-like molecules, which can reorient as

molecules in bulk propionitrile. In the study on TMACN, because the bulky *tert*-butyl group prevents the formation of the interdigitate structure, the results obtained from the OKE spectra suggest that the orientational behavior of TMACN in confinement closely resembles to that of propionitrile: molecules in the pore center can reorient as bulk liquid and molecules adjacent to the confining surface have significantly frustrated reorientation relaxation. However, there is only one monolayer of dynamically hindered molecules observed in nanoconfined TMACN in the vicinity of the confining surface.

6.2 Future Prospects

Some possible directions for future work are:

1. In Chapter 3, I demonstrated that hindered rotation plays a major role in the RSD of benzene liquid. Because the RSDs of pyridine and benzene resemble each other closely, it will be interesting to evaluate the relative importance of hindered rotations in the RSDs of pyridine as well. In addition, an enhancement in the low-frequency region of RSDs for benzene isotopologues containing six ^{13}C atoms is observed. The source of this enhancement needs to be investigated in the future.
2. In the study of the density effect on nanoconfined pyridine and acetonitrile, the confining surfaces have been modified to lessen the interactions between liquid molecules and the surfaces. The dynamics of pyridine and acetonitrile in such confinement could be studied using OKE spectroscopy to gain better insights into the density effect on liquid dynamics.

Bibliography

(1) Fourkas, J. T. *Liquid Dynamics Experiment, Simulation, and Theory*; American Chemical Society Books.: Washington, 2002.

(2) Price, D. L.; Trouw, F. R. *Annu. Rev. Phys. Chem.* **1999**, *50*, 571–601.

(3) Fourkas, J. T. *Nonresonant Intermolecular Spectroscopy of Liquids, in Ultrafast Infrared and Raman Spectroscopy*; Fayer, M. D., Ed.; Marcel Dekker: New York, 2001; pp. 473–512.

(4) Kindt, J. T.; Schmuttenmaer, C. A. *J. Phys. Chem.* **1996**, *3654*, 10373–10379.

(5) Duguay, M. A.; Hansen, J. W. *Appl. Phys. Lett.* **1969**, *15*, 192–194.

(6) Righini, R. *Science.* **1993**, *262*, 1386–1390.

(7) S. Kinoshita, Y. Kai, T. Ariyoshi, Y. S. *Int. J. Mod. Phy. B* **1996**, 1229–1336.

(8) Smith, N. A.; Meech, S. R. *Int. Rev. Phys. Chem.* **2002**, *21*, 75–100.

(9) McMorrow, D. *Opt. Commun.* **1991**, *86*, 236–244.

(10) McQuarrie, D. A. *Statistical Mechanics*; Harper and Row: New York, 1976; p. 472.

(11) McMorrow, D.; Lotshaw, W. T.; Kenney-Wallace, G. A. *IEEE J. Quantum Electron.* **1988**, *24*, 443–454.

(12) Zhong, Q.; Fourkas, J. T. *J. Phys. Chem. B* **2008**, *112*, 15529–15539.

(13) Bucaro, J. A. *J. Chem. Phys.* **1971**, *54*, 3846–3853.

(14) Chang, Y. J.; Castner, E. W. *J. Phys. Chem.* **1996**, *100*, 3330–3343.

(15) Cang, H.; Li, J.; Fayer, M. D. *Chem. Phys. Lett.* **2002**, *366*, 82–87.

(16) Li, J.; Wang, I.; Fayer, M. D. *J. Phys. Chem. B* **2005**, *109*, 6514–6519.

(17) Shirota, H.; Castner, E. W. *J. Phys. Chem. A* **2005**, *109*, 9388–9392.

(18) Castner, E. W.; Wishart, J. F.; Shirota, H. *Acc. Chem. Res.* **2007**, *40*, 1217–1227.

(19) Loughnane, B. J.; Scodinu, A.; Fourkas, J. T. *Chem. Phys.* **2000**, *253*, 323–330.

(20) Loughnane, B. J.; Farrer, R. A.; Scodinu, A.; Reilly, T.; Fourkas, J. T. *J. Phys. Chem. B* **2000**, *104*, 5421–5429.

(21) Loughnane, B. J.; Farrer, R. A.; Fourkas, J. T. *J. Phys. Chem. B* **1998**, *102*, 5409–5412.

(22) Drake, J. M.; Klafter, J. *Molecular Dynamics in Restricted Geometries*; Wiley: New York, 1989.

(23) Drake, J. M., Klafter, J., Kopelman, R., Awschalom, D. D. *Dynamics in Small Confining Systems*; Materials Research society: Pittsburgh, PA, 1993; p. 377.

(24) Drake, J. M., Klafter, J., Kopelman, R., Troian, S. M. *Dynamics in Small Confining Systems II*; Materials Research society: Pittsburgh, PA, 1995; p. 466.

(25) Drake, J. M., Klafter, J., Kopelman, R. *Dynamics in Small Confining Systems III*; Materials Research Society: Pittsburgh, PA, 1997; p. 388.

(26) Drake, J. M.; Grest, G. S.; Klafter, J.; Kopelman, R. *Dynamics in Small Confining Systems IV*; Materials Research Society: Warrendale, PA, 1999; p. 372.

(27) Jackson, C. L.; McKenna, G. B. *J. Chem. Phys.* **1990**, *93*, 9002–9011.

(28) Zhang, J.; Liu, G.; Jonas, J. *J. Phys. Chem.* **1992**, *96*, 3478–3480.

(29) Alba-Simionesco, C.; Dosseh, G.; Dumont, E.; Frick, B.; Geil, B.; Morineau, D.; Teboul, V.; Xia, Y. *Eur. Phys. J. E* **2003**, *12*, 19–28.

(30) Zhong, Q.; Fourkas, J. T. *J. Phys. Chem. B* **2008**, *112*, 15342–15348.

(31) Mayer, G.; Gires, F. *Comptes Rendus* **1964**, *258*, 2039–2042.

(32) Levenson, M. D.; Eesley, G. L. *Appl. Phys. Lett.* **1979**, *19*, 1–17.

(33) Hunt, N. T.; Jaye, A. A.; Meech, S. R. *Phys. Chem. Chem. Phys.* **2007**, *9*, 2167–2180.

(34) Berne, B. J.; Pecora, R. *Dynamic Light Scattering*; Wiley: New York, 1976.

(35) Debye, P. *Polar Molecules*; Literary Licensing, LLC: Dover, New York, 1929.

(36) Born, M.; Oppenheimer, J. R. *Ann. Phys.* **1927**, *84*, 457–484.

(37) Brinker, C. J.; Scherer, G. W. *Sol−Gel Science: the Physics and Chemistry of Sol−Gel Processing*; Academic Press: San Diego, CA, 1990.

(38) Shafer, M. W.; Awschalom, D. D.; Warnock, J.; Ruben, G. *J. Appl. Phys.* **1987**, *61*, 5438–5446.

(39) Warnock, J.; Awschalom, D. D.; Shafer, M. W. *Physcial Rev. B* **1986**, *34*, 475–478.

(40) Farrer, R. A.; Fourkas, J. T. *Acc. Chem. Res.* **2003**, *36*, 605–612.

(41) Farrer, R. A.; Loughnane, B. J.; Fourkas, J. T. *J. Phys. Chem. A* **1997**, *02167*, 4005–4010.

(42) Loughnane, B. J.; Fourkas, J. T. *J. Phys. Chem. B* **1998**, *102*, 10288–10294.

(43) Loughnane, B. J.; Scodinu, A.; Fourkas, J. T. *J. Phys. Chem. B* **1999**, *103*, 6061–6068.

(44) Zhu, X.; Farrer, R. A.; Fourkas, J. T. *J. Phys. Chem. B* **2005**, *109*, 12724–12730.

(45) Zhu, X.; Farrer, R. A.; Zhong, Q.; Fourkas, J. T. *J. Phys. Condens. Matter* **2005**, *17*, 4105–4118.

(46) Chang, Y. J.; Castner, E. W. *J. Chem. Phys.* **1993**, *99*, 7289–7299.

(47) Wang, X. D.; Tang, Y.; Wang, Y. J.; Gao, Z.; Yang, W. L.; Fu, S. K. *Chem. Commun.* **2000**, 2161–2162.

(48) Davis, M. E. *Nature* **2002**, *417*, 813–821.

(49) *Vycor 7390 Porous Glass*; Corning: Houghton Park.

(50) Brinker, C. J.; Scherer, G. W. *Sol-Gel Science: the Physics and Chemistry of Sol-Gel Processing*; Academic Press: San Diego, CA, 1990.

(51) Loughnane, B. J.; Farrer, R. A.; Scodinu, A.; Fourkas, J. T. *J. Chem. Phys.* **1999**, *111*, 5116–5123.

(52) Hench, L. L.; West, J. K. *Chem. Rev.* **1990**, *90*, 33–72.

(53) Graham, T. *J. Chem. Soc.* **1864**, *17*, 318–327.

(54) Brunauer, S.; Emmett, P. H.; Edward, T. *J. Am. Chem. Soc.* **1936**, *407*, 309–319.

(55) Kinoshita, S.; Kai, Y.; Yamaguchi, M.; Yagi, T. *Phys. Rev. Lett.* **1995**, *75*, 148–151.

(56) Kinoshita, S.; Yamaguchi, M.; Yagi, T. *Chem. Phys. Lett.* **1995**, *236*, 259–264.

(57) Murry, R. L.; Fourkas, J. T.; Li, W.; Keyes, T. *Phys. Rev. Lett.* **1999**, *83*, 3550–3553.

(58) Ryu, S.; Stratt, R. M. *J. Phys. Chem. B* **2004**, *108*, 6782–6795.

(59) Elola, M. D.; Ladanyi, B. M. *J. Phys. Chem. B* **2006**, *110*, 15525–15541.

(60) Zhong, Q.; Fourkas, J. T. *J. Phys. Chem. B* **2008**, *112*, 8656–8663.

(61) Heisler, I. A.; Meech, S. R. *J. Chem. Phys.* **2010**, *132*, 174503.

(62) Loughnane, B. J.; Scodinu, A.; Fourkas, J. T. *J. Phys. Chem. B* **2006**, *110*, 5708–5720.

(63) Zhong, Q.; Zhu, X.; Fourkas, J. T. *J. Phys. Chem. B* **2008**, *112*, 3115–3120.

(64) Loughnane, B. J.; Scodinu, A.; Farrer, R. A.; Fourkas, J. T.; Mohanty, U. *J. Chem. Phys.* **1999**, *111*, 2686–2694.

(65) Viswanath, D. S.; Ghosh, T. K.; Prasad, D. H. L.; Dutt, N. V. K.; Rani, K. Y. *Viscosity of Liquids: Theory, Estimation, Experiment, and Data*; Springer: Dordrecht, The Netherlands, 2007.

(66) Holz, M.; Mao, X.; Seiferling, D.; Sacco, A. *J. Chem. Phys.* **1996**, *104*, 669–679.

(67) Rajian, J. R.; Hyun, B.-R.; Quitevis, E. L. *J. Phys. Chem. A* **2004**, *108*, 10107–10115.

(68) Tao, G.; Stratt, R. M. *J. Phys. Chem. B* **2006**, *110*, 976–987.

(69) Zuilbof, H.; Lodder, G. *J. Phys. Chem.* **1992**, *96*, 6957–6962.

(70) Scher, C.; Ravld, B.; Halevl, E. A. *J. Phys. Chem.* **1982**, *86*, 654–658.

(71) Http://www.sigmaaldrich.com/united-states.html.

(72) Turton, D. A.; Wynne, K. *J. Chem. Phys.* **2009**, *131*, 201101.

(73) Rohne, C.; Jensby, K.; Loughnane, B. J.; Fourkas, J. T.; Nielsen, O. F.; Keiding, S. R. *J. Chem. Phys.* **2000**, *113*, 3749–3756.

(74) Shirota, H.; Fujisawa, T.; Fukazawa, H.; Nishikawa, K. *Bull. Chem. Soc. Jpn.* **2009**, *82*, 1347–1366.

(75) Gallo, P.; Ricci, M. A.; Rovere, M. *J. Chem. Phys.* **2002**, *116*, 342–346.

(76) Shirota, H. *J. Phys. Chem. A* **2011**, *115*, 14262–14275.

(77) Nakasaka, Y.; Tago, T.; Yano, K.; Masuda, T. *Chem. Eng. Sci.* **2010**, *65*, 226–231.

(78) Yi, J.; Jonas, J. *J. Phys. Chem.* **1996**, *100*, 16789–16793.

(79) Narten, A. H. *J. Chem. Phys.* **1977**, *67*, 2102–2108.

(80) Cabaço, M. I.; Danten, Y.; Besnard, M.; Guissani, Y.; Guillot, B. *J. Phys. Chem. B* **1997**, *101*, 6977–6987.

(81) Coasne, B.; Fourkas, J. T.; Normale, E. *J. Phys. Chem. C* **2011**, *115*, 15471–15479.

(82) Fury, M.; Munie, G.; Jonas, J. *J. Chem. Phys.* **1979**, *70*, 1260–1265.

(83) DiVerdi, J. A.; Kobayashi, T.; Maciel, G. E. *J. Phys. Chem. C* **2007**, *111*, 5982–5989.

(84) Liu, G.; Li, Y.; Jonas, J. *J. Chem. Phys.* **1991**, *95*, 6892.

(85) Nikiel, L.; Hopkins, B.; Zerda, T. W. *J. Phys. Chem.* **1990**, *94*, 7458–7464.

(86) Cheng, L.; Morrone, J. A.; Berne, B. J. *J. Phys. Chem. C* **2012**, *116*, 9582–9593.

(87) Morales, C. M.; Thompson, W. H. *J. Phys. Chem. A* **2009**, *113*, 1922–1933.

(88) Hu, Z.; Weeks, J. D. *J. Phys. Chem. C* **2010**, 10202–10211.

(89) Ding, F.; Hu, Z.; Zhong, Q.; Manfred, K.; Gattass, R. R.; Brindza, M. R.; Fourkas, J. T.; Walker, R. A.; Weeks, J. D. *J. Phys. Chem. C* **2010**, *114*, 17651–17659.

(90) Choi, J.-H.; Oh, K.-I.; Lee, H.; Lee, C.; Cho, M. *J. Chem. Phys.* **2008**, *128*.

(91) Bertagnolli, H.; Chieux, P.; Zeidler, M. D. *Mol. Phys.* **1976**, *32*, 1731–1736.

(92) Bertagnolli, H.; Zeidler, M. D. *Mol. Phys.* **1978**, *35*, 177–192.

(93) Ding, F.; Zhong, Q.; Manfred, K.; He, X.; Bender, J. S.; Brindza, M. R.; Walker, R. A.; Fourkas, J. T. *J. Phys. Chem. C* **2012**, *116*, 4019–4025.

(94) Ding, F.; Rivera, C. A.; Zhong, Q.; Manfred, K.; He, X.; Brindza, M. R.; Walker, R. A.; Fourkas, J. T. *J. Phys. Chem. C* **2012**, *116*, 7000–7009.

(95) Eisenthal, K. B. *Chem. Rev.* **1996**, *96*, 1343–1360.

(96) Wang, H.-F.; Gan, W.; Lu, R.; Rao, Y.; Wu, B.-H. *Int. Rev. Phys. Chem.* **2005**, *24*, 191–256.

(97) Richmond, G. L. *Chem. Rev.* **2002**, *102*, 2693–2724.

(98) Chen, Z.; Shen, Y. R.; Somorjai, G. A. *Annu. Rev. Phys. Chem.* **2002**, *53*, 437–465.

(99) Scodinu, A.; Farrer, R. A.; Fourkas, J. T. *J. Phys. Chem. B* **2002**, *106*, 12863–12865.

(100) Ladanyi, B. M.; Klein, S. *J. Chem. Phys.* **1996**, *105*, 1552–1561.

(101) Lambert, A. G.; Davies, P. B.; Neivandt, D. J. *Appl. Spectrosc. Rev.* **2005**, *40*, 103–145.

(102) Liu, S.; Hu, Z.; Weeks, J. D.; Fourkas, J. T. *J. Phys. Chem. C* **2012**, *116*, 4012–4018.